

Investigation of Self Switching Flux Pump for High Temperature Superconducting Magnets

Muhammad Haseeb Iftikhar

Department of Electronic and Electrical Engineering
University of Strathclyde, Glasgow
United Kingdom.

A thesis submitted for the degree of
Doctor of Philosophy

October 2023

Copyright Declaration

This thesis is the result of the author's original research. It has been composed by the author and has not been previously submitted for examination which has led to the award of a degree.

The copyright of this thesis belongs to the author under the terms of the United Kingdom Copyright Acts as qualified by University of Strathclyde Regulation 3.50. Due acknowledgment must always be made of the use of any material contained in, or derived from, this thesis.

Signed:

A handwritten signature in blue ink, appearing to read 'Muhammad H. Iftikhar', with a stylized flourish underneath.

Muhammad H. Iftikhar.

Date: Tuesday 10th October, 2023

Abstract

The rapid development of second-generation (2G) high-temperature superconducting (HTS) coated conductors (CCs) has made it possible to manufacture 2G HTS coils with enormous potential for a wide range of applications, including magnetic resonance imaging (MRI) magnets, electrical propulsion systems (HTS machines), magnetic levitation trains, and energy storage (SMES). While these coils can be operated using either DC or AC current, challenges such as properly magnetizing an HTS coil under DC conditions and reducing losses under AC conditions still need to be addressed before their widespread use in scientific and industrial settings. Typically, high-current power supplies power these coils through current leads, which can complicate insulation between cryogenic and room temperature environments. Fortunately, HTS flux pumps provide an alternative method of energizing superconducting magnets without the need for direct electrical contacts, reducing resistive heating and heat leakage from current leads at room temperature. Recent developments in flux pumps for HTS magnets have made it possible to charge kA levels of current without the need for thick current leads. This thesis aims to provide a comprehensive investigation of charging an HTS magnet to operate it in a persistent current mode, and presents a novel perspective on controlling the magnetic field in HTS magnets via flux pumping.

First a two-dimensional (2D) model of a single turn high-temperature superconducting (HTS) coil was developed using a well-established H-formulation, which was iteratively refined to eliminate numerical errors from the solution. The resulting model provides insights into the self-rectifying flux pumping mechanism, which was subsequently validated experimentally. The 2D model also enables the estimation of the over-critical current voltage (also known as the flux flow voltage) across the HTS tape, which acts as a stable voltage source for

injecting current into the HTS magnet. This results in the quantization of the bridge voltage, enabling precise flux injection into a fully superconducting circuit.

A higher stable dc voltage can be achieved across the terminals of the HTS magnet using a bifilar coil as a bridge (bridge – the HTS tape short-circuits the terminals of the magnet and the secondary coil), the results are verified experimentally. The influence of the HTS tape and bifilar coil acting as a bridge across the HTS magnet is investigated. The results show that the bifilar bridge gives higher stable dc voltage to charge the HTS magnet to its critical current values and leads to the compact geometry making it suitable for adoption to complex geometries like rotor magnets in HTS machines.

HTS flux pumps can charge the magnet and compensate for any current decay, enabling quasi-persistent operation of HTS magnets. To operate an HTS magnet in the persistent current mode, a jointless HTS magnet is constructed that offers zero joint resistance, allowing it to operate in persistent current mode. However, when used in applications like rotors of fully superconducting machines, it continuously experiences a background magnetic field in the form of magnetomotive force coming from the stator. The external alternating field can cause a gradual decay of the magnetic field. Therefore, this work presents a closed-loop feedback control for field modulation in HTS magnets to operate in persistent current mode. This method eliminates the need for continuous flux pumping and allows for the injection and reduction of current in increments of 0.5 A. This flux modulation can enable a stable magnetic field for HTS magnets.

Finally, the thesis investigates critical aspects of the flux pumping in HTS magnets operating at 30 K, marking an advancement in the field of HTS magnet technology as previous flux pumps have only been reported to operate at higher temperatures.

These results provide insight into achieving a stable magnetic field in HTS magnets via flux pumping and outline the methods to compensate for current decay in HTS magnets operating in the persistent current mode – opening new pathways to high-field, low-cost HTS magnets.

Acknowledgements

I would like to express my sincerest gratitude to my supervisor Professor Min Zhang and Professor Weijia Yuan, for their unwavering support, guidance, and encouragement throughout my PhD journey. Their invaluable insights and expertise have shaped my research and personal growth.

I am also deeply grateful to University of Strathclyde for providing me with John Anderson Research Award (JARA) Studentship and an excellent academic environment necessary to complete my PhD.

My heartfelt thanks also go to my colleagues in Applied Superconductivity Laboratory in Strathclyde. I would like to thank my lab mates especially Ali, Abdelrahman, Ercan, Tian, Gaurav, Hengpei, Felix and Zhishu for creating a supportive and stimulating atmosphere in the lab. Their camaraderie and friendship have been a source of motivation and inspiration. I must thank Richard Munro, George Cochrane, Keir Mitchell, Colin Campbell for their help in experimental setups in Strathclyde.

Finally, I would like to take this opportunity to express my heartfelt appreciation to the people who have been an unwavering source of support and encouragement throughout my academic journey. Firstly, I am immensely grateful to my beloved wife, Mehwish, for her unwavering love, support, and understanding during the highs and lows of my PhD. Her constant support has been the cornerstone of my success, and I could not have done it without her. I also want to extend my gratitude to my parents, Rukhsana and Iftikhar, and my siblings, Somia, Ayesha, Muneeb and Anie, for their unwavering love, support, and encouragement. Their sacrifices and belief in me have been invaluable in helping me reach this milestone. I will forever cherish the memories we have shared, and I hope to continue making them proud.

Once again, thank you for always being there for me.

Contents

List of Figures	ix
List of Tables	xviii
1 Introduction	1
1.1 Research justification	1
1.2 Principal contributions	3
1.3 Thesis overview	4
1.4 Publications	5
2 Superconductivity	7
2.1 Introduction	7
2.2 Classification of superconductors	8
2.2.1 Classification on the basis of critical temperature	8
2.2.2 Classification on the basis of magnetic behaviour	9
2.3 Magnetic field and transport current in type-II superconductors	13
2.3.1 Flux pinning and critical current	13
2.3.2 Critical state model of type-II superconductors	17
2.3.3 Flux creep, flux flow and E - J power law	21
2.3.4 Intrinsic pinning and anisotropy	23
2.3.5 AC loss in type-II superconductors	24
2.4 Conclusion	24

3	Introduction to Flux Pump Technologies	26
3.1	Importance of flux pumps for superconducting magnets	26
3.1.1	Superconducting magnets	26
3.1.2	Persistent current operation of superconducting magnets	27
3.1.3	Flux leakage in HTS magnets and flux compensation by flux pumps	29
3.2	Low temperature superconducting flux pumps	30
3.2.1	The flux compressor	31
3.2.2	A dc dynamo	33
3.2.3	Rectifier type flux pumps	34
3.3	High temperature superconducting flux pumps	35
3.3.1	Travelling magnetic field Induced flux pumps	36
3.3.2	Rectifier type flux pumps	39
3.4	Operating principle of self-switching flux pump	45
3.4.1	Origin of dc voltage in high temperature superconductors	46
3.5	Comparison between HTS flux pumps	47
3.6	Conclusion	49
4	Modeling and Experimental Analysis on a Self-Switching Rectifier Flux Pump	50
4.1	Introduction	50
4.2	2-D simulation of self-switching flux pump	51
4.2.1	2D H-formulation	51
4.2.2	Geometrical description	55
4.2.3	2D FEA modeling of HTS flux pump	57
4.3	A compact flux pump for HTS magnets	61
4.3.1	Geometrical description of compact flux pump	61
4.3.2	Non-Inductive Winding Structure	62
4.3.3	HTS magnet	64
4.3.4	Equivalent circuit model	66
4.4	Experiment	67

Contents

4.4.1	Experiment test bench	67
4.4.2	Applied current	73
4.4.3	Current induced in the charging coil	74
4.4.4	Exploring the Current-Voltage characteristics of a bridge in flux pump	75
4.4.5	Flux injection into the HTS magnet	78
4.5	Estimation of losses in flux pump	80
4.5.1	Losses in copper	80
4.5.2	Efficiency	82
4.6	Discussion	84
4.7	Conclusion	85
5	Feedback-Controlled Field Modulation for HTS Magnets in Persistent Current Mode	87
5.1	Introduction	87
5.2	Jointless HTS loop charging using flux pump	89
5.2.1	Equivalent circuit diagram	90
5.2.2	Geometrical description	91
5.2.3	Experimental Results for Loop Charging	92
5.3	Jointless HTS Magnet	94
5.4	Field modulation in HTS magnets using closed-loop feedback control . . .	95
5.4.1	Voltage prediction in HTS-CC	96
5.4.2	Voltage estimation via FEA modeling and experimental verification	98
5.4.3	Equivalent Circuit Model	100
5.5	Experiment	102
5.5.1	Control algorithm in LabVIEW	103
5.5.2	Critical Current of a Jointless HTS Magnet	104
5.5.3	Field modulation of HTS magnet using closed loop feedback control	105
5.5.4	Precision in closed loop feedback control of HTS magnet using flux pump	109

Contents

5.5.5	Discussion	111
5.6	Conclusion	112
6	An HTS Flux Pump Operating at 30 K	113
6.1	Introduction	113
6.2	Introduction to conduction cooling system	115
6.2.1	Cooling system	115
6.2.2	Cryostat	117
6.3	Assembly and design configuration of geometry in HTS flux pumps	118
6.3.1	HTS magnet	118
6.3.2	Excitation coil	119
6.3.3	Impregnation of a sample under study	121
6.3.4	Final assembly	124
6.4	Experiment	125
6.4.1	Equivalent circuit model	125
6.4.2	Applied current	126
6.4.3	Induced current in the secondary coil	127
6.4.4	Voltage-current (V-I) of the bridge superconductor in the flux pump	130
6.4.5	Flux injection into HTS magnet	132
6.5	Discussion	133
6.6	Conclusion	134
7	Conclusion and Future Work	136
7.1	Introduction	136
7.2	Summary and conclusions	136
7.3	Future work	138
	References	141

List of Figures

2.1	A comparison between the Meissner effect in a superconductor and an ideal conductor is shown. The figure illustrates the effects of field cooling (FC) and zero field cooling (ZFC) on the magnetic flux in both types of conductors.	8
2.2	The development history of superconductors.	9
2.3	Phase diagram of type–I and type–II superconductors.	10
2.4	Magnetization characteristics of type–I superconductors.	10
2.5	Magnetization characteristics of type–II superconductors.	11
2.6	Increase in the number of super electrons ns and decay of magnetic field B_{app} with distance from the surface of the superconductor.	12
2.7	The structure of a single vortex	14
2.8	The current distribution of two neighbouring vortices	15
2.9	The figure shows Abrikosov FFL of Nb thin film in a magnetic field of 10 mT at 4.5 K observed using Lorentz microscopy.	15
2.10	The Lorentz force and pinning force on vortex system in type–II superconductor.	16
2.11	Geometry of an infinite long slab subjected to homogeneous external field. .	19
2.12	Magnetization process of type–II superconductor in zero field cooling following Bean model, the applied field H_a increase monotonously from zero to over $2H_p$ and reaches monotonously back to zero.	20
2.13	Magnetization process of type–II superconductor in field cooling under Bean model, H_p is initial applied field and it reduces monotonously to zero. . . .	20
2.14	The energy landscape of a pinned vortex in a uniform external current. . . .	22

List of Figures

2.15 (a) Structure of a single unit cell of YBCO, and (b) the picture of YBCO (courtesy of Wikipedia).	23
3.1 Critical field vs temperature plot for low temperature superconductors and high temperature superconductors.	27
3.2 Circuit diagram of superconducting magnet operated in a persistent current mode. The PCS drives the superconductor to the normal state and charges the magnet. Once the magnet is fully charged, the superconductor in the PCS is cooled down to a superconducting state, allowing persistent current to flow in the magnet.	28
3.3 Architecture of standard HTS coated conductor.	29
3.4 Mechanism of LTS flux pumps.	30
3.5 The flux compressors, (a) cyclic flux compressor and (b) stepless regulable flux compressor.	32
3.6 The superconducting dc dynamos, (a) simple dc dynamo and (b) axial geometry dc dynamo.	34
3.7 Normal conducting half wave rectifier, (b) superconducting rectifier pump half cycle, (c) reset half cycle.	35
3.8 Schematic drawing of open circuit voltage of travelling wave flux pump. . .	36
3.9 HTS dynamo type flux pumps, (a) schematic drawing of rotating permanent magnet based flux pump and (b) circuit diagram of the setup employing HTS sheet (red box) and HTS coil.	37
3.10 Liner travelling wave flux pumps, (a) schematic drawing of the linear travelling wave flux pump and (b) the wavelength of the travelling magnetic field produced by the linear motor flux pump can be adjusted using different designs for the iron teeth and slots.	38

List of Figures

3.11 (a)The field distribution inside a slab-like superconductor subjected to an AC magnetic field and carrying a DC transport current, as per the Bean model, (b) the presence of the DC transport current leads to an asymmetric field profile within the slab. 40

3.12 Alternating field switching flux pump, (a) schematic drawing of the ac field switched flux pump, in addition, the ac field is applied so that the flux flow into the HTS coil (load coil) through the resistive bridge and (b) the circuit diagram of the flux pump where an ac field is applied normal to the surface of the HTS tape to rectify the induced current, the resultant direct current is accumulated into the HTS coil. 42

3.13 $\mathbf{J_c B}$ switching flux pump, (a) schematic drawing of the dc field switched flux pump, in addition, the dc field is applied so that the flux flow into the HTS coil (load coil) through the resistive bridge and (b) the circuit diagram of the flux pump where an dc field is applied normal to the surface of the HTS tape to rectify the induced current, the resultant direct current is accumulated into the HTS coil. 43

3.14 Self switching HTS flux pump, (a) A varying magnetic field is applied to an HTS loop which consists of a resistive joint. A superconducting load L is connected to branch ab which has a lower critical current value than the rest of the HTS loop. (b) the $V-I$ curve of branch ab , and one example waveform of the circulating current $i(t)$. During each cycle of $i(t)$, at region A and only region A , the critical current of branch ab has been exceeded, and a voltage developed across the load. For the remainder of the waveform, $abs(i(t)) < I_c$. 44

3.15 Schematic diagram of a self-switching superconducting flux pump, comprising a transformer, a charging coil, a load coil, and a bridge connecting the two coils. 46

4.1 Illustration of HTS coated conductor in a FEM model using H formulation . 52

List of Figures

4.2 Schematic of the 2D HTS flux pump model. The model consists of three parallel thin superconducting strips, with their terminations connected to form two loops: a smaller charging loop and a larger load loop. The applied field is perpendicular to the charging loop area. Flux pumping is considered to occur if the load loop current gradually increases. Bottom shows a cross-sectional view of the model. 56

4.3 2D infinitely long model simulating flux pumping effect in COMSOL. The figure illustrates the three HTS strips, labeled as s_1 , s_2 , and s_3 . The transformer is used to generate magnetic fields and induce the current into s_1 and s_2 , referred to as the charging coil. It should be noted that in the actual system, strip s_3 is positioned far away from the other two strips. However, for the purpose of clarity and ease of visualization, the strips are shown in close proximity in the model. 58

4.4 Simulation results illustrating the charging curve of strip s_3 . The graph displays the variation of the current in strip s_3 over time as it is being charged by the fluxpump. The charging curve provides insight into the dynamics of the flux pumping effect in the system. 59

4.5 Simulation results illustrating the bridge current s_2 60

4.6 Simulation results illustrating the current in the charging coil s_1 60

4.7 Comparison between non-inductive bifilar bridge and inductive conventional bridge incorporated in an HTS flux pump. (a) Photograph of the proposed flux pump showing a double pancake magnet made of 4 mm HTS tape with a diameter of 75 mm, and a bifilar bridge wound around the magnet with a diameter of 120 mm. A transformer is used to induce an asymmetric current into the excitation circuit, which is short-circuited to the bridge through copper terminals (magnet terminals). (b) Conventional self-switching flux pump. 62

4.8 Illustration of non-inductive coil structures; (a) series solenoid, (b) parallel solenoid, and (c) bifilar pancake. 63

List of Figures

4.9	HTS magnet incorporating bridge.	65
4.10	Measured V–I curve for an HTS magnet (double-pancake coil) in this experiment and its equivalent magnetic field measured at the center of the coil.	65
4.11	Equivalent circuit model, (a) circuit diagram of flux pump with conventional bridge with flux flow resistivity R_{ff} and bridge inductance L_b , (b) circuit diagram of a flux pump with proposed bifilar bridge configuration where bridge inductance is cancelled out $L \simeq 0$	66
4.12	Calibration curves for the Hall effect sensors in the current transducers. (a) Calibration curve for current transducer 1. (b) Calibration curve for current transducer 2.	70
4.13	GHS-C Cryogenic 1D Hall Sensor (a) Photograph and (b) Circuit Diagram of PCB.	71
4.14	Asymmetric applied current waveform.	73
4.15	Induced current (i_s) in the charging coil of a self switching flux pump with a conventional bridge.	74
4.16	Induced current (i_s) in the charging coil of a self switching flux pump with a bifilar bridge.	75
4.17	Bridge current (i_b), plot of current flowing through a conventional flux pump bridge.	76
4.18	Bridge current (i_b), plot of current flowing through a bifilar flux pump bridge.	77
4.19	The voltage measured (v_b) across the conventional bridge in the flux pump shows an amplitude of under 100 mV, along with a noticeable DC biasing trend over time.	77
4.20	The voltage measured (v_b) across the bifilar bridge in the flux pump shows an amplitude of over 100 mV, and the peak voltage remains stable over time.	78
4.21	The load’s magnetic field measured at the center of the coil magnet for both cases, with conventional bridge saturating at 26 mT and bifilar bridge at 35 mT.	79

List of Figures

4.22 Measured primary current, measured charging current for conventional and bifilar bridge, measured induced voltages across conventional and bifilar bridge and measured magnetic field in a magnet coil for conventional and bifilar bridge. 80

4.23 High-temperature superconducting (HTS) magnet, (a) operated in driven mode and (b) using flux pump at 77 K. 81

4.24 Joule heat of copper lead in (a) HTS magnet operating in driven mode at 77 K and (b) HTS magnet operated using a flux pump at 77 K. 82

4.25 The efficiency trend η for flux pumps with bifilar and conventional bridges over charging duration. 84

5.1 Schematic diagram of the HTS loop being charged by the self-switching HTS flux pump. The loop is formed by slitting the HTS tape lengthwise from its center, with one side of the loop serving as a bridge and the other side featuring a single turn acting as a load. Once charging is complete, the loop will function as a persistent current one-turn HTS magnet 89

5.2 An equivalent circuit model of a flux pump charging a jointless loop, with the loop highlighted in yellow. 90

5.3 Photograph of the proposed jointless loop charging using self switching flux pump. 91

5.4 Results of the loop charging using the flux pump. (a) Asymmetric applied current waveform, (b) Induced current in the charging coil of the flux pump, and (c) Voltage measured across the loop. 93

5.5 Current plot of the jointless loop charged via self switching HTS flux pump. 93

5.6 (a) Schematic illustration of the jointless loop. (b) Calculated magnetic field plot for the jointless loop. 94

List of Figures

5.7 Block diagram of the closed-loop feedback control system for HTS magnets. The algorithm is implemented in LabVIEW. The control block reads the error, estimates the necessary bridge voltage, and determines the current required to generate the estimated bridge voltage. The signal is subsequently limited to protect the HTS from potential damage due to overcurrent. The signal generation block writes the signal for the amplifier. The amplifier produces the input signal for the primary side of the transformer. 96

5.8 (a) Sample of HTS tape to test record the voltage when the HTS tape is subjected to over critical current, and (b) 2D FEM model of HTS tape in COMSOL, layer dimensions are given in Table 5.1 and physics parameters are in Table 5.2. A pulse of a current $1.2 \times$ critical current of HTS tape is applied and the response is recorded. On left a zoom extent view of a 4 mm wide HTS tape is illustrated. 98

5.9 Voltage profile for 8 cm long HTS tape measured experimentally and calculated by FEM simulation against normalized applied current (I/I_c). 100

5.10 Simplified circuit model representing bridge as a current controlled voltage source, transformer is represented by Gain and the solder joint by R_s 101

5.11 Photograph of proposed flux pump to charge HTS magnet in persistent current operation. Magnet is prepared in jointless fashion and the flux pump is operated in closed-loop feedback control, where a LabVIEW based control calculates the voltage required to inject the required current into the HTS magnet. 102

5.12 A jointless HTS magnet is charged to it critical current value using flux pump and flux pump is switched OFF at time $t = 26 \text{ sec}$, the current decay can be observed due to self field flux creep at critical state and the current stabilize at 85 A. 104

5.13 The current in the HTS magnet against the set-point value, the current plot illustrates the field modulation in the HTS magnet and accurate reference tracking in feedback control for a flux pump. 106

List of Figures

5.14	The voltage measured across the bridge during field modulation in HTS magnet.	107
5.15	The charging current plot in the HTS secondary side of the transformer.	107
5.16	The bridge current plot i_b in HTS flux pump.	108
5.17	The bridge current vs charging current plot while charging an HTS magnet by closed loop feedback control operated flux pump.	108
5.18	The bridge current vs charging current plot while charging an HTS magnet by closed loop feedback control operated flux pump.	109
5.19	The current modulation in jointless HTS magnet indicating the precision control by removing the current from the magnet and injecting exactly the same amount.	110
5.20	The induced voltages across the bridge to precisely remove and inject the current in an HTS magnet.	110
6.1	CH-110LT Cold Head Capacity Map Using F-70 Compressor at 50Hz.	115
6.2	Illustration of the conduction cooling system, showcasing the cryostat, He compressor, temperature controller, vacuum pump, and water chiller. On the right, there is a block diagram of the cooling system.	116
6.3	3D Rendering of the Interior of the ICE Cryostat for Conduction Cooling.	117
6.4	Schematic Representation of HTS Magnet and Bridge Superconductor,(a) The HTS Magnet and Bridge Superconductor configured in a bifilar pancake configuration with direction change via an S-shaped slit in the former,(b) 3D exploded diagram of the HTS Magnet former highlighting its components and design configuration.	119
6.5	HTS Magnet and Excitation Circuit. The yellow box depicts the HTS magnet, while the bottom section shows the excitation circuit, including the charging coil housed in an oxygen-free brass former. The two components are joined together at the copper terminals using M3 bolts.	120

List of Figures

6.6	Image of HTS flux pump, (a) exploded diagram of charging coil former: showcasing components and terminals with adjoining bolts, (b) final assembly image showcasing transformer, HTS secondary/excitation coil and HTS magnet.	121
6.7	Impregnation of HTS magnet: (a) Melting of paraffin wax at 60 °C, (b) Degassing the mixture, (c) Charging coil after impregnation, and (d) HTS magnet after impregnation.	122
6.8	Schematic diagram of the final assembly of 30 K HTS flux pump.	123
6.9	Image of HTS flux pump installed on cryostat cold head for operation at 30 K.	124
6.10	The equivalent circuit of the flux pump, which includes the charging coil, bifilar bridge, and magnet serving as the load coil.	125
6.11	Applied current (i_p), (a) for flux pump operating at 77K, (b) for flux pump operating at 30 K.	127
6.12	Temperature dependence of critical current for the charging coil and bridge, along with the variation of copper resistivity with temperature	128
6.13	Induced current plot in the charging coil (i_s), (a) for flux pump operating at 77 K, (b) for flux pump operating at 30 K.	129
6.14	Temperature profile of the bridge superconductor for the flux pump operating at 30 K.	130
6.15	The voltage measured (v_b) across the bridge, (a) for flux pump operating at 77 K, (b) for flux pump operating at 30 K.	131
6.16	The load's magnetic field measured at the center of the coil magnet for both cases, (a) for flux pump operating at 77 K, (b) for flux pump operating at 30 K.	133

List of Tables

3.1	General comparison between HTS flux pumps.	48
4.1	Instantaneous heat losses in copper leads (Temperature gradient 300 K-80 K).	81
4.2	Instantaneous heat loss in primary copper of a flux pump (Temperature gradient 300 K-80 K).	81
5.1	Design parameters for layers of HTS tape subject to over critical current resistivity measurement.	99
5.2	Parameters employed in FEM simulation for layers of HTS tape subject to over critical current resistivity calculation.	99

1

Introduction

1.1 Research justification

Advancements in superconducting technology have led to a range of industrial applications and commercial uses, including superconducting motors/generators for propulsion systems, magnetic resonance imaging and nuclear magnetic resonance machines, as well as the potential integration into future fusion reactors. All these applications depend on superconductors to efficiently generate powerful magnetic fields. Numerous studies have demonstrated that extremely high magnetic fields can be produced using various methods involving superconductors [1, 2, 3, 4, 5]. Researchers have successfully created superconductor bulks that achieve magnetic fields of 17.24 T at 29 K using $YBa_2Cu_3O_{7-\delta}$ (YBCO) [6], and 17.6 T at 26 K [7]. Additionally, in a stack of superconductor tapes, a trapped field of 17.7 T was achieved [8]. These results represent magnetic field strengths significantly greater than those produced by permanent magnets. However, the cost associated with the cooling and charging system required for this purpose is exceedingly high and, in certain instances, even beyond practical affordability [9]. Advances in the fabrication of coated conductors (CCs) [10, 11, 12] have facilitated the production of lengthy superconducting CCs that possess robust bending tolerance, making them suitable for winding superconductor coils. In comparison to bulk materials and stacked tapes, CC coils exhibit significantly enhanced mechanical characteris-

tics [13]. Additionally, they offer greater flexibility in terms of demagnetization and ease of maintenance [14]. These advantages position superconducting CC coils as strong contenders for applications requiring high magnetic fields

High Temperature Superconducting (HTS) magnet operating in a persistent current mode (PCM) is an ideal candidate for use in high-field magnet systems [15, 16], such as magnetic resonance imaging (MRI) [17], nuclear magnetic resonance (NMR) [18], and superconducting motors [19, 20]. This issue predominantly arises from the challenge of operating magnets constructed from HTS-CC in the persistent current model due to relatively low n -values [21], and achieving a lossless joint proves to be difficult [22, 23]. One approach to tackle this problem involves operating a magnet with an external power supply, which results in significant heat losses due to copper leads transporting DC current from room temperature to cryogenic temperature [24]. Such losses reduce system efficiency and lead to increased cooling demands. An alternative solution is to incorporate a flux pump. A flux pump device can inject a substantial DC current into a superconducting circuit without requiring electrical contact [25, 26, 27, 28, 29, 30, 31, 32, 33, 34, 35, 36, 37]. HTS flux pumps have the capability to charge the magnet and compensate for any current decay, enabling the quasi-persistent current operation of HTS-CC magnets.

HTS flux pumps present a promising alternative for energizing superconducting magnets without necessitating direct electrical contacts, thereby reducing resistive heating and heat leakage from current leads at room temperature. This thesis undertakes a comprehensive exploration of the stable generation of DC voltages for flux pumping in HTS magnets and introduces a fresh viewpoint on controlling the magnetic field in HTS magnets through flux pumping. Additionally, novel flux pump devices with improved performance are introduced.

1.2 Principal contributions

Bifilar bridge configuration

This thesis demonstrates flux pumping utilizing a non-inductive bifilar coil as a bridge. This configuration yields higher and more stable DC voltages while the superconductor is subjected to a flux flow regime, resulting in increased load current. Furthermore, a bifilar bridge results in a compact-sized magnet with the bridge neatly wound across it, rendering it a strong candidate for intricate applications such as rotating machines.

Moreover, the novel design of the bifilar bridge represents a significant advancement in the development of efficient and compact HTS flux pumps. The bifilar bridge configuration provides the flexibility to wind a larger coil. This setup opens the door to achieving high bridge voltages, potentially revolutionizing the replacement of costly, linear, and bulky power supplies in large-scale applications.

Quantitative analysis of DC voltage generation in high-temperature superconducting coated conductors

This thesis presents a thorough investigation into the generation of DC voltage in HTS CCs, which includes precise calculations of the flux flow resistance values within these conductors. The validation is subsequently demonstrated using both computer-aided Finite Element Analysis (FEA) and laboratory experiments.

Closed loop feedback-controlled field modulation

This thesis introduces a novel closed-loop feedback control approach for flux modulation in HTS magnets operating under persistent current mode. Experimental results demonstrate the precision of the proposed control technique in generating a DC voltage across the HTS bridge, leading to efficient flux modulation within the HTS magnet.

HTS Flux Pump Operating at 30 K

A novel HTS magnet has been designed to function in conduction-cooled environments below 77 K. This magnet integrates a built-in bifilar bridge, allowing it to charge using a flux pump and operate as a persistent current magnet. The experiment initially tested the flux pump at 77 K and later at a colder 30 K temperature. In both instances, the magnet successfully generated a magnetic field of 65 mT at its center. Moreover, the magnet is characterised by an improved cooling capability, enabling the attainment of higher magnetic fields through flux pumps. The innovation lies in the fact that this HTS magnet functions at temperatures below 77 K, which is a novel advancement. Until now, documented flux pumps have primarily operated at liquid nitrogen temperatures.

1.3 Thesis overview

This thesis aims to investigate the viability of charging the HTS magnets via a self rectifier HTS flux pump to operate it in a persistent current mode. In it, the challenges and solutions to mitigate those challenges are identified.

Chapter 1 provides the introduction to this thesis.

Chapter 2 provides a concise introduction to superconductivity and its fundamental theories. It begins by defining the concept of superconductivity and categorizing different types of superconductors. Furthermore, it explores the macroscopic magnetization theories of type II superconductors in detail.

Chapter 3 discusses the practical motivation and objectives of this study in detail. The usage of superconductors in high field applications is first introduced, followed by an analysis of the challenges associated with operating HTS magnets in persistent current mode. The concept of using flux pumps as a potential solution is then presented. Various LTS and HTS flux pumps are introduced, and their characteristics and limitations are discussed.

Chapter 4 focuses on simulation and experimental studies of self-rectifying HTS flux pumps at 77 K. In addition, this research provides a compact solution for generating a stable

DC voltage across the HTS magnet, allowing for higher current injection and making it a feasible choice for critical applications, such as the rotor magnets of fully superconducting machines in future all-electric propulsion systems.

Chapter 5 presents a novel feedback-controlled flux modulation technique for HTS magnets operating in the persistent current mode. The method is based on the flux pump mechanism, which generates a DC voltage by applying a current higher than the critical current of the charging superconductor. Through closed-loop feedback control, the flux modulation enables precise injection and reduction of HTS magnet current in 0.5 A increments.

Chapter 6 reports the viability of using above mentioned HTS flux pumping for future all-electric aircraft propulsion systems. As a practical example, this work demonstrates flux pumping at 30 K, which is a significant advancement in the field of HTS magnet technology towards the development of liquid hydrogen-cooled all-electric propulsion systems.

Chapter 7 provides a comprehensive summary of the research findings, integrating the various lines of inquiry and examining their implications. The chapter concludes by offering recommendations that can guide future research in this area and support the development of commercially viable high field HTS magnets operating in persistent current mode.

1.4 Publications

1. ***Muhammad Haseeb Iftikhar**, Min Zhang and Weijia Yuan “Feedback-Controlled Flux Modulation for High-Temperature Superconducting Magnets in Persistent Current Mode.” IOP Superconductor Science and Technology 36(5):055008, APR 2023.
2. ***Muhammad Haseeb Iftikhar**, J Geng, Weijia Yuan and Min Zhang. “A Noninductive Bifilar Coil to Design Compact Flux Pumps for HTS Magnets.” IEEE Transactions on Applied Superconductivity 32.9 (2022): 1-7.
3. A Elwakeel, E Ertekin, M Elshiekh, **Muhammad Haseeb Iftikhar**, W Yuan, M Zhang “Protection system architecture for all-electric aircraft.” IEEE Transactions on Applied Superconductivity (2023): 1-7.

Chapter 1. Introduction

4. T. Lan, H. Liao, **Muhammad Haseeb Iftikhar**, W. Yuan, A. Cole, R. A and M. Zhang, “Multi-filament HTS cables to reduce AC loss: proof-of-concept experiments and simulation.” IEEE Transactions on Applied Superconductivity (2023): 1-25.
5. H. Lio, Z. Wei, **Muhammad Haseeb Iftikhar**, W. Yuan and M. Zhang “Magnetization Characteristics of HTS-Stacked Ring Magnets with and without HTS Stack Inserts.” IOP Superconductor Science and Technology, submitted (2023).

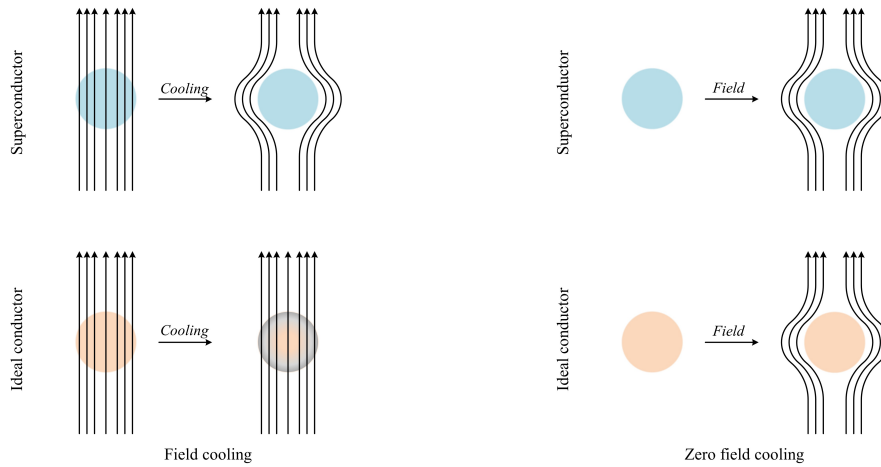
*Publications related to this thesis

2

Superconductivity

2.1 Introduction

In 1911, a Dutch scientist named H. Onnes discovered that the resistance of mercury abruptly decreased to zero at a temperature lower than 4.2 Kelvin, which led to the initial definition of superconductivity. After this discovery, superconductors are considered an ideal conductors below a critical temperature (T_c). In 1933, W. Meissner and R. Ochsenfeld made a discovery known as the Meissner Effect [38], which refers to the perfect diamagnetic behavior exhibited by a superconductor. Figure 2.1a illustrates the difference between an ideal conductor and a superconductor under field cooling. The effect of field cooling (FC), which involves applying a magnetic field before cooling the sample, is demonstrated. After a superconducting material is cooled below its critical temperature (T_c), the magnetic field is expelled from the inner region due to the Meissner effect. Conversely, in an ideal conductor, the magnetic field remains stable within the conductor according to Lenz's law after it has been cooled down. Figure 2.1b depicts the impact of zero field cooling (ZFC), where the sample is cooled before the application of the magnetic field. Both a superconducting material and an ideal conductor expel a magnetic field from the inner area under these circumstances. Although the outcome seems comparable, the expulsion of magnetic flux from a superconducting material is a consequence of the Meissner effect, while the expulsion of magnetic flux from an ideal



(a) Field cooling, the magnetic field is applied prior to cooling the sample.

(b) Zero-field cooling, the sample is cooled before applying the magnetic field.

Figure 2.1: A comparison between the Meissner effect in a superconductor and an ideal conductor is shown. The figure illustrates the effects of field cooling (FC) and zero field cooling (ZFC) on the magnetic flux in both types of conductors.

conductor is due to Lenz’s law.

2.2 Classification of superconductors

Superconductors are classified in different ways, and they can be classified based on their critical temperature, as Low Temperature Superconductors (LTS) and High Temperature Superconductors (HTS). If they are being studied on the basis of magnetic behaviour, they can be classified as Type–I superconductors and Type–II superconductors.

2.2.1 Classification on the basis of critical temperature

The critical temperature (T_c) of mercury is only 4.2 K discovered in 1911. Later in the century, due to the researchers’ continuous effort, superconductors with higher critical temperatures were discovered. A detailed discovery history is shown in Figure 2.2.

In 1986, Muller et al. discovered Lanthanum–Barium–Copper Ceramic ($LaBaCuO_4$) [40], with a critical temperature (T_c) of 30 K, a benchmark temperature to classify supercon-

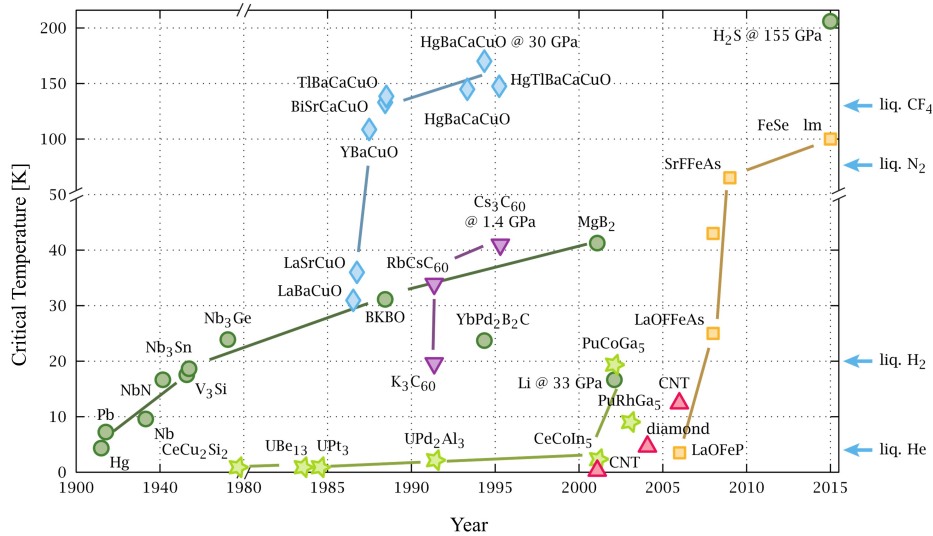


Figure 2.2: The development history of superconductors, [39].

ductors. A superconductor is a low temperature superconductor if its critical temperature is below 30 K. Otherwise, it is a high temperature superconductor.

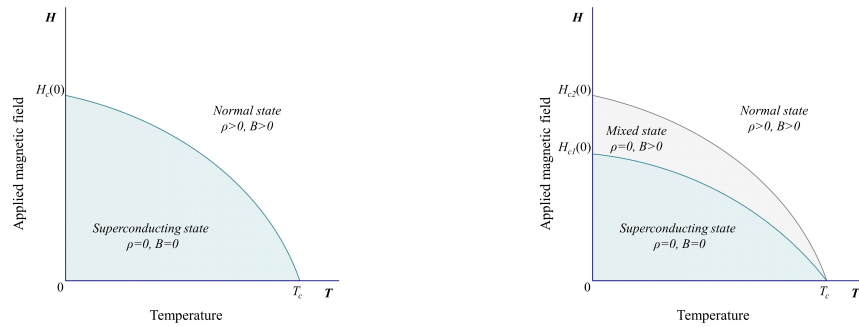
2.2.2 Classification on the basis of magnetic behaviour

In the Section 2.1, we mentioned the Meissner effect. Let's delve into the Meissner state and its role in classifying superconductors. Superconductors respond differently to the increased external applied field. Some directly enter the normal state, known as Type-I and some enter a mixed state before returning to the normal state and are known as Type-II superconductors, illustrated in Figure 2.3.

Type I superconductors are characterized by a critical field, denoted as B_c . When the external field surpasses B_c , these superconductors undergo an abrupt transition from the Meissner state to the normal state. In the normal state, the magnetic flux fully penetrates the sample, the magnetization drops to zero as illustrated in Figure 2.4, and the internal magnetic field of the sample becomes equal to the external field [41]. Type I superconductors primarily consist of metal alloys such as mercury (Hg) and tin (Sn).

Type II superconductors exhibit two critical fields: the lower critical field (B_{c1}) and the

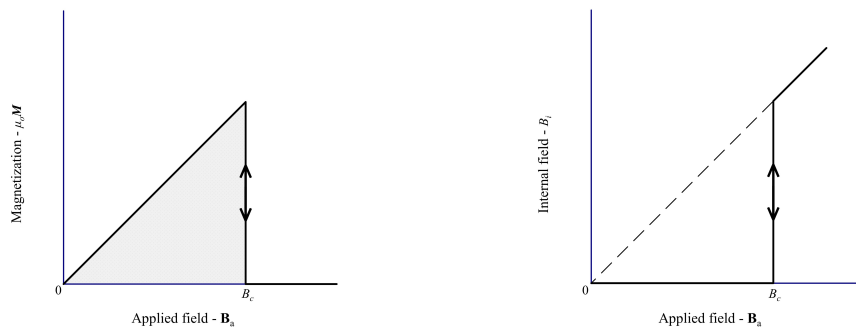
Chapter 2. Superconductivity



(a) Type-I superconductors have only one critical field, \mathbf{H}_c , below which they are in a superconducting state, otherwise in a normal state.

(b) Type-II superconductors have a lower critical field, \mathbf{H}_{c1} , below which they are in a superconducting state. They also possess an upper critical field, \mathbf{H}_{c2} ; between \mathbf{H}_{c1} and \mathbf{H}_{c2} , they exist in a mixed state, and above \mathbf{H}_{c2} , they are in a normal state.

Figure 2.3: Phase diagram of type-I and type-II superconductors.



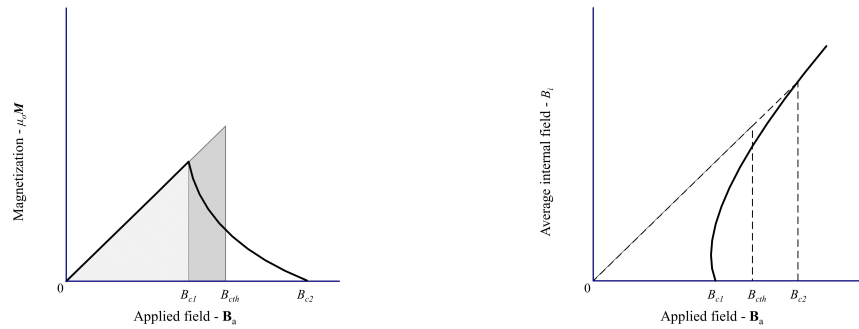
(a) Magnetization plot for type-I superconductors.

(b) Internal field plot for type-I superconductors.

Figure 2.4: Magnetization characteristics of type-I superconductors.

upper critical field (B_{c2}). At a lower critical field, the superconductor undergoes a transition where the magnetic field starts to penetrate it in the form of quantized flux lines. The state involving the partial penetration of magnetic flux is referred to as the mixed state. Within this state, the magnetization of the type II superconductor decreases monotonically as the applied

field increases until reaching the upper critical field as illustrated in Figure 2.5 [41]. When the upper critical field is reached, the magnetization drops to zero and the internal field become equal to the external field at this stage, the superconductor becomes normal [42]. Examples of type II materials are alloys and compounds, such as Nb_3Sn , NbTi , MgB_2 and all high- T_c cuprates [43].



(a) Magnetization plot for type-II superconductors.

(b) Internal field plot for type-II superconductors.

Figure 2.5: Magnetization characteristics of type-II superconductors.

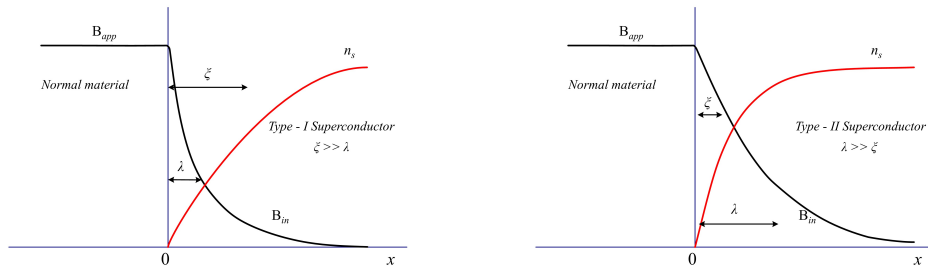
Ginzburg and Landau in 1950 proposed a theory known as Ginzburg – Landau theory to differentiate between type-I and type-II superconductors [44]. Landau’s theory of phase transitions is the foundation for this, which involves minimizing the free energy in a superconductor. This results in the derivation of two GL (Ginzburg-Landau) equations, which in turn define two crucial length scales [45]. The first is called coherence length (ξ), which is defined as the distance near the boundary of a normal material and a superconductor. In which the super electrons (cooper pairs [46]) density increases from zero (in a normal material) to a constant value inside the superconductor. The second is called penetration depth (λ). It describes the length scale with which the external magnetic field (\mathbf{B}) decays exponentially to zero inside a superconductor.

The relation between coherence length and penetration depth is known as Ginzburg –

Chapter 2. Superconductivity

Landau parameter and can be written as;

$$\kappa = \frac{\lambda}{\xi} \quad (2.1)$$



(a) The coherence length and penetration depth are shown for type-I superconductors ($\xi \gg \lambda$)

(b) The coherence length and penetration depth are shown for type-II superconductors ($\lambda \gg \xi$)

Figure 2.6: Increase in the number of super electrons n_s and decay of magnetic field B_{app} with distance from the surface of the superconductor.

A superconductor can then be classified as a type-I superconductor if $\kappa < 1/2^{1/2}$; otherwise, it is classified as a type-II superconductor, as illustrated in Figure 2.6. The relationship between B_{c1} and B_{c2} can be obtained from GL equations as;

$$B_{c1} = \frac{B_{cth} \ln \kappa}{\sqrt{2}\kappa} \quad (2.2)$$

$$B_{c2} = \kappa\sqrt{2}B_{cth} \quad (2.3)$$

Where B_{cth} is thermodynamic critical field.

2.3 Magnetic field and transport current in type-II superconductors

2.3.1 Flux pinning and critical current

It is well documented that when magnetic field B_{app} penetrates type-II superconductors, they go to the mixed state before entering the normal state. The flux flows in the superconductor in the form of tubes, called vortices [47]. Abrikosov further explains that each vortex has a core through which the flux lines go, and a circulating current (screening current) flows around the core, as shown in Figure 2.7 [48]. The radius of the core is equal to the coherence length (ξ), and the circulating current's radius equals the penetration depth (λ), within which current density decreases exponentially. The density of super electron is very low in the core region; therefore, it can be considered normal. According to Ginzburg – Landau theory, each vortex contains a flux quantum ($\Phi_0 = h/2e = 2.0679 \times 10^{-15} \text{ T}\cdot\text{m}^2$). The magnetic field's peak value lies at the vortex's centre. If the penetration depth is significantly larger than the coherence length, the macroscopic flux density in the superconductor can be considered proportional to the density of vortices [48, 49]. If N_A is the number of vortices per unit area in a superconductor, then the relationship can be given as

$$B_{in} = N_A \Phi_0 \quad (2.4)$$

If the two vortices are close to each other, there will be a force between the screening current of the vortex and the magnetic flux of the other vortex, known as the Lorentz force. A vortex in the mixed state is the quasiparticle, and the core region and the circulation current shown in Figure 2.7 are considered a whole body. If the circulating currents are subject to the Lorentz force, it impacts the complete vortex [51, 52, 53].

The illustration in Figure 2.8 displays two adjacent vortices that share the same polarity (parallel magnetic field). To simplify the problem, it is assumed that the circulating current J_2 from vortex 2 is uniform within the area of vortex 1. Under this assumption, vortex 2

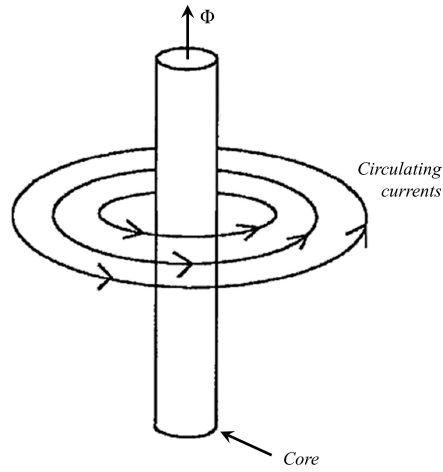


Figure 2.7: The structure of a single vortex [50].

experiences a repulsive force from vortex 1, the magnitude of which is equivalent to

$$\mathbf{f}_2 = \mathbf{J}_1 \times \Phi_0 \quad (2.5)$$

Similarly, vortex 1 experiences the same repulsive force on vortex 2.

The repulsive forces between neighboring vortices in the mixed state are equal to the magnetic stress. This results in a stable vortex pattern known as the Abrikosov Flux Line Lattice (FLL), as explained by [55]. The vortices form a hexagonal pattern that minimizes the potential energy between them, as depicted in the Figure 2.9. There are several techniques available to experimentally observe the FLL [56, 57, 58, 59, 60, 61, 62, 63, 64].

The vortices are uniformly distributed in a pure superconductor, and a magnetic gradient cannot form. According to the Ampere law, the magnetic gradient inside type-II superconducting materials equals a macroscopic current. This concludes that type-II superconductors cannot either magnetise or transport current, which means pure type-II superconducting materials have little use in practical engineering. This problem can be solved by adding impurity to the superconducting materials and crystalline defects. The outcome of this is the trapping of vortices, which creates a magnetic gradient, a phenomenon referred to as

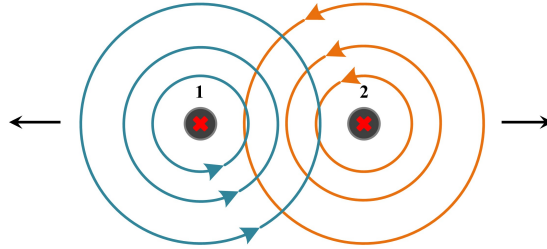


Figure 2.8: The current distribution of two neighbouring vortices

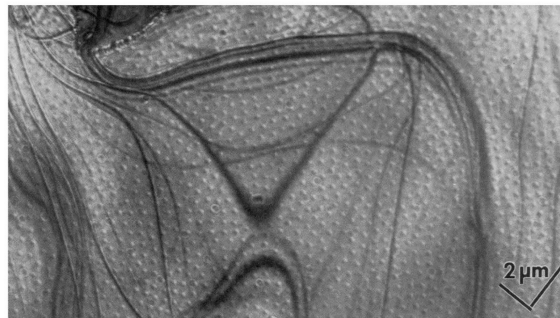


Figure 2.9: The figure shows Abrikosov FFL of Nb thin film in a magnetic field of 10 mT at 4.5 K observed using Lorentz microscopy [54].

flux pinning. The impurities or crystalline defects responsible for this are known as pinning centres.

The Lorentz force (f_l) and pinning force (f_p) acting on a vortex system are demonstrated in Figure 2.10. The magnetic flux density B can either be an applied field or a self-field, while the current density J can be either a transport current or a magnetization current. The Lorentz force acting on an individual vortex is given by

$$f_l = \mathbf{J} \times \Phi_0 \quad (2.6)$$

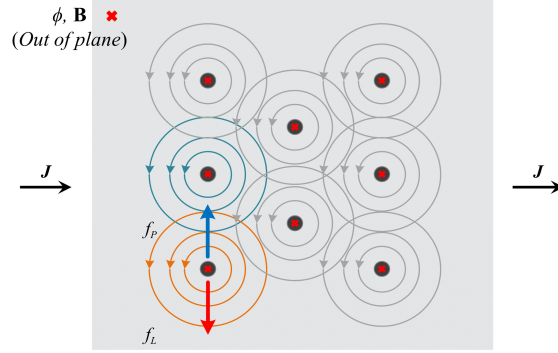


Figure 2.10: The Lorentz force and pinning force on vortex system in type-II superconductor.

When the pinning force exceeds the Lorentz force ($f_p \leq f_l$), the vortex is pinned by the pinning force. Conversely, if the pinning force is weaker than the Lorentz force ($f_p \geq f_l$), the vortex detaches from the pinning center and begins to move in the direction of the Lorentz force. Therefore, type-II superconducting materials cannot maintain a macroscopic current density without flux pinning. The phenomenon of “flux pinning” is, therefore, essential for practical applications.

The vortex system is self-organizing due to the mutual repulsive forces, and therefore, a few pinning centres are sufficient to pin the entire system. The macroscopic magnetic flux density is equivalent to the average Lorentz force F_l acting on the FLL and can be mathematically represented as follows

$$\mathbf{F}_l = \mathbf{J} \times \mathbf{B} \quad (2.7)$$

If we consider the pinning force on the FLL as F_p , then the maximum current density (also known as critical current density J_c) that the material can sustain is equal to

$$J_c = \frac{F_p}{B} \quad (2.8)$$

Thus, in a type-II superconducting material subject to a constant temperature and magnetic field, the critical current density J_c increases with a stronger pinning force.

If the pinning force is larger than the Lorentz force F_l , vortices in the superconductor cannot move, and current flows without dissipation. The critical current density J_c in the superconductor can be considered as the value presented in Equation 2.9. If the pinning force is strong, it is defined as a hard superconductor [65]. Otherwise, it is defined as a soft superconductor.

$$\mathbf{F}_p = \mathbf{F}_l = \mathbf{J}_c \times \mathbf{B} \quad (2.9)$$

A vortex in a type-II superconducting material interacts with the lattice forces of the material, causing thermal dissipation due to the vibration of the lattice. This is different from common metals where thermal dissipation is caused by scattering of free electrons. In the mixed state, when the Lorentz force is greater than the pinning force ($f_l > f_p$), the FLL is driven due to Lorentz force, resulting in “flux flow”. This movement of the vortices causes thermal dissipation due to the interaction with the lattice. However, if $f_p \geq f_l$ and the temperature is $T > 0$ K, single vortices can still move out of the pinning potential due to thermal activation. This phenomenon is called “flux creep”.

2.3.2 Critical state model of type-II superconductors

A critical state model is a vital tool for understanding the magnetization in type-II superconductors, as it describes the current-field distribution in a mixed state. It states that a type-II superconductor is always in a critical state, its current density always equals its critical current density $\pm J_c$ or zero, and the curl of the magnetic field gives J_c . Furthermore, the electric field E is always in the same direction as J . When a low current or field is applied to a superconductor, a current with a critical current density will flow in the outer part of the superconductor, it will shield the inner part, the current, and the B field will be zero at the inner part of the superconductor.

Two types of critical state models exist, namely the Bean model and the Kim model. The Bean model posits a fixed critical current density J_c for the materials, while the Kim model

considers the magnetic field dependency of the critical current density $J_c(B)$. The Bean model is useful for intuitively estimating the magnetization of a hard superconductor with a regular shape, while the Kim model provides a more accurate prediction of magnetization.

Bean model [66]

Hard superconductors have only three possible current density values, 0 and $\pm J_c$. In the absence of flux, $J = 0$; otherwise, it possesses a value of $J = \pm J_c$. The Bean model is a straightforward and powerful tool for understanding the magnetization of hard superconductors under zero-field cooling and field cooling.

Assume a slab-like superconductor with length $2a$ in the x -direction and infinitely long in the rest of the direction in a 3D plane, as illustrated in Figure 2.11. If the field is applied in the z -direction, Ampere's law gives

$$\nabla \times \mathbf{B} = \mu_0 \mathbf{J}_c \quad (2.10)$$

For one-dimensional geometry above equation can be simplified as

$$\frac{dB}{dx} = \mu_0 J_c \quad (2.11)$$

Therefore, the penetration depth x is proportional to the applied field intensity, and the field's gradient is constant (where there is a field).

Consider zero-field cooling magnetization process on the same geometry as mentioned earlier, under the Beans model. When the applied field intensity is small, the field penetrates the outer part of the superconductor. By increasing the applied field, the superconductor is further penetrated. When the field reaches the value of $H_p = aJ_c$, the current reaches the superconductor's centre, as shown in Figure 2.12b. Further increase in the field does not change the current distribution but increases the field in the superconductor. When the applied field is decreased, the current in the outer part changes direction. A field is trapped in the superconductor after the field is removed. In a zero-field cooling case, at least a field of

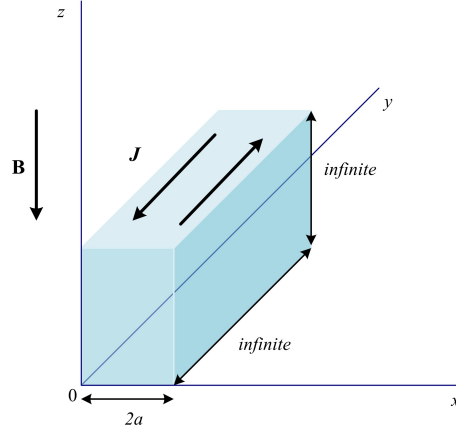


Figure 2.11: Geometry of an infinite long slab subjected to homogeneous external field.

$2H_p$ is required to trap the maximum field of H_p in the centre of the superconductor. The superconductor with applied field $2H_p$ and the field distribution when the applied field has returned to zero can be seen in Figures 2.12.

Unlike zero-field cooling, field cooling can be observed in Figure 2.13. Initially, the field in the superconductor has a homogeneous value of H_p , but no current exists. With the decrease of the external field, a current is induced in the outer part of the sample. When the field reduces to zero, a field of H_p is trapped in the centre of the superconductor. Therefore, field cooling needs a minimum applied field of only H_p to trap a field of magnitude H_p .

Kim model [67]

Kim–Anderson model is more realistic; it assumes that the critical current density depends on the local field intensity. Among many forms of field–critical relationships, the most commonly used equation is [68, 67, 65],

$$J_c(B) = \frac{J_{c0}}{1 + \frac{B}{B_0}} \quad (2.12)$$

J_{c0} is critical current density with no applied field, and B_0 is constant above equation, generally referred to as the Kim–Anderson model.

Chapter 2. Superconductivity

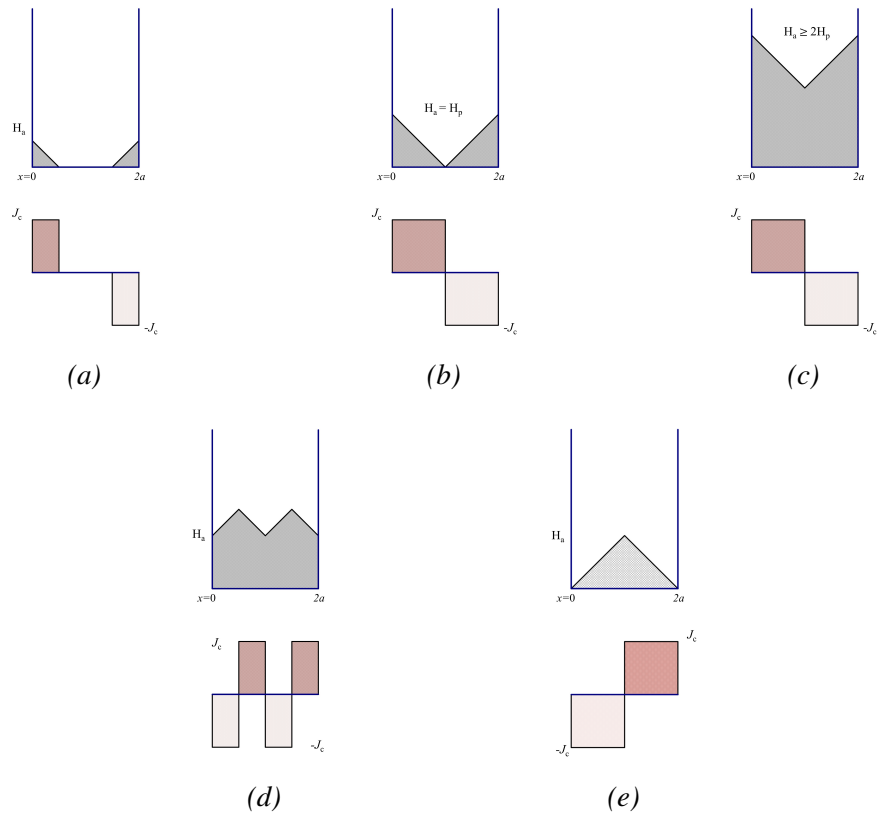


Figure 2.12: Magnetization process of type-II superconductor in zero field cooling following Bean model, the applied field H_a increase monotonously from zero to over $2H_p$ and reaches monotonously back to zero.

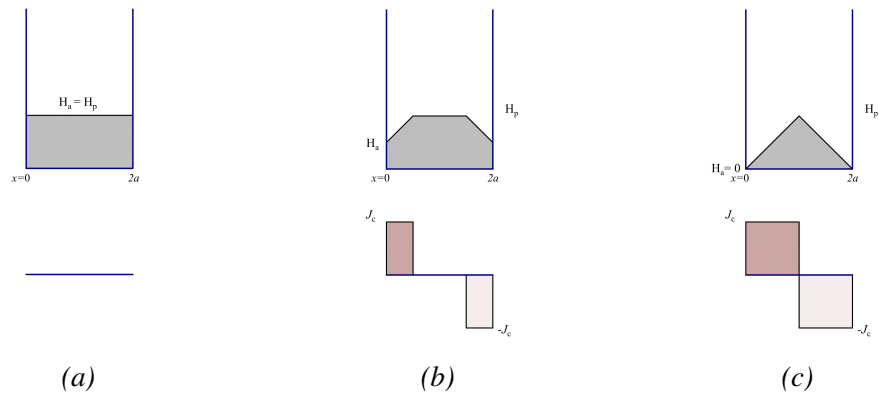


Figure 2.13: Magnetization process of type-II superconductor in field cooling under Bean model, H_p is initial applied field and it reduces monotonously to zero.

2.3.3 Flux creep, flux flow and E - J power law

In the critical state model, the superconductor is ideally stable and not disturbed by thermal activation. However, this is not the case when $T > 0$ K for HTS materials operating at 77 K, where there is significant flux creep relaxing of the magnetisation [69].

As discussed earlier in Section 2.3.1, the FFL is pinned by the pinning force when $J \leq J_c$. Therefore thermal activation enables the vortices to hop out of the pinning potentials, a phenomenon known as “flux creep”. On the other hand, when $J \geq J_c$, the Lorentz force is greater than the pinning force, which forces the FFL to move, this is known as “flux flow”. In both cases, the movement of vortices gives rise to an electric field and according to the Lorentz transformation [70]

$$\mathbf{E} = \mathbf{v} \times \mathbf{B} \quad (2.13)$$

Where v is the velocity of FLL, flux motions generate the measured electric fields in type-I and type-II superconducting material according to Equation 2.13. The heat loss comes from the parallel component of the electric field as compared to the transport current, whereas the perpendicular component gives rise to the Hall effect [71, 72, 73, 74]. In contrast to normal conductors, where heat losses are caused by the scattering of free electrons and the Hall effect arises from an accumulation of charges at the conductor edge, type-II superconducting materials exhibit fundamentally different behaviour.

The Arrhenius equation [75] is used in Anderson’s flux creep model [76] to describe the rate at which flux lines depart from the pinning centre when $J \geq J_c$.

$$R = v_0 e^{-\frac{U}{kT}} \quad (2.14)$$

Where the attempt rate is denoted by R , the microscopic attempt frequency by v_0 and is of the order of $10^{-8} - 10^{-10} s^{-1}$, the effective pinning potential is U , T is the absolute temperature and k is the Boltzmann constant. Figure 2.14 illustrates a theoretical explanation: when a uniform transport or magnetisation current ($J \geq J_c$) flows across the vortex, the pinning barrier becomes tilted, and the vortex hops to one side is greater than the probability of

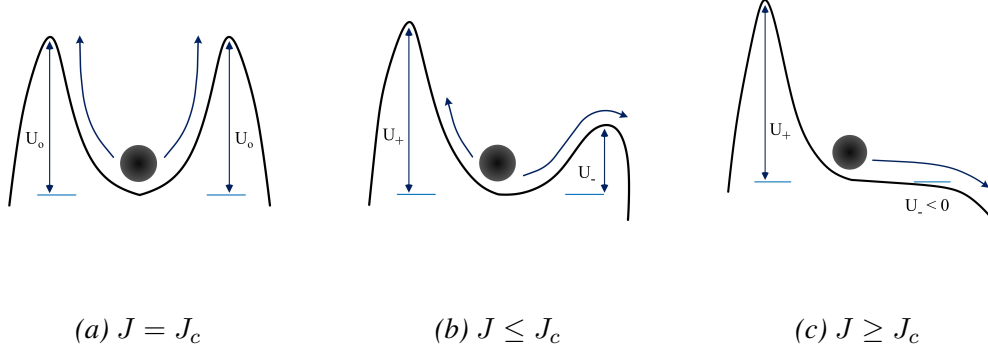


Figure 2.14: The energy landscape of a pinned vortex in a uniform external current.

hopping to the other. The effective potential on both sides can be expressed as[77]

$$\begin{aligned} U_+ &= U_0(1 - J/J_c) \\ U_- &= U_0(1 + J/J_c) \end{aligned} \quad (2.15)$$

Solving Equations 2.15 and 2.14 will yield the attempt velocity of the vortex.

$$v = v_0 l \sinh\left(\frac{U_0 J}{kT J_c}\right) \exp\left(-\frac{U_0}{kT}\right) \quad (2.16)$$

Where l is effective jump distance. Therefore the E - J relationship whilst flux creep can be given as

$$E = Bv = \rho_c J_c \sinh\left(\frac{U_0 J}{kT J_c}\right) \exp\left(-\frac{U_0}{kT}\right), \quad J \leq J_c \quad (2.17)$$

Where ρ_c is flux creep resistance and is equal to $Bv_0 l / J_c$.

For $J > J_c$, The vortices flow to one side as the potential barrier is lower than the pinning position as shown in Figure 2.14c. The electric field induced due to flux flow can be given as[78]

$$E = E_c + \rho_f J_c \left(\frac{J}{J_c} - 1\right), \quad J > J_c \quad (2.18)$$

E_c is the electric field due to flux creep at $J = J_c$, and ρ_f is the flux flow resistance. Equations 2.17 and 2.18 provide an E - J relationship for type-II superconducting materials. However,

practical simulations do not commonly employ this relationship. A more practical relationship for HTS materials is the E - J power law. It is derived from the direct four-point probe method [79] of the voltage-current relationship in the transport current measurement. The E - J power law is expressed as[80]

$$E = E_c \left(\frac{J}{J_c} \right)^n \quad (2.19)$$

Where E_c is a constant, which is usually set as 10^{-4} V/m to determine the critical current density of superconductors experimentally. The n value in the above equation varies with material and temperature; $n = U/kT$ reflects the stiffness of the E - J relationship. The critical state model is a specific case of the above equation, where n is equal to ∞ .

2.3.4 Intrinsic pinning and anisotropy

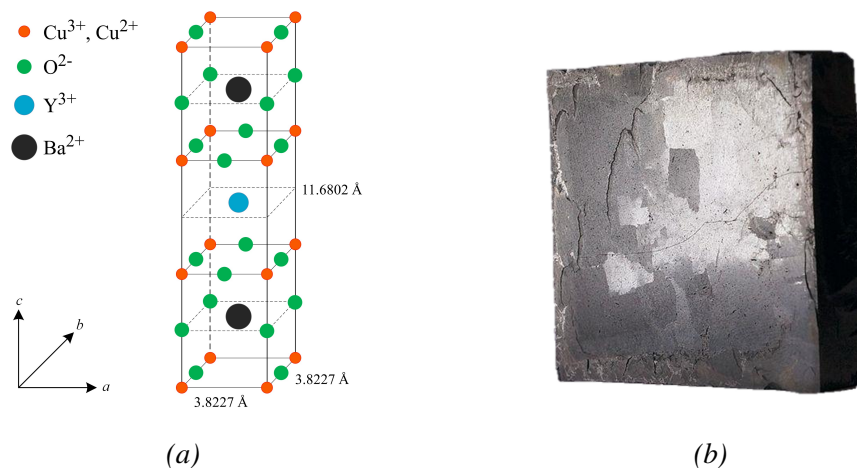


Figure 2.15: (a) Structure of a single unit cell of YBCO, and (b) the picture of YBCO (courtesy of Wikipedia).

Figure 2.15 displays the unit cell structure that is typically found in YBCO. In YBCO, supercurrent flows more easily within the CuO_2 plane (ab plane) than between layers (c direction). The motion of vortices in the ab plane is not prohibited in the absence of pinning centres. However, the motion of vortices between the CuO_2 layers is restricted due to intrinsic pinning [45]. Intrinsic pinning produces anisotropy in superconducting materials, and due to anisotropy, the critical current develops an angular-dependent relation with the applied

magnetic field [81]. For example, the peak value of J_c usually applies when $H \parallel ab$.

2.3.5 AC loss in type-II superconductors

According to the critical state concept, there is no loss in a superconductor when it carries a direct current or is in a DC magnetic field. However, the situation differs when the superconductor is transporting an alternating current or is under an AC magnetic field. This alternating transport current or external magnetic field gives rise to the magnetic field redistribution inside the superconductor. According to Faraday's law, flux motion inside the superconductor induces an electric field E . The electric field E is always in the same direction as the current density J inside the superconductor. Consequently, there is a loss, which is described as

$$Q = \int_V EJ dV \quad (2.20)$$

Q is the total loss in a superconductor and is in Watts (W). V donates superconducting domain. The loss due to transporting an AC current is defined as a transport loss, and the loss caused by an external AC magnetic field is defined as magnetisation loss [82]. These losses occur when a superconductor transporting an alternating current is subjected to an external AC field.

2.4 Conclusion

The fundamental knowledge of superconductors is presented in this chapter, which includes basic superconductivity and macroscopic electromagnetic theories for type-I and type-II superconducting materials. The explanation of Meissner effect for type-I superconducting materials is explained. The mixed state in type-II superconductors is comprehended by Ginzburg-Landau equations, flux quantisation, characteristic lengths, basic vortex dynamics and pinning forces. In addition to this, the properties of high temperature superconductors and low-temperature superconductors are discussed. The different critical temperatures and critical current densities of these materials are outlined and the importance of these properties for various applications is highlighted. In the following chapters of this thesis, the focus is on

Chapter 2. Superconductivity

type-II superconductors, which are extensively used in various applications such as energy storage, power transmission and medical imaging. Therefore, macroscopic electromagnetic theories for type-II superconducting materials are explained in detail along with the concepts of flux creep, flux flow, and the E - J power law, and critical state models like the Bean model and Kim model. The cross-field effect and intrinsic pinning were introduced for type-II superconductors, which are essential for controlling the behavior of these materials in various applications. The chapter concludes by summarizing the key takeaways and highlighting the significance of the knowledge presented in this chapter for the rest of the thesis.

3

Introduction to Flux Pump Technologies

3.1 Importance of flux pumps for superconducting magnets

3.1.1 Superconducting magnets

Superconductors can transport high-density direct currents with negligible Joule loss. They are ideal for high-field magnets due to this outstanding property. Magnetic resonance imaging (MRI) [17], nuclear magnetic resonance (NMR)[18], and magnetic levitation devices [83, 84, 85], etc., are only a few applications where superconducting magnets have been extensively used [15, 86]. A greater magnetic field allows for a higher resonance frequency, higher resolution, more clearly defined chemical shift spectra, and a higher data acquisition rate in MRI/NMR. Low Temperature Superconductors (LTS) such as NbT_1 and Nb_3Sn usually have a much lower upper critical field B_{c2} than High Temperature Superconductors (HTS) as shown in Figure 3.1.

LTS are affordable, manageable, and provide sufficient fields for MRI and NRM applications. As a result, NbT_1 is still frequently utilised to produce the background field in such commercial applications. The field strength is often greater than in MRI to attain a higher resonance frequency in NMR. A 900 MHz NMR, which needs 20 T, is still relatively common, and Nb_3Sn can produce this magnitude of magnetic field. However, 1.3 GHz NMR requires

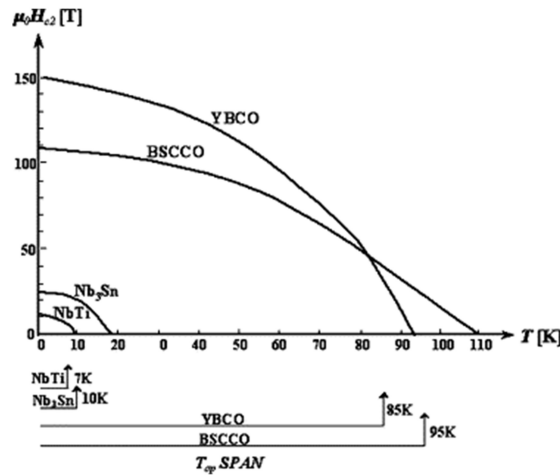


Figure 3.1: Critical field vs temperature plot for low temperature superconductors and high temperature superconductors [16].

a field greater than 30 T, which is greater than the top critical field of Nb_3Sn . The current design employs an LTS magnet to establish a background field of (>20 T) within its bore, and it incorporates an HTS magnet as an insert to generate an additional field exceeding 10 T under these conditions, where the use of HTS is essential [87].

Additionally, superconductors enable the generation of exceptionally high magnetic fields for projects. The National High Magnetic Field Lab (NHMFL) in the USA stated that they were able to attain a consistent magnetic field of 45.5 T by utilizing a hybrid magnet that combines resistive and HTS materials [88]. However, this is not the limit for HTS, and their next objective is to construct a fully superconducting magnet of 60 T.

3.1.2 Persistent current operation of superconducting magnets

Superconductors must carry a large current for superconducting magnets to produce a high magnetic field. Utilising external power sources and current leads is one way of powering superconducting magnets [88]. The electronic power supply delivers a constant current to the magnet through a pair of current leads. This method has a number of shortcomings. Foremost, the continual current generates a continuous loss in the current leads. Furthermore, the stability

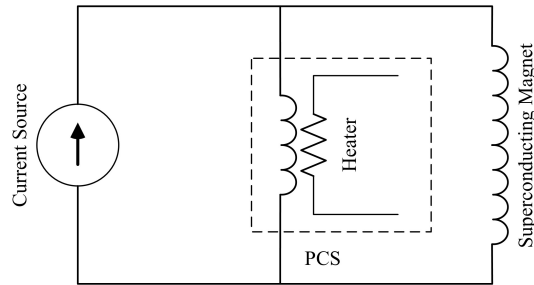


Figure 3.2: Circuit diagram of superconducting magnet operated in a persistent current mode. The PCS drives the superconductor to the normal state and charges the magnet. Once the magnet is fully charged, the superconductor in the PCS is cooled down to a superconducting state, allowing persistent current to flow in the magnet.

of the magnetic field is constrained by the stability of the power supplies, making it difficult to improve the stability of the field. External power supplies are unable to achieve the required field stability of 0.1 ppm/h or higher for applications like MRI/NMR. Therefore, in MRI/NMR, the LTS magnet normally works in persistent current mode [89]. The magnet's terminals are shortcircuited by a Persistent Current Switch (PCS), to operate a magnet in a persistent current mode [89, 90, 91]. A persistent current switch usually employs a heating element to drive the superconductor to the normal state. Figure 3.2 illustrates a superconducting magnet operating in the persistent current mode. During the charging process of the magnet, the superconductor in the switch is heated above its critical temperature, causing it to lose its superconductivity. Once it becomes normal, a voltage is developed across the switch to charge the magnet. The switch's superconductor is cooled to regain superconductivity when the magnet is fully charged. In LTS persistent current switches, the joint resistance can be developed in order of $10^{-13} \Omega$ [92, 93]. As a result, there is almost no degradation in the transport current as it flows through the magnet. LTS magnets can provide an incredibly steady magnetic field due to persistent current operation, which is essential for NMR/MRI.

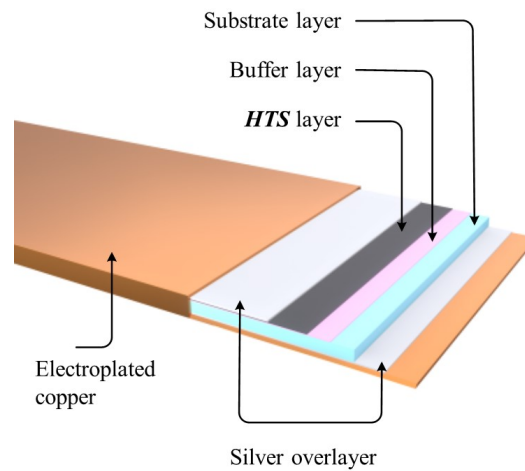


Figure 3.3: Architecture of standard HTS coated conductor.

3.1.3 Flux leakage in HTS magnets and flux compensation by flux pumps

Ideally, an HTS magnet should operate in a persistent current mode, but several problems must be solved before achieving the persistent current operation of HTS magnets. HTS are typically compounds, as compared to low-temperature superconductors. They are normally manufactured as Coated Conductors (CC) with multilayer structure, as illustrated in Figure 3.3, which includes a high temperature REBCO/YBCO layer, a substrate (Hastelloy) layer, a buffer stack layer, two silver overlays and two electroplated copper layers [94]. These layers enhance the mechanical strength and electrical stability of HTS CCs.

A low resistance joint between the HTS-CC is challenging to achieve because of the presence of the other metal layers. Joint resistance values between CCs are often measured in the tens of nano-ohm range [22], which is too high for persistent current operation. Although recent research [23] asserts that a joint resistance of less than $10^{-17}\Omega$ between CCs is made, no repeatable results have been presented. Even if this claim is valid, the manufacturing methods are noticeably too complex for engineering use.

Flux creep is the additional source of flux leakage [75]. Flux creep will result in a transport loss in superconducting magnets. HTS are quite susceptible to this phenomenon, which causes their n -value to be relatively low. A DC HTS magnet will produce a significant transport loss

Step 1: On approach, the flux source (moving magnet) generates a normal region at the edge of the superconductor, equal to the opening of the switch S1. If there is an existing current in loop 2, it flows through switch S2. Since L1 is open, there is no induced current in loop 1. Hence there is no change in magnetic flux in loop 2.

Step 2: When this normal region reaches the centre of the superconductor, both S1 and S2 switches are closed. There is still no change of magnetic flux in loop 1 and, therefore, no current induced in it. Similarly, loop 2 remains unchanged during step 2.

Step 3: When this normal region reaches the inner edge of the superconductor, switch S2 opens. There is no magnetic field change in either loop 1 or 2. However, the flux in loop 2 is increased by the approaching flux ($-\Delta\Phi$) (this flux is the moving magnet from step 1).

Step 4: This is the most important and the final step of the flux pumping cycle, here the flux source leaves the superconductor. On exit it removes the flux by ($-\Delta\Phi$) in the loop 2, according to Faraday's law, a current I must be induced to maintain the magnetic flux stability inside the superconducting loop. This induced current is added to the existing current to counteract the change in magnetic flux. Compared to the magnetic flux at the start of the cycle, the flux increases by ($-\Delta\Phi$) inside the superconducting loop.

3.2.1 The flux compressor

The possibility of trapping magnetic fields, even with excellent homogeneity, inside superconducting cylinders is exploited by mechanically driven flux compressors. The field strength can be improved by narrowing the area where the flux can be trapped. A block of superconducting material is used for this, e.g., Nb or sintered Nb₃Sn with a narrow slot that connects two cylindrical holes. The compressor is cooled below its critical temperature, typically to 4.2 K and placed in an external magnetic field parallel to the axes of holes. When the superconducting piston is inserted into hole A, the flux is expelled, and this expelled flux causes an increase in flux density in hole B. The expression for flux density can be given as

$$B_{final} = \frac{\text{area before insertion}}{\text{area after insertion}} \cdot B_{initial} - B_{losses} \quad (3.1)$$

The term B_{losses} refers to the deviation from the ideal compression ratio. The superconducting piston performs mechanical work and is transformed into magnetic energy and stored in the compressor's empty space. Any desired compression ratio can be achieved by adjusting the hole areas, provided it does not exceed the limits of critical density, flux flow dissipation, and flux jump phenomena.

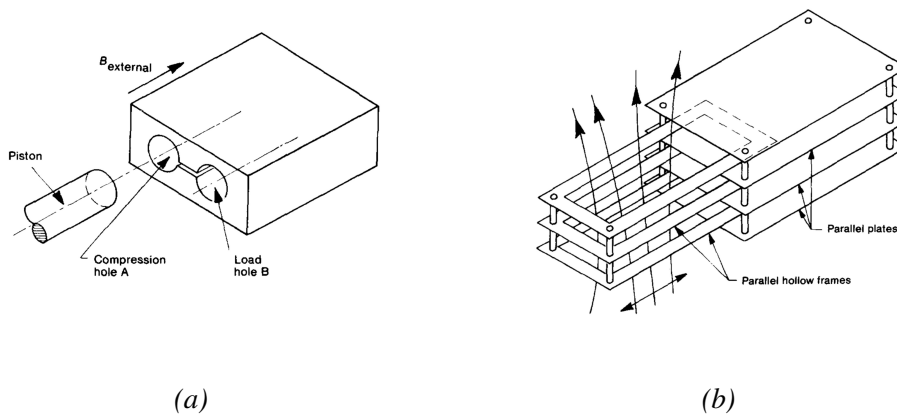


Figure 3.5: The flux compressors, (a) cyclic flux compressor and (b) stepless regulable flux compressor.[25]

The aforementioned demonstrates discontinuous changes in the trapped flux density. However, if the area of the trapped flux is constantly variable, stepless regulation of a flux compressor is achievable. This can be accomplished by using several parallel hollow frames that are only partially covered, as illustrated in Figure 3.5b. Initially, the device made out of this principle reached 70 mT; later, it was shown that it can achieve a field up to 270 mT.

Improving the field stability against flux jumps can lead to the development of flux compressors. A disadvantage is the requirement for mechanical work in the helium bath. Also, handling the strong forces inside and between the various sections is challenging. The shortcomings of these inexpensive, potentially attractive devices, prevented their acceptance for widespread use..

3.2.2 A dc dynamo

The primary attribute of this type of flux pump is the transformation of mechanical energy into electromagnetic energy. All dc dynamos have a superconducting sheet as a “pump bridge” connected across a magnet or coil acting as load in common. These flux pumps work by “moving” flux into a superconducting loop without producing significant inductive eddy currents or negative voltages. This flux is then withdrawn naturally, causing the load current to be generated and accumulated again after every pump cycle because of flux conservation. In Figure 3.6a, a magnet travels from A to B, forming a normal region that encloses the flux (Φ) if the local magnetic field exceeds the sheet material’s critical value. During the passage of the normal spot across the sheet, if the spot dimensions are lower than those of the sheet, the superconducting loop short circuiting the load coil is not interrupted.

The induced eddy currents in the normal region are short circuited mainly because the normal spot is surrounded by superconducting material, leaving only a small negative voltage at the edge of the pump bridge. At point B, the electromagnet is either turned off or moved away via a different path, such as over the leads of a hard superconductor, to remove the flux. This results in a significant positive induction voltage, which increases the load current. Each cycle’s current increase is even doubled by changing the magnetic field’s polarity at point B before returning to point A. Starting at A, the pump cycle may be repeated.

For each cycle, under ideal conditions, the trapped flux increases by the amount of flux contained within the normal spot. In practice, several loss mechanisms operate around the sheet’s normal region, resulting in a saturation effect. The load current and voltage curve of the dynamo, can be given as [25]

$$V_{load} = f\Phi_0 - 2flI_{load} - f^2\Phi_0\frac{l}{R} \quad (3.2)$$

$$I_{load} = \frac{\Phi_0}{2l} \left[1 - e^{(-\frac{2fl}{L})t} \right] \quad (3.3)$$

Here, V_{load} represents the voltage across the load, I_{load} signifies the current in the load, f stands for frequency, l represents length, while R and L respectively denote resistance and

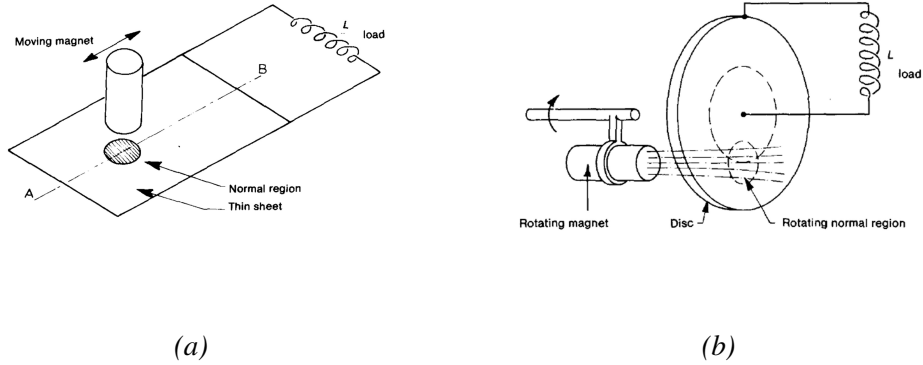


Figure 3.6: The superconducting dc dynamos, (a) simple dc dynamo and (b) axial geometry dc dynamo.[25]

load inductance.

In equation 3.2, the positive induction voltage is represented by the first term, the switching voltage drop caused by the moving normal spot by the second term, and the incomplete short circuiting of the generated eddy currents in the normal region by the third term.

3.2.3 Rectifier type flux pumps

In superconducting dynamo-flux pumps, the flux containing the moving normal region works as both a flux source and a “switch” simultaneously. Employing another source of flux can separate these functions, such as an electrical transformer. Some of the subsequently created devices are superconducting versions of well-known conventional rectifier circuits. This analogy is shown in Figure 3.7, where the new circuit is comprised of a transformer, at least two switches that function as diodes, and a load coil built up in two loops. The periodic current generated by these two alternative superconducting loops is ensured to be accumulated rather than dissipated. This is a key difference from conventional rectifiers.

The operation of the transformer rectifier can be explained in two steps:

Step 1: In the first half, the current is induced in the secondary loop and the load via switch 1 and 2 is kept open.

Step 2: In the second half of the switching process, 2 is closed, providing the return path

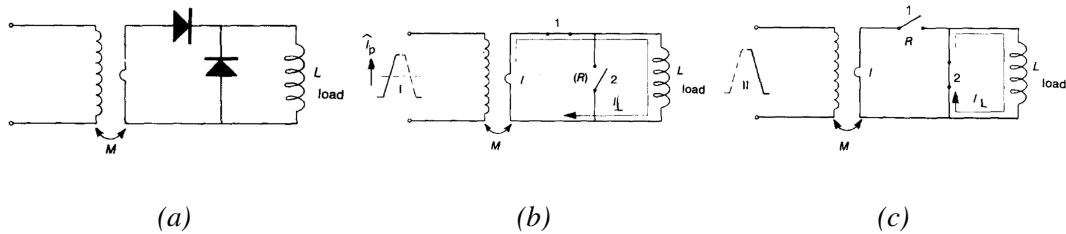


Figure 3.7: Normal conducting half wave rectifier [26], (b) superconducting rectifier pump half cycle, (c) reset half cycle.

to the load current and switch 1 is open, ensuring the flux conservation.

3.3 High temperature superconducting flux pumps

Recently, two major types of HTS flux pumps have been developed, namely HTS travelling magnetic field induced flux pumps (an HTS dynamo [34, 98, 99, 100], linear flux pumps [101, 102, 103, 104, 105, 106]) and HTS transformer-rectifier type flux pumps (thermally switching [107, 108, 109], dynamic resistance switching [110, 111, 112, 29, 113], $J_c B$ switching [114, 115], and self switching type flux pumps [116, 117, 118]). The HTS travelling wave flux pumps bear resemblances to LTS dynamo flux pumps in terms of their structures, while the HTS transformer-rectifier flux pumps share similarities with LTS transformer-rectifier flux pumps. Nevertheless, a significant distinction between them lies in the utilization of YBCO tape in HTS flux pumps, which possesses an upper critical field exceeding 100 T [119]. Unlike LTS tape, where a normal spot can be easily generated by employing a permanent magnet with a field of approximately 1.0 T, such an occurrence is unattainable in YBCO tape. Therefore, the working principles of HTS flux pumps differ significantly from those of LTS flux pumps.

3.3.1 Travelling magnetic field Induced flux pumps

Principle of HTS travelling wave flux pumps

The understanding of HTS travelling wave flux pumps and their DC output on a single YBCO stator is more complex compared to the HTS transformer-rectifier flux pumps, which have clear circuit models and switching mechanisms (will be discussed later in detail). In order to understand the source of the open-circuit voltage in HTS travelling wave flux pumps, a circuit model [106] was introduced, illustrated in Figure 3.8. The model consists of two parallel branches (ab and dc). As the magnetic flux traverses this loop, the associated terminal voltage $v(t)$ is obtained as per the following derivation

$$v(t) = \frac{1}{T} (p_{dec} - p_{inc}) \Delta\Phi \quad (3.4)$$

$$p = \frac{R_2(t)}{R_1(t) + R_2(t)}$$

Where p_{inc} is for increasing, p_{dec} is for decreasing magnetic flux Φ , and $\Delta\Phi$ is for peak applied magnetic field. If there is an imbalance in the resistances of the two branches during

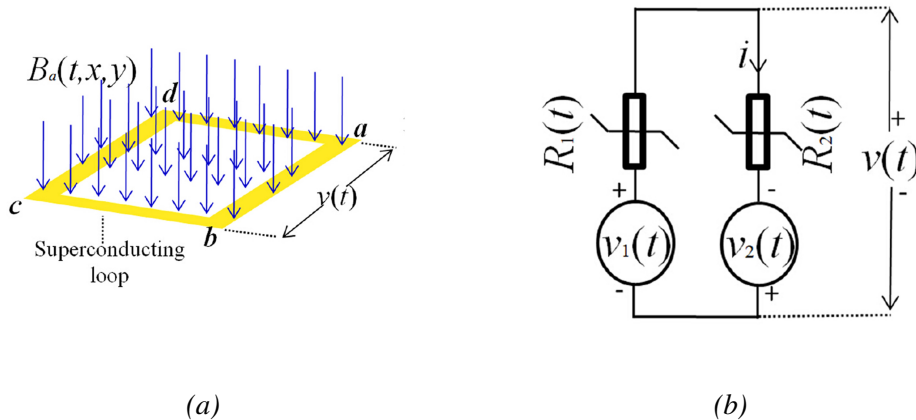


Figure 3.8: Schematic drawing of open circuit voltage of travelling wave flux pump [106].

the decrease and increase of the magnetic flux Φ (i.e., $p_{inc} - p_{dec} \neq 0$), a DC output voltage will be generated in each cycle.

HTS dynamo type flux pump

Hoffmann et al. originally proposed a rotating travelling wave flux pump, also known as the HTS dynamo [34, 120]. Rotating permanent magnets are used in this type of flux pump to generate the travelling magnetic field. Several permanent magnets are uniformly fixed on a spherical disc with the same field polarity facing outward, as seen in Figure 3.9. The motor rotates the disk around the shaft at its centre. Each magnet will move over a superconducting sheet as the disc spins. Consequently, a travelling magnetic wave is experienced by the sheet, and a dc voltage will emerge. Thus the dc current in the superconducting magnet starts to ramp up until it reaches its steady-state value.

The output voltage-current curves of an HTS Dynamo were measured by researchers from Victoria University Wellington, New Zealand [36]. They found that a resistance that was two orders higher than the total resistance in the circuit reduced the maximum possible load current and attributed it as a “dynamic resistance”. Numerous aspects that affect the flux pump’s performance have been studied, including the flux gap [121], operating frequency

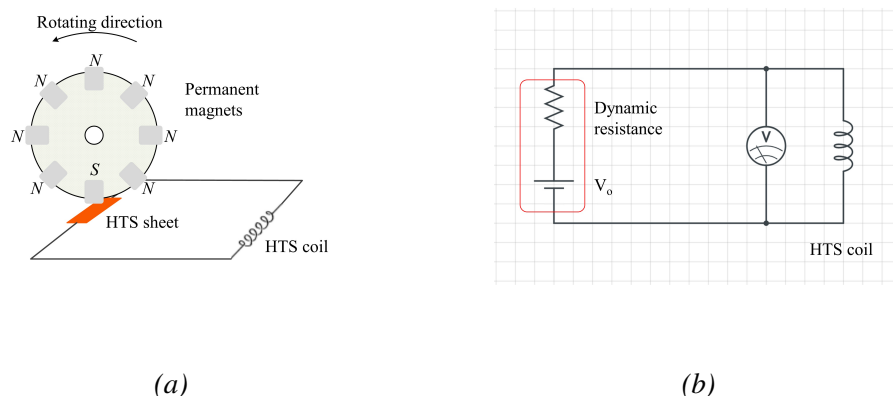


Figure 3.9: HTS dynamo type flux pumps, (a) schematic drawing of rotating permanent magnet based flux pump and (b) circuit diagram of the setup employing HTS sheet (red box) and HTS coil.

[122], stator wire width [98], and magnets' geometry [123]. Additionally, a through-wall excitation system [124] was created, demonstrating how the flux pump may be taken out of the cryogenic system, it made flux pumps more practical.

Hoffmann provided an explanation of the flux pump's workings [34]: flux will be "dragged" across the wire by the magnets if the magnetic field is strong, and the wire will expel flux if the field is weak. Chris et al. presented a more detailed explanation of HTS dynamo [37], which states that screening current follows the position of the magnet. When magnets rotate, the relative position between the magnet and the HTS sheet changes, which alters the screening current's forward and backwards path and produces a rectifying effect.

Linear travelling wave flux pump

An electromagnet is used by Bai et al. [32, 125, 126] to generate a linear travelling magnetic wave. The flux pump comprises copper windings and an iron yoke with several poles, as seen in Figure 3.10. The copper windings link the iron poles. Alternating current is used to power the windings in sequence so that a travelling magnetic wave can be produced in the gaps between the poles. An HTS sheet is inserted into the gap to short a superconducting coil. The load connected to the sheet can gradually energise when it encounters a travelling

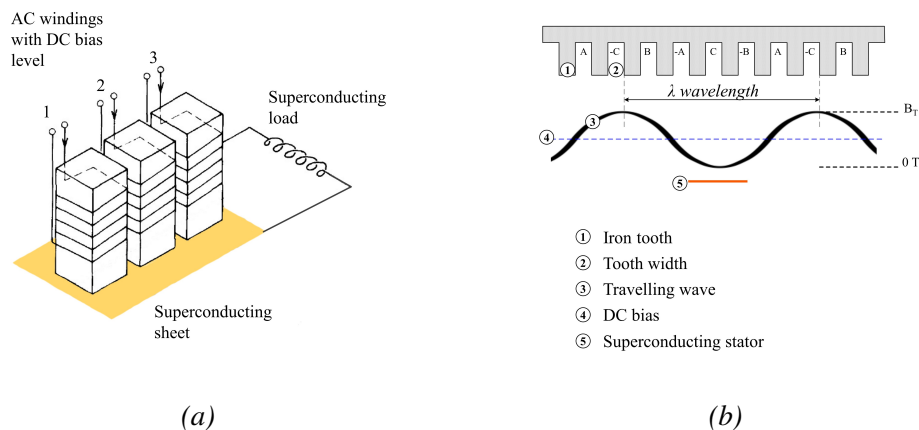


Figure 3.10: Linear travelling wave flux pumps, (a) schematic drawing of the linear travelling wave flux pump and (b) the wavelength of the travelling magnetic field produced by the linear motor flux pump can be adjusted using different designs for the iron teeth and slots.

magnetic field. Fu et al. developed a linear flux pump similar to Bai's flux pump [127, 33] in which several parallel HTS tapes as a stator are used instead of a sheet.

The mechanism of these flux pumps has not been adequately explained, despite the fact they can inject flux into superconducting circuits. Bai et al. [32] describes it as the travelling magnetic wave creating a moving normal spot in the superconducting sheet, which is identical to LTS flux pumps. The explanation disregards the fact that their experiment's field magnitude is too small to disrupt the superconductivity of HTS sheet.

3.3.2 Rectifier type flux pumps

To date, a comprehensive understanding of the working principle of HTS rectifier type flux pumps has been achieved. These pumps employ the same electric circuitry as LTS transformer rectifier flux pumps. However, a crucial distinction arises in the "switching" mechanism. In contrast to LTS transformer-rectifier flux pumps, which transition the LTS wire from a superconducting state to a normal state, HTS rectifier flux pumps leverage the resistive flux flow state of YBCO tape to switch the HTS tape from a superconducting state (closed switch) to a resistive state (open switch).

Dynamic resistance in type-II superconductors

Prior to delving into rectifier type flux pumps, it is essential to first gain a comprehensive understanding of the dynamic resistance that arises from AC magnetic fields in type II superconductors. Dynamic resistance, as documented by Ogasawara et al. (1976), Uksusman et al. (2009), and Oomen et al. (1999) [128, 129, 110], manifests in high temperature superconductors that carry direct current while being exposed to an AC magnetic field perpendicular to the direction of the current. The underlying physics of dynamic resistance pertains to the hysteresis magnetization behaviour observed in HTS.

Figure 3.11a depicts a slab-shaped type II superconductor carrying a direct current (I_t) and exposed to a perpendicular AC field (B), with dimensions of width (a), length (w), and thickness (l) such that $a \ll w$ and $a \ll l$. At low field intensities, the field cannot penetrate

the transport current, leading to pure magnetization loss. However, at high field intensities, where the induced current and transport current can occupy the entire superconductor, the situation is different, as shown in Figure 3.11b. During an increasing field, most of the flux enters the superconductor from the left edge, and during a decreasing field, most of the flux exits the superconductor from the right edge. The flux central line, marked by the blue-dash lines in Figure 3.11b and referred to as such by Oomen et al. (1999), represents the boundary of transport current in the superconductor, indicating the point where the electric field equals zero and no flux can cross [110]. The position of the flux central line changes during the field-increasing and field-decreasing process, resulting in a net flux flow across the superconductor. The shaded area in Figure 3.11b shows the flux flow across the superconductor per unit length during each field cycle, and the total flux flow across the superconductor can be expressed as

$$\Phi_{per-cycle} = 2(B_a - B_{a,th})aI_t w / I_c \quad (3.5)$$

In Figure 3.11b, the threshold field ($B_{a,th}$) represents the minimum field intensity required to initiate interaction between the applied field and the transport current in the superconductor. This value needs to be surpassed to enable such interaction. The transport current is the current flowing through the superconductor, and (I_c) is its critical current. As a result of the

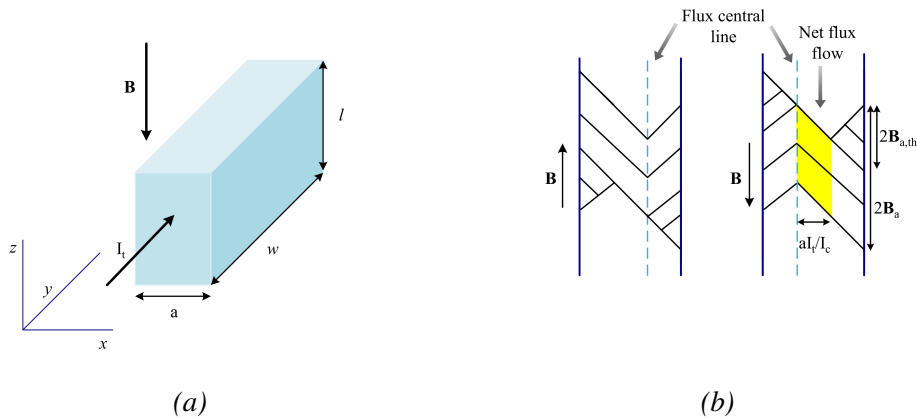


Figure 3.11: (a) The field distribution inside a slab-like superconductor subjected to an AC magnetic field and carrying a DC transport current, as per the Bean model, (b) the presence of the DC transport current leads to an asymmetric field profile within the slab.

net flux flowing across the superconductor, a direct current (dc) voltage is generated across the superconductor in accordance with Faraday's law. This dc voltage has the same direction as the transport current and can be expressed as

$$V_{DC} = f\Phi_{per-cycle} = 2f(B_a - B_{a,th})aI_t w / I_c \quad (3.6)$$

Where f is the applied field frequency. The voltage over the transport current is equal to the equivalent resistance which is defined as a dynamic resistance

$$R_{dyn} = \frac{V_{DC}}{I_t} = \frac{2awf(B_a - B_{a,th})}{I_c} \quad (3.7)$$

In [130], the dynamic resistance expression is derived for thin superconducting sheets with $a \gg l$. On the other hand, in [110], an analytical expression for dynamic resistance is presented for high applied magnetic fields, which takes into account the field-dependence of critical current density.

$$R_{dyn} = \frac{2awf}{I_{c0}}(B_a + cB_a^2) \quad (3.8)$$

The parameter c in this equation relates to the dependence of critical current density on the applied magnetic field. When modeled using Bean's model, c is equal to 0. The critical current of the superconductor without an external field is represented by I_{c0} .

The dynamic resistance, as depicted in Equation 3.8, exhibits a direct proportionality with the field frequency and a positive correlation with the field strength. This intriguing characteristic may allow for its application as an AC field controlled persistent current switch.

Alternating field switching flux pump

Geng et al. proposed this design of a flux pump [29], in which an ac magnetic field regulates the resistance of the HTS sheet [116] and HTS sheet acts as a resistive switch. A high magnitude, low frequency alternating current is induced in the superconducting loop. The rectification is performed by applying the high-frequency ac signal normal to the HTS tape. This high frequency ac signal interacts with the transport current and induces a net flux flow

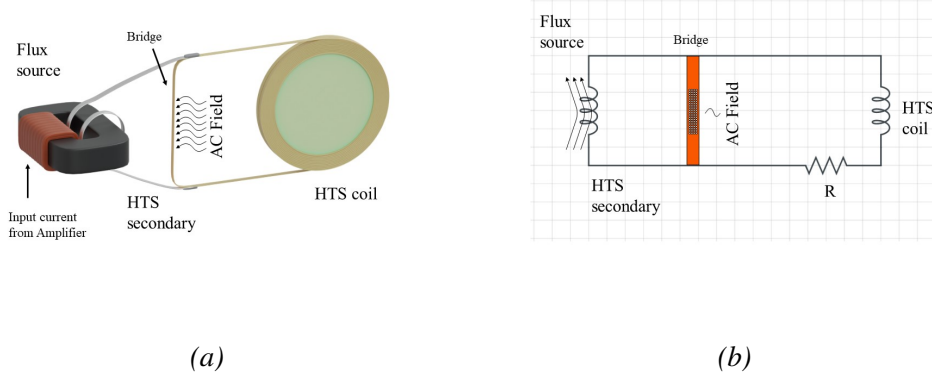


Figure 3.12: Alternating field switching flux pump, (a) schematic drawing of the ac field switched flux pump, in addition, the ac field is applied so that the flux flow into the HTS coil (load coil) through the resistive bridge and (b) the circuit diagram of the flux pump where an ac field is applied normal to the surface of the HTS tape to rectify the induced current, the resultant direct current is accumulated into the HTS coil.

across the tape, which in return pumps current into the load. The underlying physics is as follows: when an AC magnetic field is introduced perpendicular to a DC carrying HTS tape, it undergoes flux flow. The transport current's direction only influences the flux flow direction during each cycle of the AC field; it is not polarity-dependent. The flux flow for a DC transport current is always in one direction; as a result, flux accumulates in the load coil. The AC field across the HTS switching tape is intermittently applied whilst the transport current reaches one polarity achieving the unidirectional flux flow in the load coil. The flux flow voltage can be given as

$$V_0 = R_{dyn} (i_p - i_L) \quad (3.9)$$

Where V_0 is the voltage across the HTS tape, R_{dyn} is the resistance due to the applied ac field, i_p is the induced current and i_L is the current in the HTS coil. Similarly, the maximum current injected into the coil can be driven as

$$I_L = \frac{I_p}{1 + \frac{R_L}{R_{dyn} P}} \quad (3.10)$$

Where is I_p the average value of induced current (i_p), P is the duty cycle of the applied field.

J_cB switching flux pump

The studies conducted by Ishmael et al. [28] and Venuturumilli et al. [115] present speculative designs for the HTS flux pump. In the design, switches are made of superconducting tapes. High DC fields are applied to the switch superconductor to operate the switch as illustrated in Figure 3.13. The switch is also known as a DC field controlled HTS switch or J_cB switch. The critical current density of HTS superconductors depends on the external field. The critical current of the superconductor acting as a switch lowers with applied external fields. The process of flux pumping can be achieved by carefully balancing the current capacity of the switch, the applied DC field, and the secondary current. These studies have proposed designs and models for the DC field controlled HTS flux pumps and explained the underlying principles and limitations of this type of flux pump.

Self-switching flux pump

This flux pump does not require any switching component, it exploits the superconducting properties of the HTS tape to achieve the flux pumping phenomenon [116]. The method of

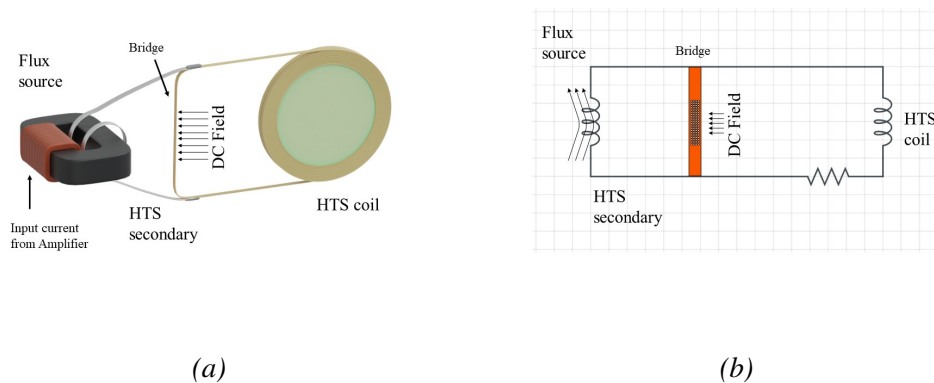


Figure 3.13: J_cB switching flux pump, (a) schematic drawing of the dc field switched flux pump, in addition, the dc field is applied so that the flux flow into the HTS coil (load coil) through the resistive bridge and (b) the circuit diagram of the flux pump where an dc field is applied normal to the surface of the HTS tape to rectify the induced current, the resultant direct current is accumulated into the HTS coil.

switching employed here shares similarities with the overcurrent switch [131] found in LTS transformer-rectifier flux pumps. However, the key difference lies in the HTS bridge operating within the flux flow region instead of being in a normalized state. It induces an asymmetrical alternating current into the superconducting circuit as illustrated in Figure 3.14.

To achieve a net DC current to the load in each cycle, certain conditions must be met. Firstly, the current in branch “ ab ” ($i(t)$) induced by the transformer needs to be asymmetric, while the current I_c of the branch “ ab ” should be significantly smaller than the superconducting secondary of the transformer. As depicted in Figure 3.14b, during the first half cycle, the current $i(t)$ rises rapidly, surpassing the value of I_c in its positive peak region. This renders the bridge resistive, allowing the current to flow towards the load. In the second half cycle, the current $i(t)$ gradually decreases, with its negative peak value remaining lower than I_c , thereby maintaining the bridge in a superconducting state. Consequently, a net DC current is rectified into the load during each cycle. Importantly, the overcurrent switch does not necessitate an external AC field like the dynamic resistance switch does and achieves a self-switching effect. This thesis focuses on these flux pump types, and this phenomenon is discussed in detail in

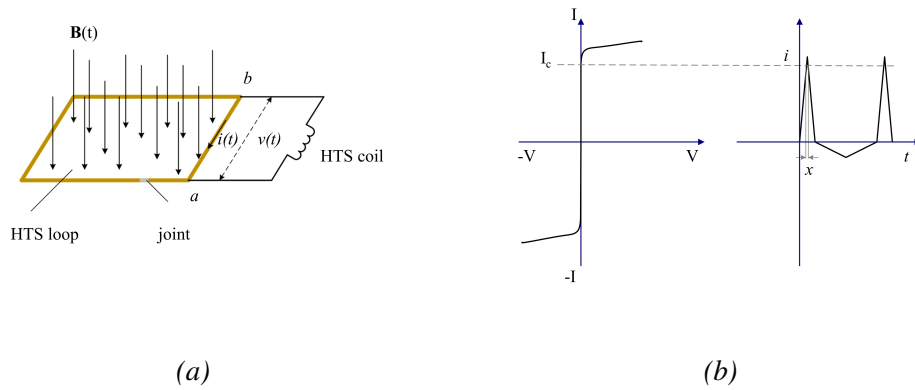


Figure 3.14: Self switching HTS flux pump, (a) A varying magnetic field is applied to an HTS loop which consists of a resistive joint. A superconducting load L is connected to branch ab which has a lower critical current value than the rest of the HTS loop. (b) the V - I curve of branch ab , and one example waveform of the circulating current $i(t)$. During each cycle of $i(t)$, at region A and only region A, the critical current of branch ab has been exceeded, and a voltage developed across the load. For the remainder of the waveform, $abs(i(t)) < I_c$.

later Section.

Thermal switching flux pump

Thermally actuated HTS flux pumps have been widely studied in the literature. Iwasa et al. in their study demonstrated a flux pump with a thermally actuated switch made of YBCO [132]. Similarly, Jeong et al. in their study demonstrated a flux pump using YBCO as the thermally actuated switch [133]. Later in 2005 Oomen et al. demonstrated the use of a thermally actuated switch made of Nb_3Sn superconductor in a HTS flux pump [27]. These studies have demonstrated the potential of using thermally actuated switches in HTS flux pumps, however, one of the main limitations of these flux pumps is their slow operating speed, which is a result of the slow thermal response of the superconductor. Additionally, the use of a thermally actuated switch also adds an additional heat load to the cooling system, which can be a significant limitation in certain applications.

3.4 Operating principle of self-switching flux pump

In section 3.3.2, a concise overview of self-switching HTS flux pumps is presented. This section will delve into a more detailed examination of the components and operation of these flux pumps. As illustrated in Figure 3.15, a self-switching HTS flux pump consists of the following main parts:

1. A transformer, which serves as the source of flux
2. An excitation or charging coil, made of HTS tape, which is typically the secondary coil of the transformer.
3. A load coil, which can be a superconducting magnet.
4. A bridge, made of HTS tape, which connects the charging coil to the load coil.
5. The critical current relationship between the superconducting elements of the flux pump must be such that the critical current of the charging coil is greater than the critical

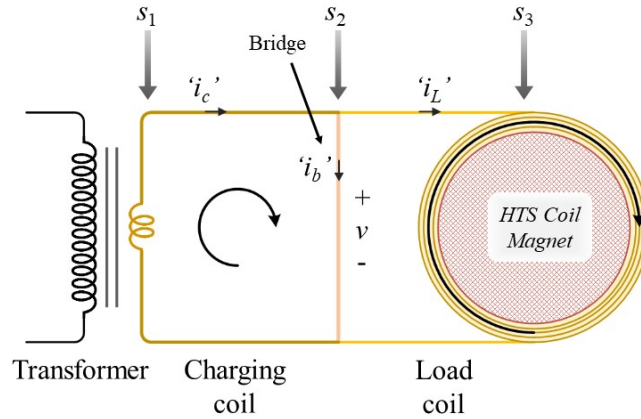


Figure 3.15: Schematic diagram of a self-switching superconducting flux pump, comprising a transformer, a charging coil, a load coil, and a bridge connecting the two coils.

current of the bridge, which is in turn greater than the critical current of the load coil.

An external flux is applied to the charging coil using the transformer, which in turn induces a current in the charging coil. The amplitude of this current is greater than the critical current of the bridge, causing the bridge to open (this phenomenon will be discussed in detail in later sections) and allowing the current to be injected into the load coil. Once the bridge returns to its superconducting state, the current is trapped in the load coil. This process is repeated, resulting in a gradual accumulation of current in the load coil.

3.4.1 Origin of dc voltage in high temperature superconductors

In Chapter 2.2, we discussed the classification of superconductors into Type-I and Type-II. Type-II superconductors, such as HTS with critical temperatures above 30 K, remain in the mixed state above their critical field (B_{c1}) and begin to penetrate it as the field increases until they reach their upper critical field (B_{c2}). When the transport current in an HTS superconductor exceeds its critical current value, the superconductor is forced into the flux flow regime as

illustrated in Figure 3.14b, which generates a DC voltage across the superconductor according to the E - J power law described in Section 2.3.3. The equation for this phenomenon can be given as follows

$$v_{dc} = lV_c \left(\frac{i_b}{I_c} \right)^{n-1}, \quad (3.11)$$

where l is length of the superconductor, I_c is critical current of the superconductor i_b is current flowing through the superconductor and V_c is voltage criterion and n is the exponent of the E - J power law.

3.5 Comparison between HTS flux pumps

HTS flux pumps are an emerging technology currently in development, with significant potential for various applications in the field of HTS magnets. These applications include fusion, particle accelerators, NMR/MRI magnets, superconducting motors, and magnetic levitation, among others. HTS flux pumps can function as wireless DC power supplies, allowing HTS magnets to maintain a quasi-persistent current mode. The promising outlook for HTS flux pumps suggests that numerous new applications will arise in the near future.

Table 3.1: General comparison between HTS flux pumps [134].

Type	Pros.	Cons.	Comments
HTS Dynamo	simple design, easy operation	includes moving parts, a rotating shaft is required to rotate a disc	output DC voltage is relative low (\sim mV)
Linear HTS flux pump	relatively small size, easy field control	the magnetic teeth arrangement similar to linear motor is required	output DC voltage is relative low (\sim mV)
Thermally switched flux pump	easy to operate only requires heaters for switching	adds cooling load on the cryocooling system	low switching speed
AC field switched flux pump	an external field is required for switching	sophisticated system, complex operation consideration	Highly inductive
Self switching flux pump	completely current driven model, no external field required	The Sharp E-J relation of HTS makes it potentially unstable	relatively low efficiency ($<10\%$)
Power electronics switched	requires IGBTs and MOSFETS, cheap and widely available	On-state resistance is inevitable	Technically not a flux pump

3.6 Conclusion

This chapter has provided an overview of the current state of flux pump technology, with a focus on both low-temperature superconducting and high-temperature superconducting flux pumps. The challenges and limitations associated with HTS flux pumps have been discussed, as well as the practical demands for these devices in various applications. The significance and motivation for this work have also been highlighted. It is important to note that this chapter has laid the foundation for the research presented in the following chapters, where the focus is on the design, fabrication, and characterization of a self-switching HTS flux pump, as well as the control strategies used to achieve precise field modulation. The results and findings presented in this thesis aim to contribute to the ongoing efforts to improve the performance and reliability of HTS flux pumps and make them more suitable for practical applications.

4

Modeling and Experimental Analysis on a Self-Switching Rectifier Flux Pump

4.1 Introduction

A self-switching flux pump operates without the use of external switching components. It utilizes the superconducting properties of HTS tape to achieve the flux pumping phenomenon. It drives HTS above its critical current value to induce flux flow resistivity. The phenomenon of flux flow resistivity has been observed in HTS-CCs when exposed to an AC field, carrying an AC current, or carrying a DC current above their critical current. This unique flux flow behavior holds potential for flux pumping applications, originally proposed by Laquer and Giaever for LTS [131, 135]. Similar to the LTS flux pump [131], Geng et al. proposed a self-switched HTS flux pump that works by driving the HTS-CC into the flux flow region of the E - J curve by injecting current above its critical current value [116]. While previous studies have used straight HTS tapes, known as “the bridge,” in a single or parallel configuration to pass high currents, this study demonstrates flux pumping using a non-inductive bifilar coil as a bridge. This configuration enables higher and more stable DC voltages while the superconductor is subjected to the flux flow regime, resulting in a higher load current. Additionally, the bifilar bridge allows for a compact size magnet with a neatly wound bridge

across the magnet, making it a suitable candidate for complex applications like rotating machines.

4.2 2-D simulation of self-switching flux pump

4.2.1 2D H-formulation

The numerical model adopted in this thesis to predict the electromagnetic behaviour of the HTS flux pump is based on the solution of a set of Maxwell's equations in 2D using the H formulation [136, 137, 138, 139, 140, 141, 142]. The software package used was COMSOL Multiphysics v5.5 AC-DC module. In H formulation the methods can converge easily compared to other modelling techniques. Moreover, it is simple to set the boundary condition whether it is current flowing in the superconductor or externally applied magnetic fields. The modelling space is typically divided into two subdomains i.e. superconducting region and air. The other metal layers found in the coated conductors are defined respectively. A set of partial differential equations (PDEs) is defined in each subdomain, sharing the same dependent variables. The constitutive law

$$\mathbf{B} = \mu_0 \mathbf{H}$$

is applicable in the space for both air and superconducting subdomain, the relevant Maxwell's equations are

$$\nabla \times \mathbf{E} = -\frac{d\mathbf{B}}{dt} = -\mu_0 \frac{d\mathbf{H}}{dt} \quad (4.1)$$

$$\nabla \times \mathbf{H} = \mathbf{J} \quad (4.2)$$

The E-J characteristics of a superconductor are modelled assuming;

1. The electric field is always parallel to the current density.

2. The power law relationship

$$E = E_0 \left(\frac{J}{J_0(B)} \right)^{n-1} \frac{J}{J_c}$$

Where E_0 donates the threshold electric field is used to define the critical current density J_c and is given as 10^{-4} Vm^{-1} .

The original Bean model assumes $n \rightarrow \infty$ and a voltage criterion $E_0 = 1\mu\text{Vcm}^{-1}$, therefore the power law model is more suitable because a constant $n = 21$ is assumed that is typical value of melt processed YBCO [143, 137].

H formulation in cartesian coordinates

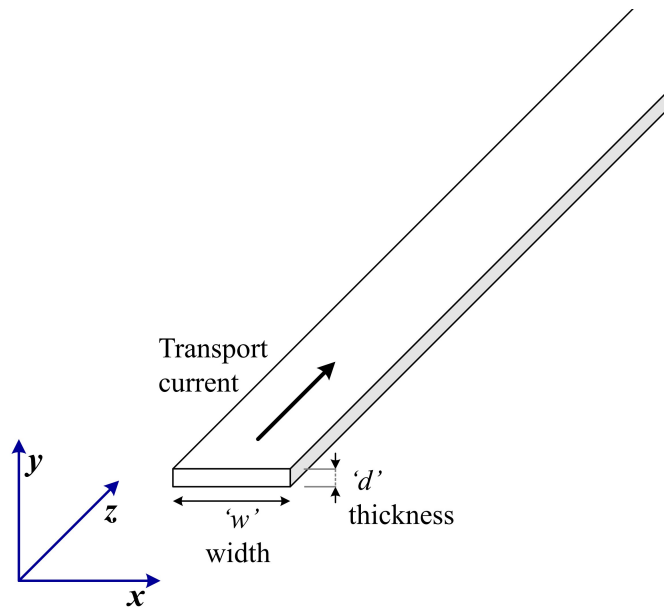


Figure 4.1: Illustration of HTS coated conductor in a FEM model using H formulation

The space is assumed to be infinitely long in the z -coordinate, and the HTS tape sample is also considered as infinitely long of a rectangular cross section $w \times d$. The current density \mathbf{J} only flows in the z direction, while the magnetic flux is located in the $x - y$ plane. Figure 4.1 illustrates the concept in graphic form.

Thus, Maxwell's equation becomes

$$J_z = \frac{dH_y}{dx} - \frac{dH_x}{dy} \quad (4.3)$$

$$-\frac{dE_z}{dx} = -\mu_0 \frac{dH_y}{dt} \quad (4.4)$$

$$\frac{dE_z}{dy} = -\mu_0 \frac{dH_x}{dt} \quad (4.5)$$

COMSOL can solve this problem using these two PDEs and appropriate boundary conditions, with the two dependent variables H_x and H_y . The PDE, “ Δu General Form PDE (g)” subdomain settings in COMSOL, which are suitable for non-linear PDEs, adhere to the following convention [143, 144, 145, 137]

$$e_a \frac{d^2 \mathbf{u}}{dt^2} + d_a \frac{d\mathbf{u}}{dt} + \nabla \cdot \Gamma = F \quad (4.6)$$

where \mathbf{u} is

$$\mathbf{u} = \begin{bmatrix} H_x \\ H_y \end{bmatrix}$$

\mathbf{u} is a vector of dependent variables, e_a is mass coefficient in a matrix form, d_a is the damping coefficient, F is the source term and Γ is known as flux vector. These vectors can be a function of spatial coordinates, the solution \mathbf{u} , and the space and time derivatives of \mathbf{u} . Combining with the previously stated Maxwell's equations, the subdomain setting to be used in COMSOL can be achieved.

$$\begin{bmatrix} 0 & 0 \\ 0 & 0 \end{bmatrix} \frac{d^2 \mathbf{u}}{dt^2} + \begin{bmatrix} \mu_0 & 0 \\ 0 & \mu_0 \end{bmatrix} \frac{d\mathbf{u}}{dt} + \nabla \cdot \begin{bmatrix} 0 & E_z \\ E_z & 0 \end{bmatrix} = \begin{bmatrix} 0 \\ 0 \end{bmatrix} \quad (4.7)$$

The simplest case, in which transport current flows and no external magnetic field is present, is formed by a Dirichlet boundary condition at infinity. The following continuity equation is used at the boundary between air and superconductor.

$$n \times (\mathbf{H}_1 - \mathbf{H}_2) = 0 \quad (4.8)$$

To implement it in COMSOL, a Neumann boundary condition is applied at the superconducting surface. This means the tangential component of the magnetic field intensity is conserved on either side of the material interface. Alternatively, it can be expressed as

$$\frac{dH_{t1}}{dn} = 0, \quad \frac{dH_{t2}}{dn} = 0 \quad (4.9)$$

where H_{t1} and H_{t2} are the tangential components of the magnetic field at the surface of materials 1 and 2, respectively. Under these boundary conditions, COMSOL is used to solve the PDEs. Scalar expressions need to be defined to set these equations up in COMSOL.

1. J_z is defined by as

$$\mathbf{d}(H_y, x) - \mathbf{d}(H_x, y)$$

2. Resistivity of superconductor ρ_{sc} is defined as

$$\rho_{sc} = \frac{E_0}{J_c} \left(\frac{|J|}{J_c} \right)^{n-1}$$

3. The electric field E_z is defined for superconducting subdomain by the expression

$$\rho_{sc} \cdot J_z$$

4. The electric field E_z for air subdomain is defined as

$$\rho_{air} \cdot J_z$$

where ρ_{air} is constant (e.g. $2 \times 10^{14} \Omega\text{m}$).

Applied Current: The current flowing in the superconductor is constrained. This is done by creating a Subdomain Integration Variable I_{int} to ensure the current flow is limited to the superconductor subdomain. The applied current can be either AC, DC or custom defined.

Thus,

$$I_{int} = \iint J_z dx dy = \int_s J_z ds$$

where s is the cross-section of the superconducting domain. This is used as a boundary or point setting to limit current flow to the superconductor.

External Magnetic Field: An external magnetic field can be applied to the superconductor by modification of the Dirichlet boundary condition. The Dirichlet boundary condition is revised for an applied transverse magnetic field of constant magnitude such that

$$H_x = H_{ext} \left(1 - e^{-\frac{t}{\tau}}\right)$$

where H_{ext} is the magnitude of the field and τ is the time constant, a ramp function is applied because a step function may not be applicable here due to the initial boundary conditions and to apply a DC field instantaneously is not physical. Similarly, for the parallel magnetic field, the Dirichlet boundary condition is modified for the y axis i.e.

$$H_y = H_{ext} \left(1 - e^{-\frac{t}{\tau}}\right)$$

An alternating magnetic field can be applied in the same way by modifying the term

$$\left(1 - e^{-\frac{t}{\tau}}\right) \longrightarrow \sin(2\pi ft)$$

where f is the frequency of the applied field in Hz.

The H formulation can be used to analyse the electromagnetic characteristics of the single superconducting tape under an external magnetic field or applied current in both time-constant and time-varying conditions.

4.2.2 Geometrical description

This section describes the 2D simulation techniques used to develop a 2D model of an HTS flux pump. Our modelling approach is similar to the one presented by Zhou et al. in [118],

which follows the modelling strategy similar with the approach developed by [146]. In this model, the flux pump circuit consists of two loops:

1. The excitation or charging loop.
2. The load loop.

The model allows us to analyze the performance of the flux pump under different operating conditions and design configurations. By comparing the simulation results with experimental measurements, we can validate the accuracy of the model and identify potential improvements to the design.

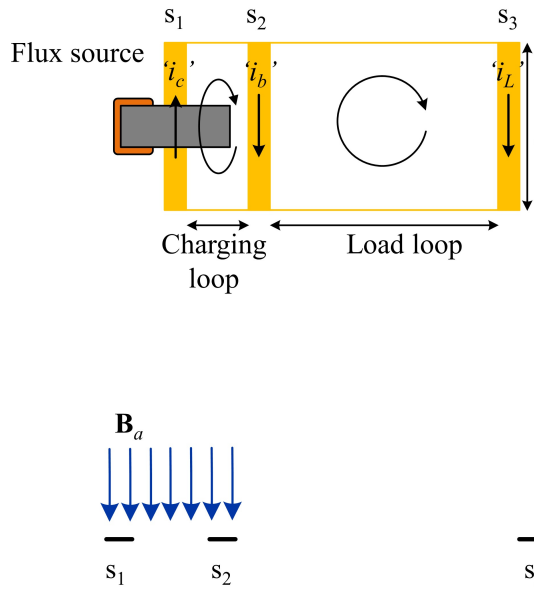


Figure 4.2: Schematic of the 2D HTS flux pump model. The model consists of three parallel thin superconducting strips, with their terminations connected to form two loops: a smaller charging loop and a larger load loop. The applied field is perpendicular to the charging loop area. Flux pumping is considered to occur if the load loop current gradually increases. Bottom shows a cross-sectional view of the model.

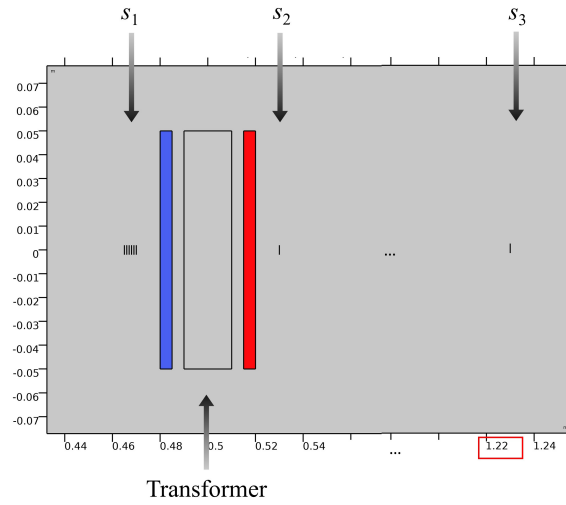
The excitation and load loops are connected at a terminal referred to as the ‘bridge.’ The 2D model in COMSOL consists of three strips of HTS tape, as illustrated in Figure 4.2. These strips are labeled s_1 , s_2 , and s_3 , and the currents in each strip are denoted by i_c , i_b , and i_L ,

respectively. The loop formed by strips s_1 and s_2 is referred to as the charging loop, while strip s_3 is kept far from the rest to form a larger load loop. We assume that the load loop is much larger than the charging loop, and the magnetic field is applied only in the area of the charging loop, perpendicular to the page. By converting the problem to 2D, we can analyze the flux pumping that occurs when the magnetic field is applied to the charging loop and the load current gradually increases.

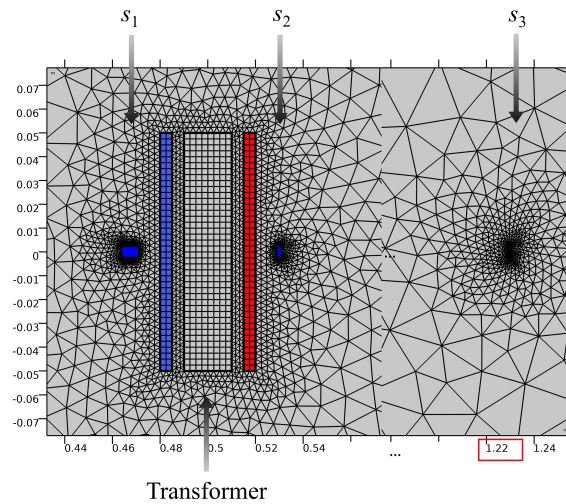
4.2.3 2D FEA modeling of HTS flux pump

To build a 2D model of an infinitely long (into the page) HTS flux pump, we use the built-in partial derivative equations (PDE) Physics in COMSOL Multiphysics. The geometry of the model is illustrated in Figure 4.3. In order to meet the critical current requirement of the charging loop (s_1), we use six parallel strips. The charging loop (s_1 and s_2) is modeled with a single 4 mm HTS strip, while the load loop (s_3) is also modeled using a single strip. s_1 and s_2 are placed across the flux source (transformer), and s_3 is placed at a distance of 50 cm. In our model, we only assign the superconducting physics to these strips and neglect the other layers of the coated conductors. The thickness of each strip is set to 1 μm to accurately represent only the HTS layer in the modeling process. This choice does entail some sacrifice in accuracy, as the buffer and other metal layers are ignored. Despite this, the model provides a rough estimate of the fundamentals and helps us understand the basic principles of HTS flux pumping.

In our model, we use a transformer to apply the field and induce current in the s_1 and s_2 strips. The transformer consists of a pair of copper windings and an iron core. The simulation area is confined within a 2×2 m square, with the rest of the space representing free space. We use a mapped mesh in the active part of the model, with 30 elements along the width and 1 element along the thickness of the strips. For the copper windings and iron core of the transformer, we use 70 elements across the width and 10 elements across the thickness of the copper windings and 40 elements across the thickness of the iron core. In the remaining area, we use a free tetrahedral mesh.



(a)



(b)

Figure 4.3: 2D infinitely long model simulating flux pumping effect in COMSOL. The figure illustrates the three HTS strips, labeled as s_1 , s_2 , and s_3 . The transformer is used to generate magnetic fields and induce the current into s_1 and s_2 , referred to as the charging coil. It should be noted that in the actual system, strip s_3 is positioned far away from the other two strips. However, for the purpose of clarity and ease of visualization, the strips are shown in close proximity in the model.

In our model of the HTS flux pump, we accurately capture the electrical behavior by assigning the appropriate resistivity values to the copper and iron cores. The resistivity of

the stripes is described using the E - J power law, while s_2 also includes a constant resistivity to model the soldering joint between the strips. These modeling choices allow us to study the performance and efficiency of the flux pump under different operating conditions and design configurations. To ensure that the strips form a closed circuit, we apply the appropriate boundary condition.

$$i_c + i_b + i_L = \int_{s_1} \mathbf{J} ds + \int_{s_2} \mathbf{J} ds + \int_{s_3} \mathbf{J} ds \quad (4.10)$$

The simulation results of the current waveform in the superconducting tape s_3 , also known

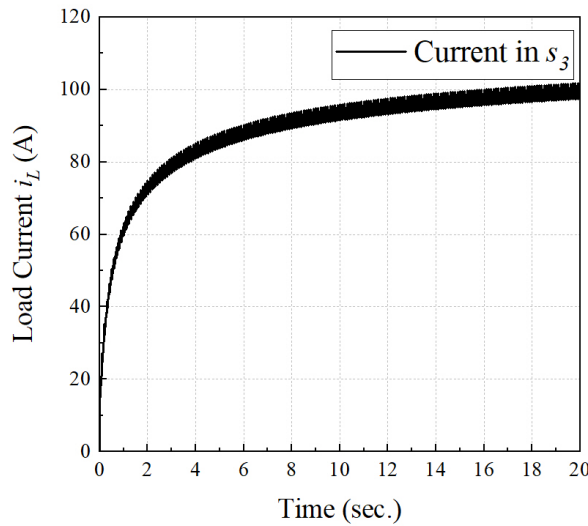


Figure 4.4: Simulation results illustrating the charging curve of strip s_3 . The graph displays the variation of the current in strip s_3 over time as it is being charged by the fluxpump. The charging curve provides insight into the dynamics of the flux pumping effect in the system.

as the load current, are depicted in Figure 4.4. The graph demonstrates an increase in the load current in a stepwise pattern, which is in agreement with the findings from experimental studies later reported in detail. This correlation validates the effectiveness of the modeling strategy employed in the simulation.

Figure 4.4 shows that the load current increases rapidly in the beginning, but with the load current pumping up, the charging speed slows down. This is because, with the increase of

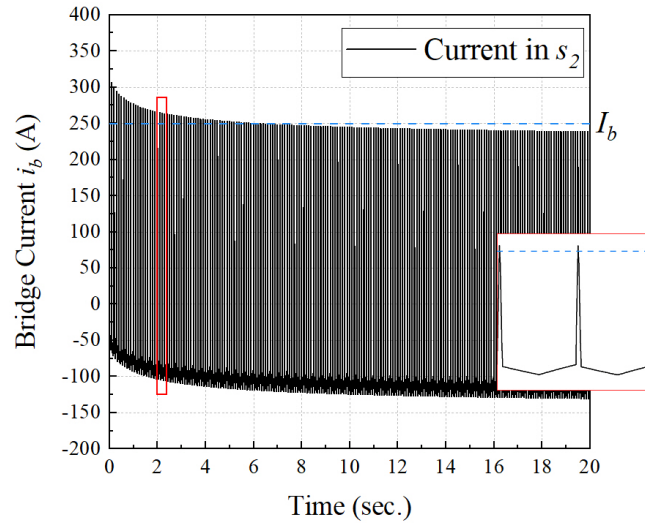


Figure 4.5: Simulation results illustrating the bridge current s_2 .

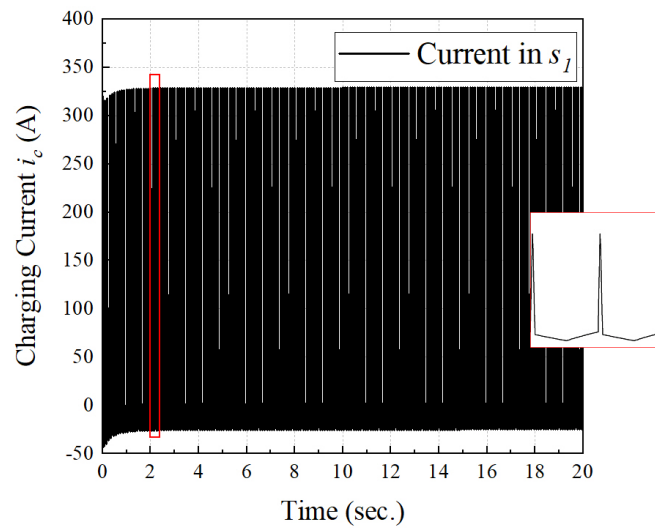


Figure 4.6: Simulation results illustrating the current in the charging coil s_1 .

load current, the bridge current will gradually bias to the negative direction. Consequently, the resistance of the HTS bridge decreases, giving rise to a smaller increment of current in

each cycle in the charging process

$$R_b(i_b) = l V_c \left(\frac{i_b}{i_c} \right)^{n-1} \quad (4.11)$$

Where R_b represents the bridge resistance (switch-on resistance), l is the length of the bridge, V_c is the voltage criteria, and n is the power law exponent. In this study, the critical current load (s_3) is 150 A, the critical current of the bridge (i_b) is 250 A, and the critical current of the charging coil (i_c) is 500 A. The final saturation load current is 100 A, which can be explained by the current in the bridge (s_2) as illustrated in Figure 4.5. During the charging process, the bridge current is biased in the negative direction. Once the load current reaches 100 A, the peak of the bridge current reaches the I_c value. This undesired current biasing results in the saturation of the load current. Similarly, the charging current plot is illustrated in the Figure 4.6.

4.3 A compact flux pump for HTS magnets

4.3.1 Geometrical description of compact flux pump

In this study, we developed an experimental test bench that consisted of a transformer as a flux source, a bifilar coil serving as a bridge (source of DC voltage), unlike [117] where straight parallel tapes were used. The transformer had a 300:1 ratio, with copper on the primary side and HTS tape on the secondary side, and had a critical current of 600 A. The transformer was constructed using amorphous cut cores (AMCC-25) from Hitachi Metals, which have low core losses and high saturation flux density ($B_s=1.56$ T).

To create the magnet, we wound a 6.8 meter long HTS coated conductor into a double pancake coil. The magnet had an inductance of 32 μ H and a critical current of 152 A at 77 K with the criterion $E_0 = 10^{-4}$ V·m⁻¹. The terminals of the magnet coil were connected to either end of the charging coil, and a 45 cm long HTS tape was wound into a bifilar pancake to form a bifilar bridge and was connected in parallel to the magnet. The magnet coil and bifilar

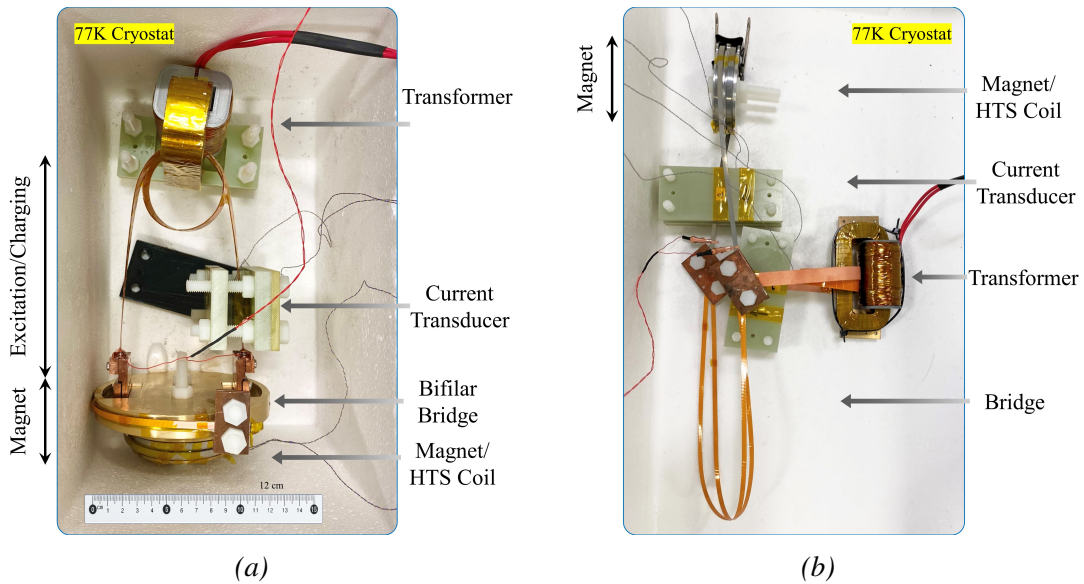


Figure 4.7: Comparison between non-inductive bifilar bridge and inductive conventional bridge incorporated in an HTS flux pump. (a) Photograph of the proposed flux pump showing a double pancake magnet made of 4 mm HTS tape with a diameter of 75 mm, and a bifilar bridge wound around the magnet with a diameter of 120 mm. A transformer is used to induce an asymmetric current into the excitation circuit, which is short-circuited to the bridge through copper terminals (magnet terminals). (b) Conventional self-switching flux pump.

bridge had a total diameter of 12 cm and height of 4 cm, resulting in a compact geometry. We compared this test bench to the flux pump configuration reported by Geng et al. [116], which used the same excitation coil and magnet coil but with a 30 cm straight HTS tape serving as the bridge instead of a bifilar coil bridge.

4.3.2 Non-Inductive Winding Structure

To compare some non-inductive coil structures, divide them into three groups, as shown in Figure 4.8.

Series solenoid

The series solenoid is a winding configuration in which the strands of wire are wound in parallel, and the current flows in opposite directions in each wire. This configuration can be achieved by cutting an HTS tape, as shown in Figure 4.8a. However, the series solenoid has

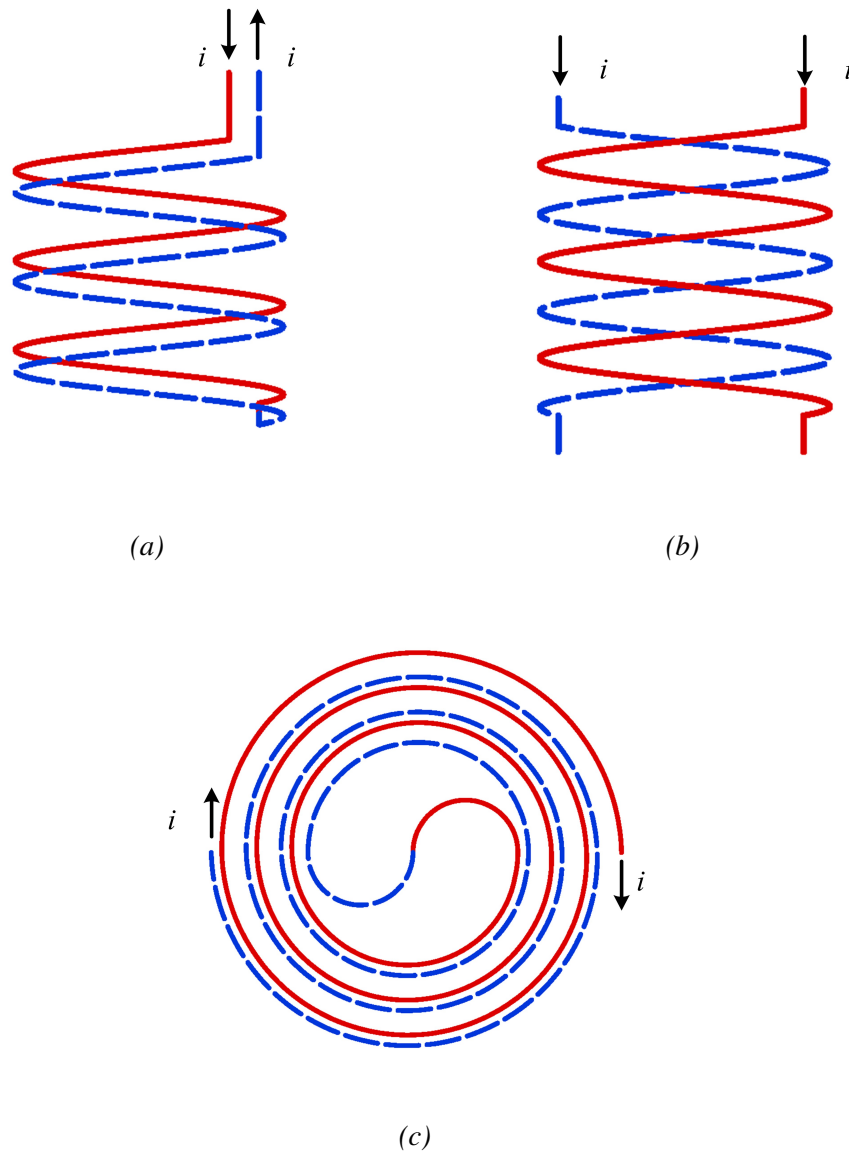


Figure 4.8: Illustration of non-inductive coil structures; (a) series solenoid, (b) parallel solenoid, and (c) bifilar pancake.

some limitations, including a bulky size, relatively large impedance, and ac losses. Despite these drawbacks, the series solenoid has been used in the Curl 10 project to create a fault current limiter (FCL) using BSCCO-2223 bulk superconductors [147].

Parallel solenoid

The parallel solenoid is a winding configuration in which the strands of wire are wound in parallel, and the current flows in the same direction in each wire. This configuration can be made by placing two adjacent coils side by side, as shown in Figure 4.8b. It has several advantages over the series solenoid, including a more compact size, lower impedance, and reduced AC losses. In comparison to the series solenoid, the parallel solenoid is more suitable for use in high field magnet systems such as magnetic resonance imaging (MRI) [17] and nuclear magnetic resonance (NMR) [18].

Bifilar pancake

A bifilar pancake [148] is a simple winding configuration with several attractive features, including a compact size, small impedance, and low AC losses. However, in this structure, the IN and OUT are only insulated with tape or paper, which poses a high risk of electrical breakdown for high voltage applications. Flux pumping requires a relatively low voltage to eliminate the risk of electrical breakdown. For example, to charge a load coil with 60 kA in 24 hours, a DC voltage of 55 mV is required, and only 6 mV is needed to maintain a steady current of 60 kA over the long term [149].

4.3.3 HTS magnet

In this study, we fabricated an HTS magnet (schematic diagram is presented in Figure 4.9), using 4 mm wide HTS tape coated with stainless steel. The total length of the conductor used was 6.8 meters, which was wound onto a brass round coil former with a diameter of 70 mm in a double pancake configuration. This configuration was chosen to decrease the number of splicing contacts between conductor pieces, which can be a major source of resistance in HTS magnets. The resulting magnet coil had an inductance of 32 μH and a critical current of 152 A at 77 K, as determined using the criterion $E_0 = 10^{-4} \text{ V}\cdot\text{m}^{-1}$. Figure 4.10 shows the magnetic field measured at the center of the magnet, along with the corresponding data. The double pancake configuration allows for a more stable magnetic field and higher critical

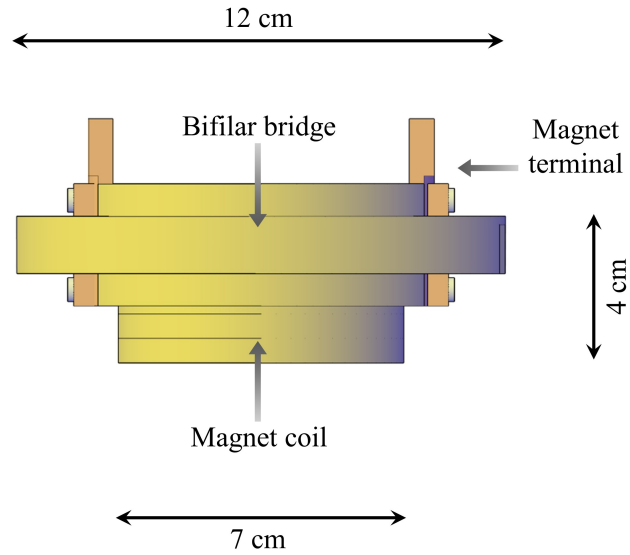


Figure 4.9: HTS magnet incorporating bridge.

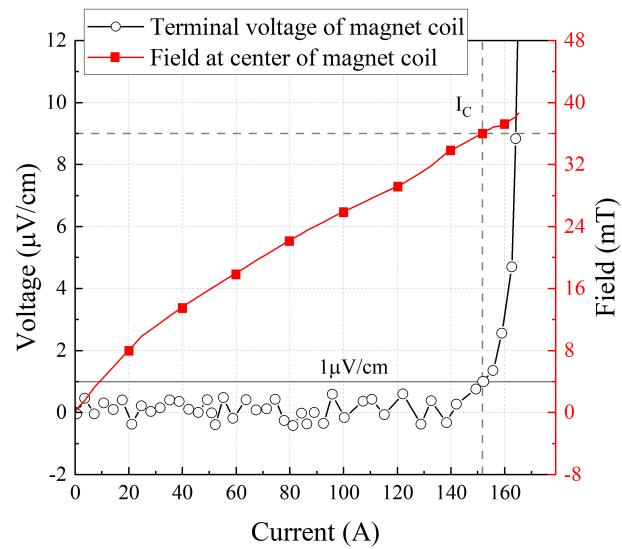
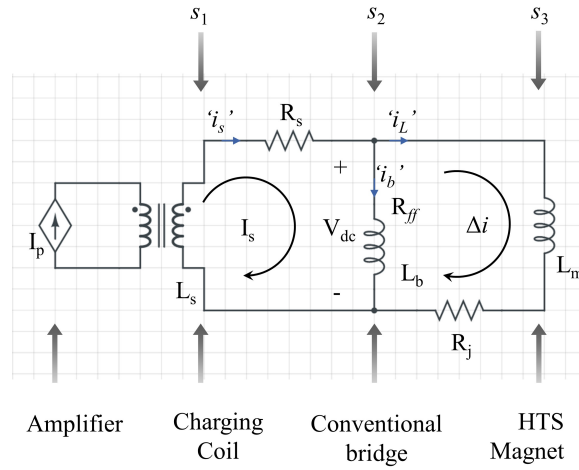
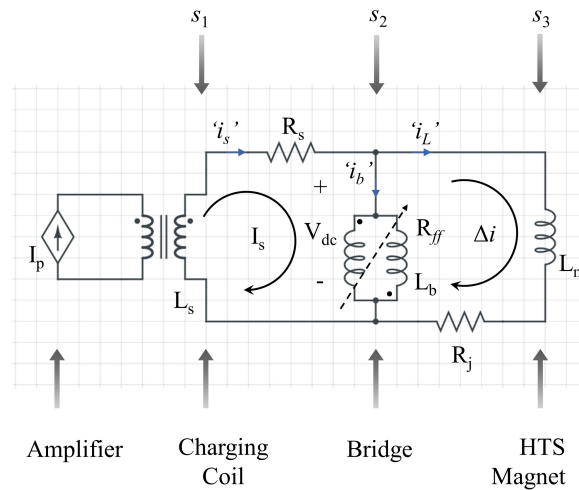


Figure 4.10: Measured $V-I$ curve for an HTS magnet (double-pancake coil) in this experiment and its equivalent magnetic field measured at the center of the coil.

current, making it an ideal choice for high-performance HTS magnets.



(a)



(b)

Figure 4.11: Equivalent circuit model, (a) circuit diagram of flux pump with conventional bridge with flux flow resistivity R_{ff} and bridge inductance L_b [117], (b) circuit diagram of a flux pump with proposed bifilar bridge configuration where bridge inductance is cancelled out $L \simeq 0$.

4.3.4 Equivalent circuit model

The equivalent circuit of the self-switching flux pump is presented in Figure 4.11a, similar to one presented by Geng et al. in [116]. In the equivalent circuit model, R_s represents the

copper terminal resistance between the secondary winding (charging coil) and HTS magnet which is $5E^{-5} \Omega$, R_j is the soldering joint in the magnet which is $1E^{-5} \Omega$ and R_{ff} denotes the flux flow resistance of the bridge superconductor, and L_m is the inductance of the HTS magnet. Geng et al. noted that the bridge inductance was too small to be significant and thus ignored it in their model. However, in our proposed bifilar bridge-based flux pump, we present the equivalent circuit in Figure 4.11b, where the bridge is represented by two anti-wind coils (bifilar coils) with a total inductance of $L_b = 0$. By winding the bridge as a bifilar coil, we effectively force the bridge inductance to be zero. Despite this circuit similarity to the LTS flux pump described in [131], the self-switching flux pump differs in terms of its underlying physics and control strategy. The origin of R_{ff} in our study is due to the flux flow [78] of the HTS superconductor, while in [131], it is a result of driving the LTS superconductor into the normal state.

4.4 Experiment

4.4.1 Experiment test bench

Cryostat

A liquid nitrogen bath cryostat is a device used to achieve and maintain low temperatures, typically around 77 K (-196 °C). It consists of an outer wooden chamber and an inner chamber that holds liquid nitrogen, which is used to cool the sample being studied. The temperature of the sample can be controlled by adjusting the amount of liquid nitrogen in the inner chamber and by adding or removing heat from the outer chamber. This type of cryostat is commonly used in research and experimentation where low temperatures are necessary. The cryostat used in this study is 50 cm long, 40 cm wide and 30 cm deep.

Power supplies

1. KEPCO bipolar power amplifier:

In the experiment, we used a KEPCO BOP 2010 power supply to power the transformer,

which was used to induce current in the HTS charging coil. The power supply acted as an amplifier, able to amplify external input signals and provide outputs of up to 10 A and 20 V. During the experiment, the power supply was operated in current mode, meaning that the output current was an amplification of the external input signal. To protect against overvoltage during high-frequency operation, we connected two 20 V anti-series Zener diodes in parallel with the output terminals of the power supply, due to the inductive nature of the load.

2. Keithly:

Keithley 2230 multichannel power supply as a current source for the sensors. This versatile power supply is capable of delivering up to 20 mA of current to the Hall effect sensors, making it an ideal choice for our experimental setup. Additionally, we used the Keithley 2230 to provide a stable 10 V output to the C Series Current Output Module NI-9265. This allowed us to precisely control the input current to the sensors and ensure accurate and repeatable measurements.

Current transducers

In order to accurately measure the induced current in the charging coil and the current pumped into the HTS magnet, we have designed and constructed two custom cryogenic current transducers. These transducers operate on the principle of a current transformer, but without any windings. Each transducer consists of a pair of C-shaped cores and a Hall effect sensor (Lakeshore HGT-2010). The Hall sensor is positioned within one of the cores, and the cores are placed face to face. When a conductor carrying a current is passed through the cores, a magnetic field is generated within the cores. The Hall sensor detects this field and provides a corresponding reading. To calibrate the current transducers, we inserted a copper bar into each transducer and applied a current ranging from 0 to 1000 A in 10 A increments. For each increment, we recorded the output of the Hall sensor. We then used curve fitting to determine the relationship between the applied current and the sensor output for both transducers.

Curve fitting expression for *Sensor 1*:

$$y(x) = \begin{cases} 15305 \cdot x + 0.2, & \text{if } 0 \leq x \leq 200; & (4.12) \\ 15098 \cdot x + 0.5, & \text{if } 201 \leq x \leq 400; & (4.13) \\ 1e^7 \cdot x^3 - 531908 \cdot x^2 + 18066 \cdot x + 10, & \text{if } 401 \leq x \leq 1000; & (4.14) \end{cases}$$

$$R^2 = 0.9971$$

Curve fitting expression for *Sensor 2*:

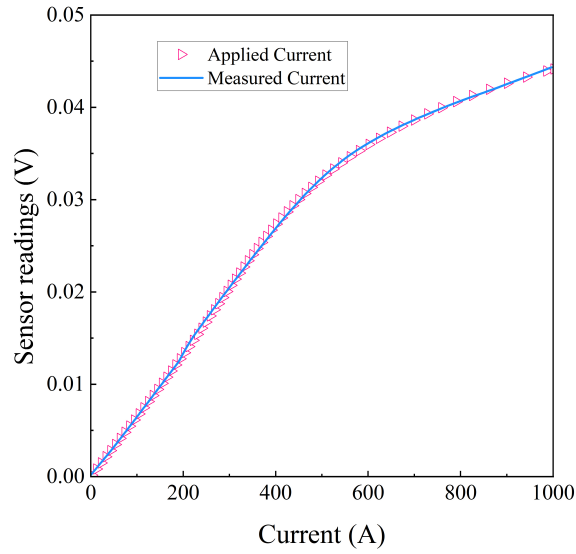
$$y(x) = \begin{cases} 18290 \cdot x + 4.4, & \text{if } 0 \leq x \leq 200; & (4.15) \\ 16191 \cdot x + 15, & \text{if } 201 \leq x \leq 400; & (4.16) \\ 3e^7 \cdot x^3 - 1e^6 \cdot x^2 + 22903 \cdot x + 15, & \text{if } 401 \leq x \leq 1000; & (4.17) \end{cases}$$

$$R^2 = 0.0.9984$$

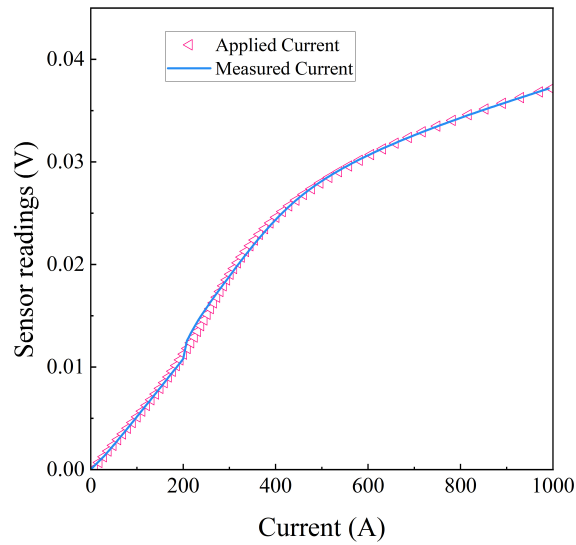
Hall effect sensors

For accurately recording the magnet's field in our study, we used a GHS-C cryogenic extreme range sensor that utilizes the inherently high sensitivity of graphene. The GHS-C range of cryogenic 1D graphene Hall sensors offers excellent resolution at cryogenic extremes, with measurements up to 30 T, while also featuring properties such as a negligible planar Hall effect and overall robustness. The GHS-C sensor has a number of beneficial features, including operation down to 1.5 K, low power dissipation, low noise performance, high linearity, and high resolution.

To measure the magnetic field of the magnet, a GHS-C cryogenic extreme range sensor is installed at the center of the magnet former. The sensor is mounted on a fiberglass PCB and is powered and read using a pair of twisted 26 AWG wire with a cross-sectional area of 0.128 mm². The GHS-C sensor is known for its high sensitivity and ability to operate at low



(a)



(b)

Figure 4.12: Calibration curves for the Hall effect sensors in the current transducers. (a) Calibration curve for current transducer 1. (b) Calibration curve for current transducer 2.

temperatures, making it an ideal choice for measuring the magnetic field of the magnet.

$$voltage\ output(V) = magnetic\ field(T) \times sensitivity \times input\ current(A) \quad (4.18)$$

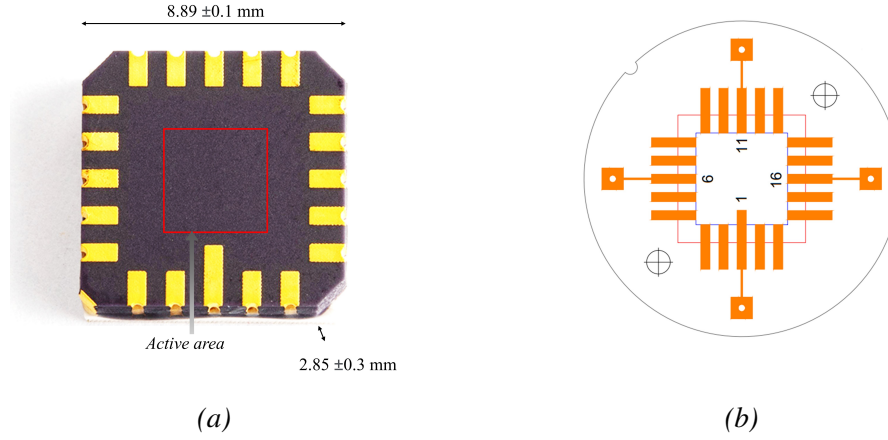


Figure 4.13: GHS-C Cryogenic 1D Hall Sensor (a) Photograph and (b) Circuit Diagram of PCB.

$$Sensitivity(Mid - Range) = \begin{cases} 250, & \text{minimum;} & (4.19) \\ 290, & \text{typical;} & (4.20) \\ 400, & \text{maximum;} & (4.21) \end{cases}$$

$$Sensitivity(Extreme - Range) = \begin{cases} 150, & \text{minimum;} & (4.22) \\ 200, & \text{typical;} & (4.23) \\ 250, & \text{maximum;} & (4.24) \end{cases}$$

Voltage taps

We used a twisted wire of 26 AWG for voltage taps. The wire was equipped with crocodile terminals at one end, allowing for easy connection to other components. The use of a twisted wire was chosen for its ability to reduce electromagnetic interference and improve the signal quality of the voltage measurements. The small size of the wire, 26 AWG, made it ideal for use in a compact experimental setup. Overall, the utilization of twisted wires with crocodile terminals significantly enhanced the accuracy and reliability of voltage measurements in the experiment. Twisted wires eliminated parasitic voltage induction, and crocodile terminals maintained consistent readings, unlike varying solder joint thickness.

Implementation of data acquisition system using LabVIEW

1. Signal Generation:

In order to achieve the desired charging current in our experiment, it was necessary to provide a precise input current to the primary of the transformer. To do this, we developed a program using LabVIEW software that generated control signals for the transformer. This program allowed us to set the magnitude, frequency, and number of cycles for both positive and negative peaks of the input signal. The digital signal generated by the program was then converted to an analogue signal using the National Instruments analogue voltage output module (NI-9263), which was fed into an amplifier (KEPCO BOP 2010) for further amplification. The use of this system ensured that we were able to accurately control the charging current and achieve efficient flux pumping.

2. Data Acquisition:

To accurately capture the various signals from the experimental test bench, we utilized a set of National Instrument DAQ cards (NI-9238). During each iteration, an array of 100 samples was received by the computer at a rate of 1 kHz. The data acquisition capabilities of the NI-9238 are as follows:

Device NI-9238

Voltage range = ± 500 mV,

Resolution = 24 bit,

$$\begin{aligned} \text{smallest detectable signal} &= \frac{\text{voltage range}}{2^{\text{resolution}}} \\ &= 5.96e^{-8} \text{ V} \end{aligned}$$

The resolution of $5.96e^{-8}$ V is notably enough for the experimental requirements.

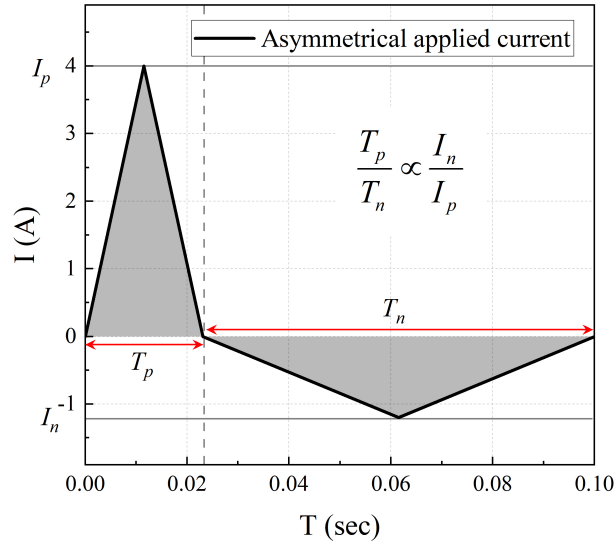


Figure 4.14: Asymmetric applied current waveform.

4.4.2 Applied current

An asymmetric signal is applied as the primary (input) current signal in this study, presented in Figure 4.14. During the positive cycle, the current ramps to the positive peak (I_p) at a constant rate, and then damps down to zero at the same rate. Similarly, during the negative cycle, the current decreases to a negative peak (I_n), then ramps up at the same rate to zero. The positive peak is kept higher to drive the superconductor into the flux flow region, enabling flux flow from the secondary side to the load side (magnet). However, the negative peak is kept at much lower values to retain the flux within the load. To make the dc component zero, the length of the positive period over the negative period is kept inversely proportional to the peak values.

$$\frac{T_p}{T_n} \propto \frac{I_n}{I_p}, \quad (4.25)$$

$$\int_0^T i_p(t) dt = 0, \quad (4.26)$$

Where, T_p is duration of positive peak, T_n is duration of negative peak, I_p is amplitude of positive peak, I_n is amplitude of negative peak, i_n is the primary current, and T , is time period.

In both case primary current of amplitude 4 A is applied to the primary of transformer.

4.4.3 Current induced in the charging coil

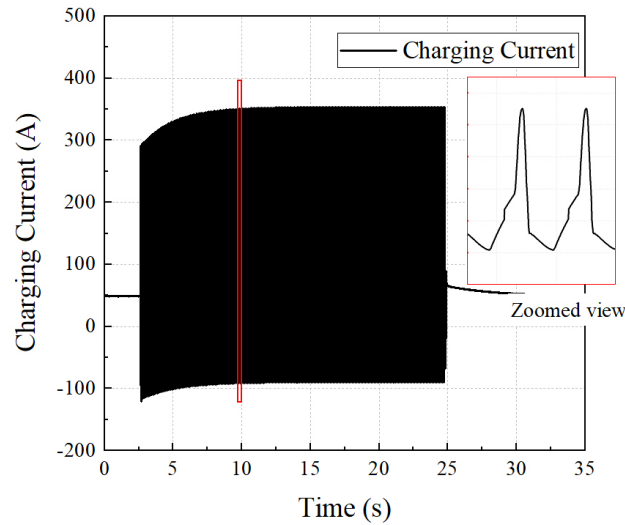


Figure 4.15: Induced current (i_s) in the charging coil of a self switching flux pump with a conventional bridge.

The current induced in the excitation circuit can be calculated using the equation presented below, which takes into account the circuit explanation provided in Section 4.3.4.

$$0 = \frac{d\phi}{dt} + L_s \frac{di_s}{dt} + i_s R_s + i_s Z_b, \quad (4.27)$$

Where, ϕ is flux generated by primary copper of the transformer coupling with HTS excitation (secondary) coil, L_s is self inductance of excitation coil. i_s is excitation current, R_s is joint resistance and Z_b is bridge impedance. In both cases, the only difference is in the magnitude of Z_b . For a conventional bridge, the impedance will be higher, limiting the induced current as shown in Figure 4.15. In a transformer action, if the load impedance is high, the output voltage may reach its limit so that the secondary current cannot follow the primary current [116]. However, in the case of a bifilar coil, the inductance is zero and the impedance is

determined solely by the real component, which is much lower than that of a conventional bridge. As a result, a higher current is induced in the secondary coil, as shown in Figure 4.16.

4.4.4 Exploring the Current-Voltage characteristics of a bridge in flux pump

For an ideal transformer action, the (secondary) charging current i_s is always proportional to its primary current i_p . However, for a real transformer, if the load impedance Z_b is high, the output voltage may reach its limit so that the secondary current cannot follow the primary current. A voltage limit for a transformer with HTS as a secondary can be stated as the voltage appears in a state when current above its critical current value flows through the HTS tape before quenching. In this section we will discuss the influence of the magnitude of applied current on the load current, since the bridge resistance originally depends on the primary current. If the peak value of the input current is kept relatively low to make bridge voltage reach the limit then the secondary current is proportional to the primary current with the transformer ratio. The bridge current i_b plot is illustrated in Figure 4.17 for conventional

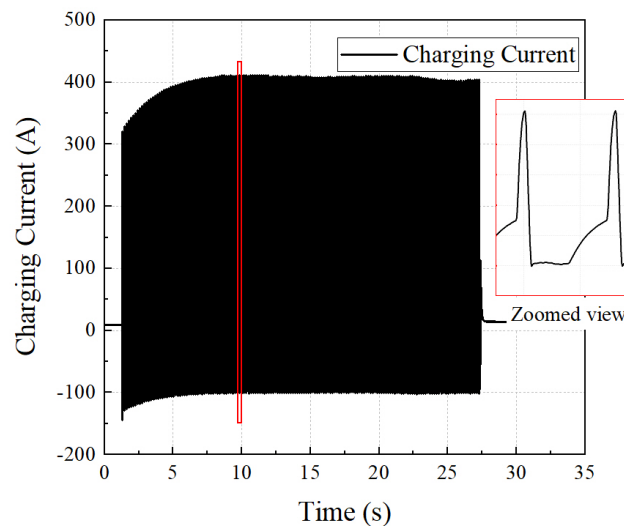


Figure 4.16: Induced current (i_s) in the charging coil of a self switching flux pump with a bifilar bridge.

bridge in flux pump whereas Figure 4.18 illustrates bridge current for bifilar bridge in flux pump. During the first cycle, the charging current will equal the bridge current because the load current (Δi) is zero. With the accumulation of load current, the bridge current will gradually be biased in the opposite direction. In this case, the dc voltage drops with the increase in the load current and it can be seen in Figure 4.19. Therefore the load current presents a curve similar to the charging curve of the first order circuit. When the applied current is too low to drive the bridge to the flux flow region, the load tends to saturate at a lower value. Keeping in mind the circuit diagram presented in Section 4.3.4, a mathematical representation can be written as following

$$i_s = i_b + \Delta i, \quad (4.28)$$

$$V_{dc} = i_b R_{ff} + L_b \frac{di_b}{dt} = L_m \frac{d\Delta i}{dt}, \quad (4.29)$$

where V_{dc} , is the dc voltage across the bridge, in (4.29) for a bifilar bridge the L_b is zero so the dc voltage V_{dc} across the bridge is purely due to flux flow resistivity R_{ff} .

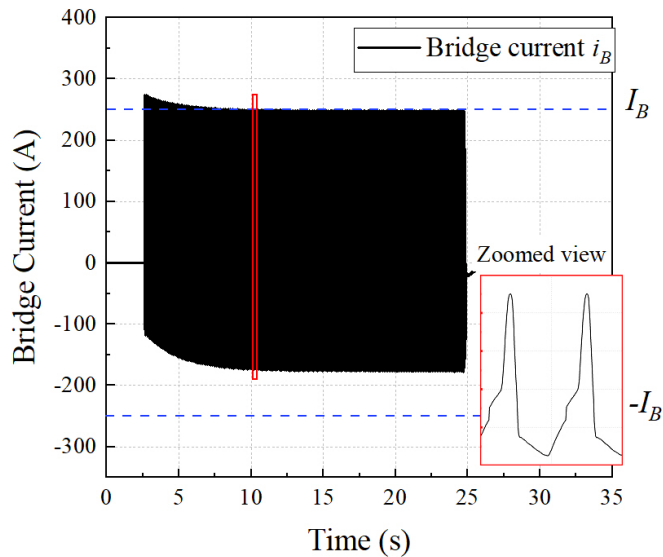


Figure 4.17: Bridge current (i_b), plot of current flowing through a conventional flux pump bridge.

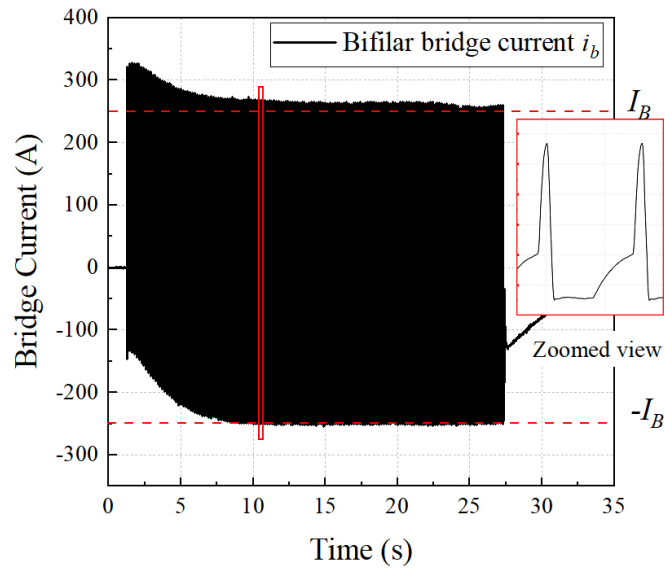


Figure 4.18: Bridge current (i_b), plot of current flowing through a bifilar flux pump bridge.

In contrast, when the primary current is too high, the bridge voltage reaches its maximum value and remains constant during the entire charging process. As a result, the load current increases at a nearly constant rate in the beginning and then decreases as it approaches its

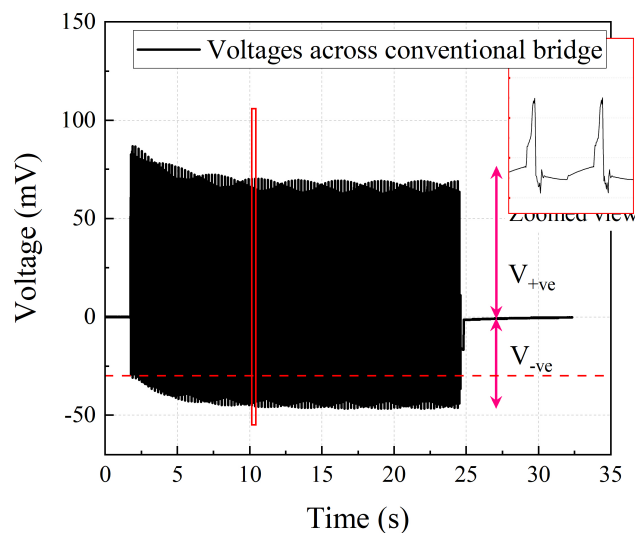


Figure 4.19: The voltage measured (v_b) across the conventional bridge in the flux pump shows an amplitude of under 100 mV, along with a noticeable DC biasing trend over time.

critical current value. On the other hand, a bifilar bridge can induce a higher excitation current at a lower applied current because it offers minimal impedance. This allows the bifilar bridge to reach its voltage limit at a lower applied current. The DC voltage across the bifilar bridge is solely determined by the flux flow resistance. When the input current is applied, the DC voltage remains constant throughout the charging process, allowing the flux pump to charge the magnet coil to its critical current value. The measured bifilar bridge voltage plot is shown in Figure 4.20.

4.4.5 Flux injection into the HTS magnet

The magnetic field plot of the coil magnet is illustrated in Figure 4.21, for both bridge configurations. A bifilar bridge can give a higher dc voltage to charge the magnet to its maximum capacity with minimal geometry. Whereas with the conventional bridge arrangement higher primary current is required to reach the voltage limit at the bridge to charge the coil to its critical current value. In section 4.3.3 it is already demonstrated that the critical current of the HTS magnet is 152 A and at this value, it produces a magnetic field of 35 mT at its centre.

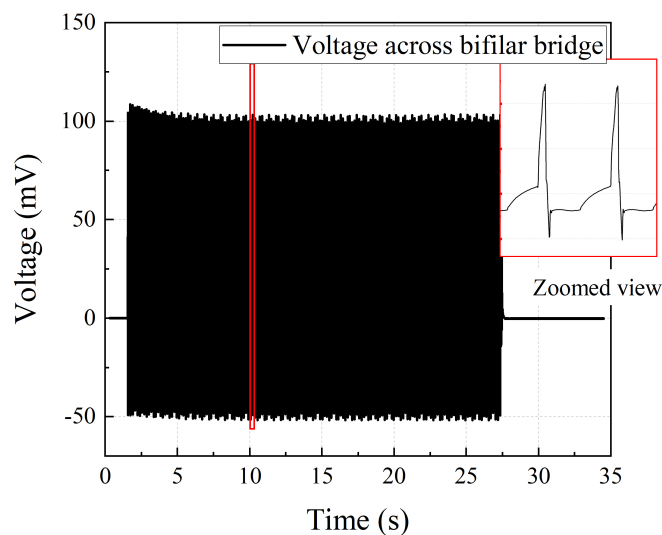


Figure 4.20: The voltage measured (v_b) across the bifilar bridge in the flux pump shows an amplitude of over 100 mV, and the peak voltage remains stable over time.

The mathematical relation between the bridge voltage V_{dc} and the load current can be given as

$$\Delta i = \frac{1}{L_m} \int V_{dc} dt, \quad (4.30)$$

The use of a bifilar bridge results in higher DC voltages, as demonstrated in Figure 4.22. This figure also shows the difference in voltages and the corresponding change in the magnet coil's field for both the bifilar bridge and conventional bridge flux pump when the same applied current and magnet coil are used. When the peak value of the applied current is low enough to cause the bridge voltage to reach its limit, the bridge current becomes biased in the opposite direction and the DC voltages on the bridge increase as the load current increases. This creates both positive and negative components during a cycle, causing the rate of change of current to decrease with each cycle and the magnet to saturate before reaching its critical current. The negative component in the DC voltage can be seen in the magnetic field plot in Figure 4.22, causing a delay in the load current and resulting in saturation at a lower value.

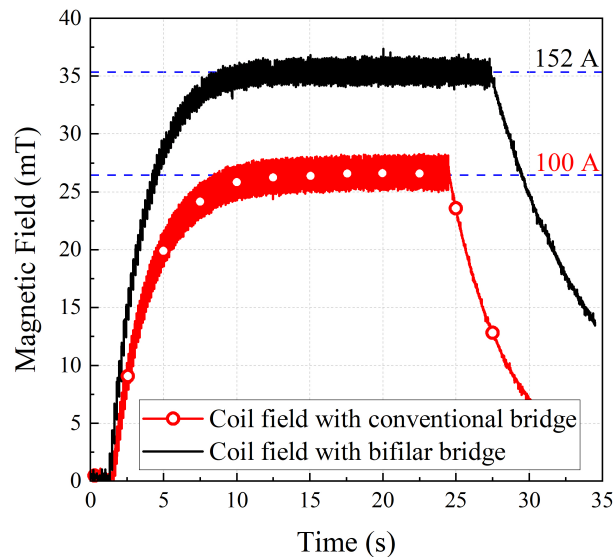


Figure 4.21: The load's magnetic field measured at the center of the coil magnet for both cases, with conventional bridge saturating at 26 mT and bifilar bridge at 35 mT.

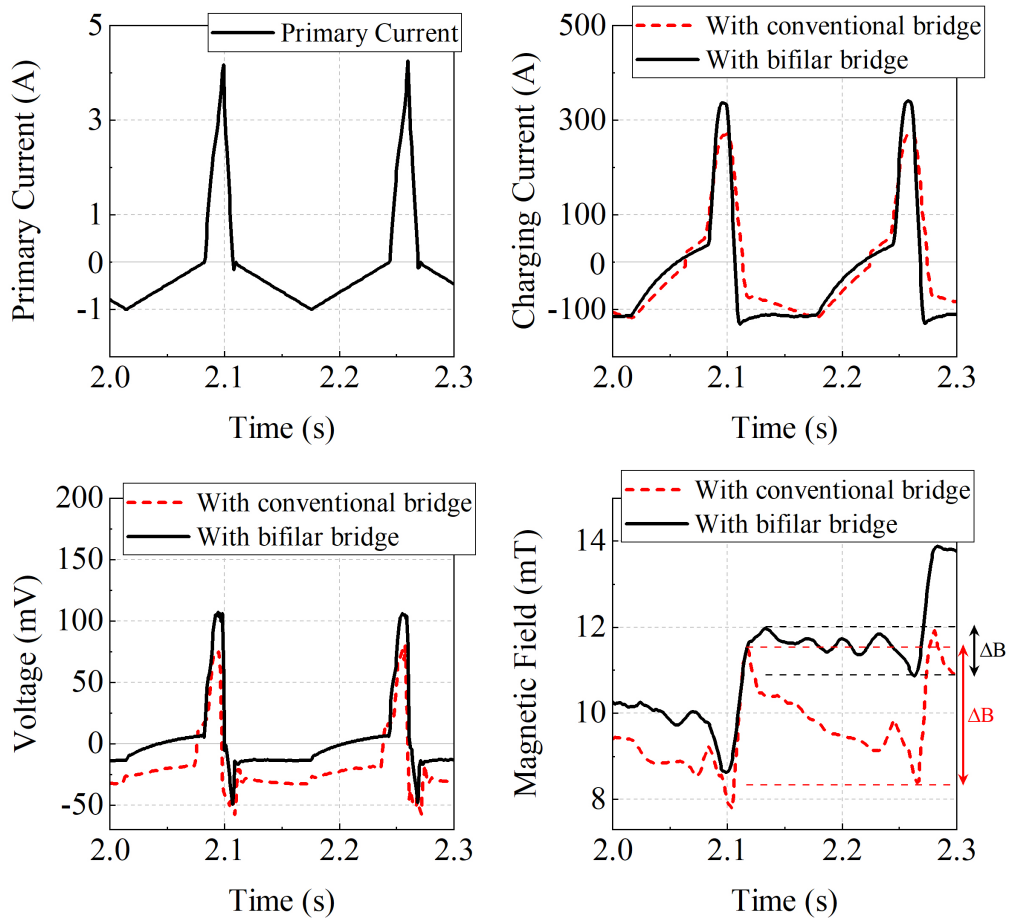


Figure 4.22: Measured primary current, measured charging current for conventional and bifilar bridge, measured induced voltages across conventional and bifilar bridge and measured magnetic field in a magnet coil for conventional and bifilar bridge.

4.5 Estimation of losses in flux pump

4.5.1 Losses in copper

In copper, electrical losses can be classified into two types: joule heat and heat flux. Consider a high-temperature superconducting (HTS) magnet in driven mode with two copper leads, each 0.2 m in length and with a diameter of 20 mm, supplying 100 A of current at 77 K. The heat load can be calculated using studies by Blondelle et al. [150] and Le et al. [151] that provide insights into current leads operating at cryogenic temperatures. The heat losses in the

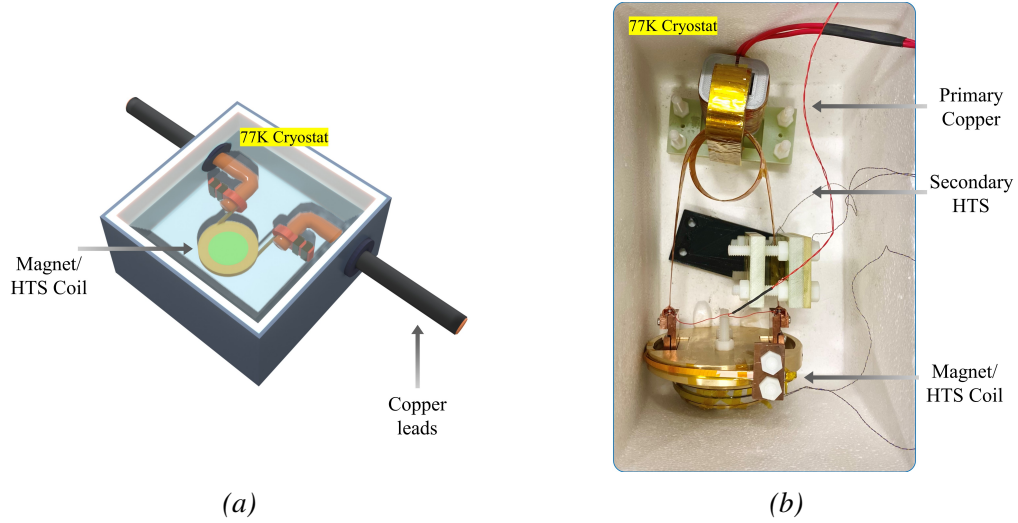


Figure 4.23: High-temperature superconducting (HTS) magnet, (a) operated in driven mode and (b) using flux pump at 77 K.

Target current in the coil	100 A
Applied current (i)	100 A
Copper lead length $\times 2$	0.4 m
Copper lead diameter ϕ	20 mm
Joule heating	0.0022 W
Heat flux/Power	5.9 W
Total heat loss	5.90200 W

Table 4.1: Instantaneous heat losses in copper leads (Temperature gradient 300 K-80 K).

Target current in the coil	100 A
Applied current (i)	4 A
Copper wire length 300turns	30 m
Copper wire diameter ϕ	1.5 mm
Joule heating	0.00035 W
Heat flux/Power	0.236 W
Total heat loss	0.23635 W

Table 4.2: Instantaneous heat loss in primary copper of a flux pump (Temperature gradient 300 K-80 K).

primary of the flux pump, made of copper, can be compared to those of the copper leads. The copper wire in the primary side of the flux pump is 30 m long, with a diameter of 1.5 mm, and 250 turns. The results are presented in Tables 4.1 and 4.2. The study shows that the heat losses from the thick copper leads are 400% higher than those from the primary side of the flux pump. However, heat losses can be reduced to zero as the flux pump induces current inductively, which allows the replacement of the C-shaped transformer with an air-core transformer.

Additionally, it's worth considering the instantaneous joule heating at peak amplitude and a fair comparison of heat loss during one cycle of applied current, as illustrated in Figure 4.24.

Integrating over one time period, the total power dissipation for copper leads delivering 100 A is 2.23 W, whereas that of the primary of the transformer is 0.02 W.

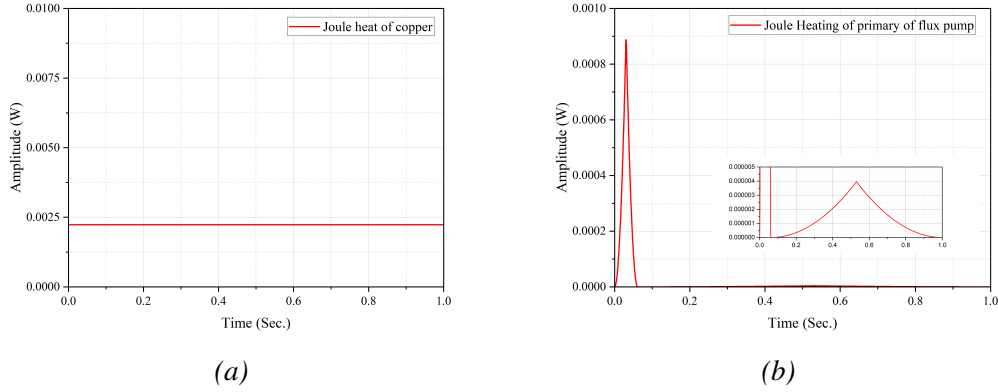


Figure 4.24: Joule heat of copper lead in (a) HTS magnet operating in driven mode at 77 K and (b) HTS magnet operated using a flux pump at 77 K.

4.5.2 Efficiency

The efficiency η refers to the proportion of power output provided to the load, relative to the overall power dissipated in the electrical circuit.

$$\eta = \frac{P_{out}}{P_{out} + P_{in} + P_{ac}} \quad (4.31)$$

In the context of a self-rectifying flux pump, the load current is maintained during charging cycles by the parallel ‘bridge’ switch in its closed state as explained in Section 3.2.3. In order to prevent saturation of the transformer [152], it is necessary to conserve flux across the switches within each cycle, thereby avoiding the accumulation of trapped flux in the charging loop [117]. Flux motion across the switching element results in a circuit voltage, allowing this requirement to be stated using the cycle-averaged integral of voltage across the series and parallel switches as [149]

$$\frac{1}{T} \int_0^T v_s dt = \frac{1}{T} \int_0^T v_b dt \quad (4.32)$$

Where $f = 1/T$ is the frequency of applied current, v_s and v_b are the voltage across the joint (R_s) and bridge voltage. The power delivered to the load is denoted by P_{out} , while the power

dissipated in the bridge components and the charging coil is represented by P_{in} , and the AC losses in the charging coil are represented by P_{ac} . The AC losses in the charging coil can be neglected as the magnitude of the losses per cycle is on the order of 10^{-9} . As a half-wave rectifier, these power values can be expressed as

$$P_{out} = \frac{1}{T} \int^T v_b \cdot i_L dt \quad (4.33)$$

$$P_{in} = \frac{1}{T} \int^T (v_s \cdot i_s + v_b \cdot i_b) dt \quad (4.34)$$

Where the current in the charging coil, bridge and the load (magnet) are denoted by i_s , i_b and i_L , respectively. By substituting the aforementioned equation into the efficiency equation given by 4.31, we obtain the following expression

$$\eta = \frac{\int^T v_b \cdot i_L dt}{\int^T v_b \cdot i_L dt + \int^T (v_s \cdot i_s + v_b \cdot i_b) dt} \quad (4.35)$$

The equation presented above is useful for determining the optimal efficiency of each cycle. Rectification occurs when the average value of the bridge voltage over the course of the cycle is non-zero, producing a net dc voltage across the load. When injecting small amounts of current during each cycle, such as during load saturation with low current ripple, the variable di_L can be considered negligible in comparison to the constant i_L and thus removed from the integral.

$$\eta = \frac{i_L \int^T v_b dt}{i_L \int^T v_b dt + \int^T (v_s \cdot i_s + v_b \cdot i_b) dt} \quad (4.36)$$

Equation 4.32 equates cycle averaged switching voltage, giving

$$\eta = \frac{i_L \int^T v_b dt}{i_L \int^T v_b dt + \int^T v_b (i_s + i_b) dt} \quad (4.37)$$

A voltage is generated when the current in a system is equal to or greater than the critical

current value I_c . Bean's critical state model [66] can be employed to constrain instantaneous currents to their corresponding critical values during switching, resulting in the generation of an arbitrary amount of voltage. Consequently, the efficiency resulting from the equation described above is independent of the voltage waveform [149].

$$\eta = \frac{i_L}{i_L + i_s + i_b} \quad (4.38)$$

The efficiency of both cases is displayed in Figure 4.25. The graph highlights that the flux pump with a bifilar bridge outperforms the conventional flux pump in terms of efficiency, indicating that the bifilar bridge is a more effective approach.

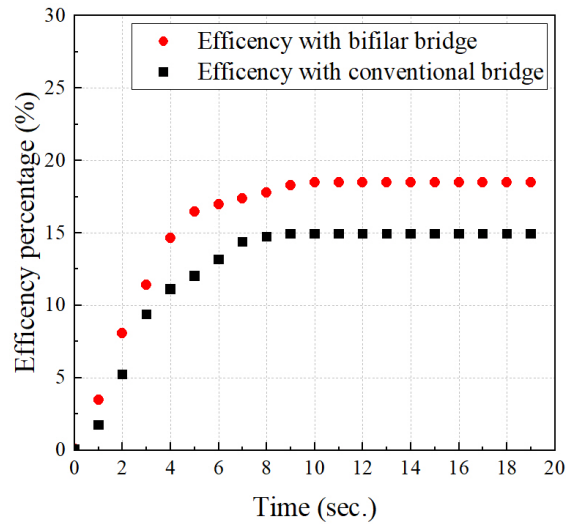


Figure 4.25: The efficiency trend η for flux pumps with bifilar and conventional bridges over charging duration.

4.6 Discussion

Self-switched high temperature superconductor flux pumps have previously been demonstrated to be able to quickly pump up currents in large magnets using a single transformer. However, they may not be ideal in terms of field stability due to the sharp $V-I$ curve of the

bridge superconductor, which makes it difficult to effectively control the bridge voltage. Noise in the bridge current can lead to large errors in the voltage. One solution to this problem has been the use of dynamic resistance control flux pumps, but these require an additional field source perpendicular to the bridge, which increases the heat load on the cryogenic system and the overall footprint of the device.

In contrast, the proposed bifilar bridge flux pump can induce higher voltages due to its increased bridge length without adding inductance to the circuit. This allows for stable, constant voltage flux pumping, enabling persistent current operation in HTS magnets. At a peak voltage of 100 mV and an inductance of 32 μH , the proposed flux pump can charge a magnet to 152 A, with a total series resistance of $6.6\text{E}^{-5} \Omega$ due to both the HTS joint and the copper terminals of the magnet.

The conventional bridge in a self-switched HTS flux pump forms a loop while shorting the terminals of the magnets, adding inductance to the circuit. This can limit the flow of current on the primary side and make it difficult to achieve high charging currents on the secondary side. By using a bifilar bridge, the inductance in the bridge is eliminated, allowing for high induced current in the excitation circuit and a stable voltage across the bridge. The bifilar bridge also gives the freedom to adjust the length of the bridge depending on the voltage requirements of the load magnet. In a cycle with period T , the flux pumping duration (T_p) and flux decay duration (T_n) can be adjusted. In comparison to a conventional bridge, the total impedance in the bifilar bridge configuration is lower due to the absence of inductive components, resulting in a slower decay of the load's magnetic field.

4.7 Conclusion

In this chapter, we presented a compact HTS flux pump consisting of a transformer with a superconducting secondary winding and a double pancake coil magnet that is short-circuited by a non-inductive bifilar coil, referred to as a “bridge.” Our results demonstrate that the bifilar bridge configuration is able to achieve higher and more stable peak voltage (~ 100 mV) throughout the charging process, compared to conventional HTS bridges. Additionally, it is

able to reach a magnetic field of 35 mT, while conventional bridge saturate at 25 mT with the same applied current. The absence of an inductive component in the bifilar bridge allows for the HTS load to be charged effectively to its I_c value, as only flux flow resistivity generates a dc voltage across the bridge. The use of bifilar bridge arrangements reduces the size of the flux pump and simplifies the geometry, making it suitable for fully superconducting HTS machines, particularly in electromotive applications where round magnets are desired. Furthermore, this bridge configuration eliminates the need for additional field sources, reducing the heat load on the cryogenic system and minimizing the footprint of the flux pump. Overall, this novel bifilar bridge design is a significant advancement in the development of efficient and compact HTS flux pumps. This configuration opens the door to achieving high bridge voltages, which could be a game-changer in replacing expensive linear, bulky power supplies for large-scale applications.

5

Feedback-Controlled Field Modulation for HTS Magnets in Persistent Current Mode

5.1 Introduction

High temperature superconducting (HTS) coated conductors (CC) magnets are known for their exceptional capability to generate strong, uniform, and ultra-stable magnetic fields. These advantageous properties result from confining supercurrents to high inductance coils with extremely low operational resistance. Studies have shown almost negligible attenuation in case of LTS, with the magnetic field produced sustained to better than 1 ppbh^{-1} in some cases, and extremely large decay times [153]. These so-called persistent mode-driven electromagnets transform into the world's highest field quasi-permanent magnets. Persistent current operation in an HTS coil becomes possible by including an HTS persistent joint in the circuit. Ohki et al. presented an intermediate grown superconducting (iGS) joint between REBCO coated conductors and achieved a joint resistance of $< 5 \times 10^{-13} \Omega - 3 \times 10^{-12} \Omega$ [154]. In addition, it has been observed that in the iGS joints between REBCO coated conductors, the critical current degrades to 45 % of the coated conductor critical current at 77 K in a self-field with a criteria of $1 \mu\text{V}$. Recently, Yanagisawa et al. in the study used an iGS superconducting joint between coated conductors in their persistent-mode NMR magnet [155]. It achieved

temporal stability of ~ 1 ppm, allowing for high-resolution NMR spectra to be obtained using a dc source and thermal switches (heaters) for charging the coil. In addition to a superconducting joint, Lee et al. presented a wind-and-flip method to achieve a jointless HTS coil and demonstrated persistent current operation with zero field cooling [156].

A key question in the use of HTS coils is how they are energized. As previously discussed, flux pumps are the most effective means for injecting direct current into HTS magnets. HTS flux pumps can charge the magnet and compensate for any current decay, enabling the quasi-persistent operation of HTS-CC magnets. The contact voltage drop of soldering joints is typically much lower than the voltage determined from the E - J relationship and is therefore considered negligible. However, the resistance of soldering joints does not go to zero, so the current flowing through HTS magnets will still decay over time. Ali et al. reported a ring-shaped HTS magnet with a trapped field of 4.6 T after field cooling magnetization at 25 K [157]. This magnet can operate in persistent current mode, but it would be difficult to compensate for the current decay when exposed to an external AC magnetic field without continuous charging using a flux pump. To date, it remains challenging to maintain an HTS magnet in persistent current mode without soldering joints, requiring continuous current injection using a flux pump.

This chapter proposes the use of closed-loop feedback control to establish an ideal charging system for HTS magnets in persistent current operations. Closed-loop feedback control is widely used in many engineering applications, including motor drives [158], the motion of atoms in optical cavities [159], and stabilizing Rabi oscillation in superconducting qubits [160]. In an HTS coated conductor, a resistivity known as flux flow resistivity appears when there is flux motion. This phenomenon occurs when a superconductor is subjected to an AC field, transporting an AC current, or transporting a DC current above its critical current value. In the previous chapter, we introduced a self-switched high temperature superconducting flux pump that drives HTS coated conductors into the flux flow region on the E - J curve by injecting current above the critical current value. In this chapter, a closed-loop feedback control system that builds upon this approach to induce a flux flow voltage and achieve bidirectional current control for an HTS coil in persistent current operation is presented. The feedback control

allows for precise flux modulation through the accurate injection and removal of current in the HTS magnet, enabling precise field control of the magnet.

5.2 Jointless HTS loop charging using flux pump

This section investigates the potential of using a self-switching HTS flux pump to charge an HTS loop as a feasibility study, laying the groundwork for charging a jointless HTS magnet. As depicted in Figure 5.1, the proposed loop has a single turn serving as a load and contributing a small inductance. The other half of the loop functions as a bridge, with the end terminals of the loop connected to the charging coil. In the following sections, we will examine the experimental setup and evaluate the viability of this approach through the results of our preliminary study.

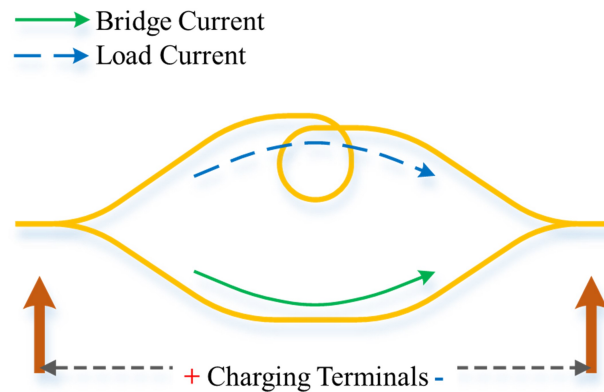


Figure 5.1: Schematic diagram of the HTS loop being charged by the self-switching HTS flux pump. The loop is formed by slitting the HTS tape lengthwise from its center, with one side of the loop serving as a bridge and the other side featuring a single turn acting as a load. Once charging is complete, the loop will function as a persistent current one-turn HTS magnet

5.2.1 Equivalent circuit diagram

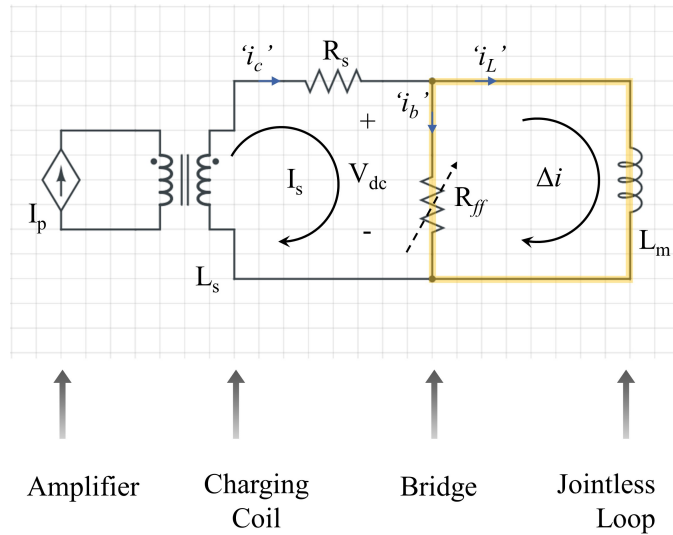


Figure 5.2: An equivalent circuit model of a flux pump charging a jointless loop, with the loop highlighted in yellow.

In Figure 5.2, the equivalent circuit of the self-switching flux pump is presented. This circuit is similar to the one discussed in Section 4.3.4. The equivalent circuit is a mathematical representation of the physical components of the system, and it is used to analyze and understand the behavior of the system. The equivalent circuit of the self-switching flux pump comprises of three main components: the joint resistance in the secondary winding (R_s), the flux flow resistance of the bridge superconductor (R_{ff}), and the inductance of the high-temperature superconducting loop (L_m).

The joint resistance in the secondary winding (R_s) represents the resistance of the winding caused by the contact resistance between the charging coil and magnet. The flux flow resistance of the bridge superconductor (R_{ff}) represents the resistance caused by driving superconductor into its mixed state. The inductance of the high-temperature superconducting loop (L_m) represents the energy stored in the magnetic field of the loop. These components are connected in series in the circuit.

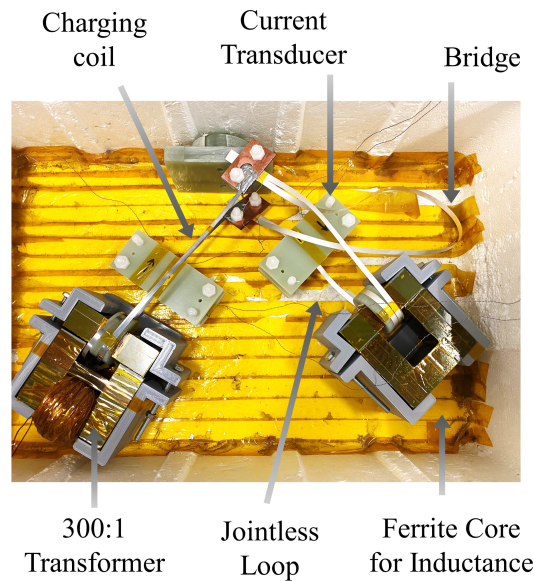


Figure 5.3: Photograph of the proposed jointless loop charging using self switching flux pump.

One significant advantage of this circuit is the absence of joint resistance in the HTS loop, which enables it to operate in the persistent current mode. The persistent current mode is a state where the current flowing through the HTS loop remains constant over time, and it is achieved by keeping the voltage across the loop constant. The absence of joint resistance in the HTS loop is essential for the proper functioning of the system, and it enables the system to achieve high efficiency and stability. The equivalent circuit of the self-switching flux pump provides a valuable tool to analyze and optimize the performance of the system.

5.2.2 Geometrical description

The HTS loop used in this study was created from a 12 mm wide and 26 cm long HTS tape with a critical current of 700 A. The tape was cut longitudinally from its center to form a loop with a diameter of 22 cm. The cutting process, however, can potentially cause degradation of the critical current due to the mechanical stress applied on the tape, as reported by Liu et al. 2016 [161]. The critical current of the loop was determined to be 350 A, which is half of the

critical current of the HTS tape. The HTS loop is a single-turn coil, which means that it has only one winding.

To increase the inductance of the single-turn loop, a ferrite core was placed on one side of the loop. Ferrite cores are commonly used in electrical engineering to increase the inductance of a coil. The other side of the loop, which acts as a bridge, consists of a straight HTS tape with zero anticipated inductance. The addition of the ferrite core increases the inductance of the coil, which allows for greater energy storage in the magnetic field.

A set of three HTS tapes were placed in parallel to form the charging coil. Each tape was 4 mm wide and 35 cm long, with a critical current of 190 A. The charging coil had terminals at both ends, which were connected to the jointless loop. A 300:1 transformer was used to induce a current in the charging coil, with the primary side made of copper wire and the charging coil serving as the secondary. The transformer is used to step-up the voltage and step-down the current to achieve the desired charging current.

The experimental setup for the loop charging is shown in Figure 5.3. It illustrates the HTS loop, the ferrite core, the charging coil, and the transformer used in the experiment. The experimental setup is designed to charge the HTS loop and measure the critical current of the loop. The charging current is controlled by adjusting the voltage on the primary side of the transformer and the critical current is measured by applying a small test current on the secondary side of the transformer. The experimental setup is designed to allow accurate measurement of the critical current of the loop and to study the effect of the ferrite core on the inductance and performance of the HTS loop.

5.2.3 Experimental Results for Loop Charging

The jointless loop was charged using the self-switching flux pump according to the procedure described in Section 4.4. An asymmetric current signal was applied to the primary of the transformer, inducing a current in the charging coil. At the positive peak of the applied current, the charging current exceeded the critical current of the loop and drove it into the flux flow region, resulting in a voltage across the loop and the injection of a small DC current. Figures

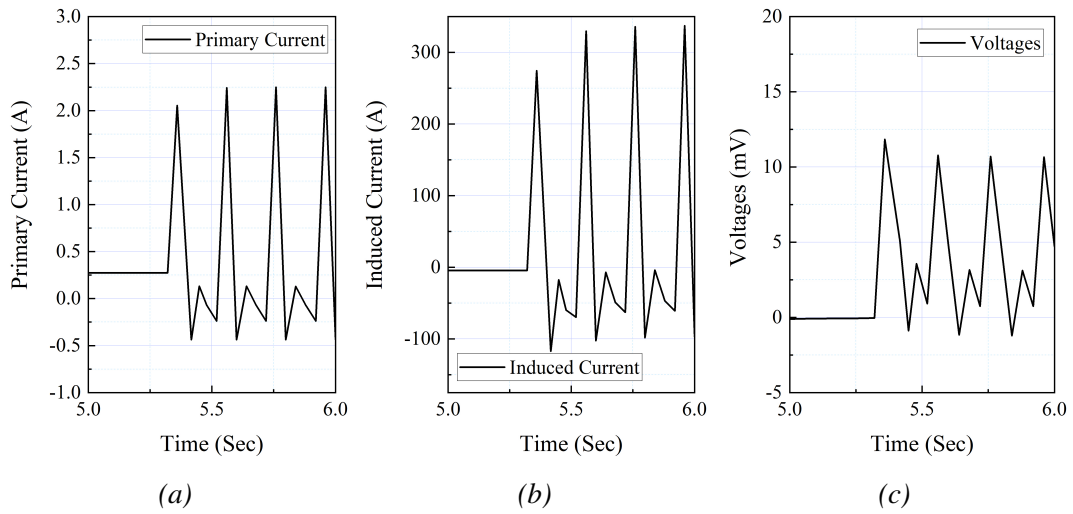


Figure 5.4: Results of the loop charging using the flux pump. (a) Asymmetric applied current waveform, (b) Induced current in the charging coil of the flux pump, and (c) Voltage measured across the loop.

5.4 show the applied current, induced current, induced voltage, and Figure 5.5 show resulting DC current injected into the jointless loop, respectively.

Figure 5.5 demonstrates the operation of the flux pump, which injects a current into the loop until 1150 seconds. From 1150 seconds to 1650 seconds, the flux pump is turned off and the loop exhibits persistent current behaviour. The temperature of the loop is then raised (deliberately to discharge the current in the joint less loop), returning it to its normal state and

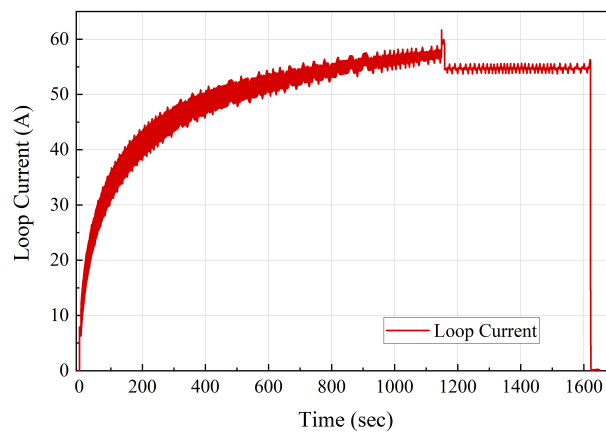


Figure 5.5: Current plot of the jointless loop charged via self switching HTS flux pump.

dissipating the current after 1650 seconds.

The magnetic field at the center of the loop can be calculated using Biot-Savart law. The expression for the magnetic field is given by following equation

$$B = \frac{\mu_0 I}{4\pi R^2} \oint dL = \frac{\mu_0 I}{4\pi R^2} 2\pi R = \frac{\mu_0 I}{2R} \quad (5.1)$$

In this equation, $\mu_0 = 4\pi \times 10^{-7} \text{ TmA}^{-1}$ is the permeability of free space, I is the current in the loop, and R is the radius of the loop. The calculated magnetic field plot is illustrated in Figure 5.6.

This experiment serves as a preliminary step towards injecting current into a jointless HTS loop. The results obtained from this experiment can be scaled up to create a jointless magnet by cutting longer pieces of HTS tape and winding them into a jointless coil. In later sections, we will provide a detailed discussion of the operation of this circuit in the persistent current mode, as well as the use of closed-loop feedback control for HTS magnets.

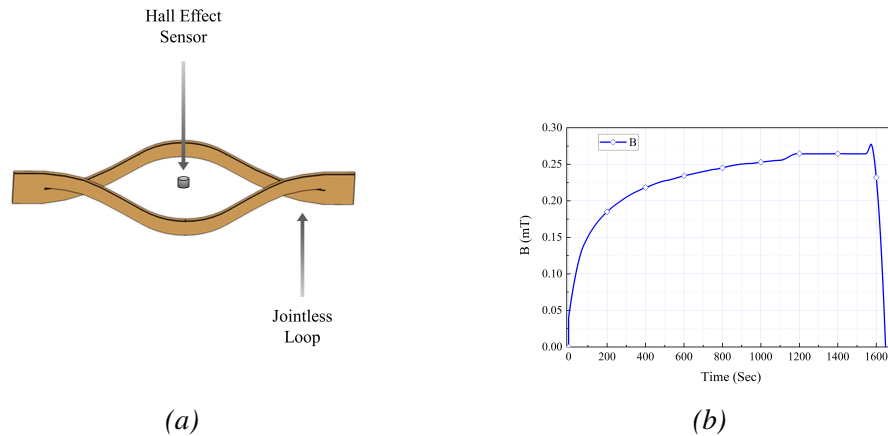


Figure 5.6: (a) Schematic illustration of the jointless loop. (b) Calculated magnetic field plot for the jointless loop.

5.3 Jointless HTS Magnet

The HTS magnet used in this study is constructed from 12 mm-wide YBCO 2G HTS tape, with an average critical current of 495 A. The tape is cut longitudinally and wound into a

double pancake structure, each with a width of 6 mm and a former diameter of 70 mm. One pancake is flipped to align the magnetic field in the same direction. The preparation of the jointless HTS magnet poses challenges, as cutting the tape can introduce mechanical stress and degrade the critical current, as Liu et al. shows in [161]. Measuring the critical current of such a coil can be difficult, but one approach is to induce flux creep by saturating the coil, as Chaudhari et al. in [162] and Kumar et al. in [163] showed. In HTS coils, flux flow and creep-related losses may occur as the coil approaches the critical state. The current plot in Figure 5.12 demonstrates that the magnet saturates at 110 A and decays to 85 A due to flux creep when the charging is switched off.

5.4 Field modulation in HTS magnets using closed-loop feedback control

Closed-loop control systems are desirable in systems that are more sensitive to disturbances because of their ability to modify the natural dynamics of a system and stabilize it, which is a key feature of any closed-loop system. In contrast, open loop systems, such as previously reported flux pumps, do not have control over the current state of the system. In the closed-loop control system described here, the set point for the required magnetic field is assigned, and the error between the magnet current and the set point is obtained. Based on the magnitude of the error, a control block calculates the required voltage and corresponding current needed to charge the magnet. This current value is then fed to a limit block that is in place to protect the HTS-CC from quenching; in this case, the limit is set to be 120% of the critical current of the HTS bridge. The signal generation block generates an analogue signal based on the current value, which is fed into an amplifier. The amplifier is connected to the primary of the transformer, inducing the charging current on the secondary coil. When the charging current exceeds the critical current of the bridge, a voltage appears across the bridge, causing flux pumping into the HTS magnet.

The block diagram in Figure 5.7 illustrates the proposed closed-loop feedback control

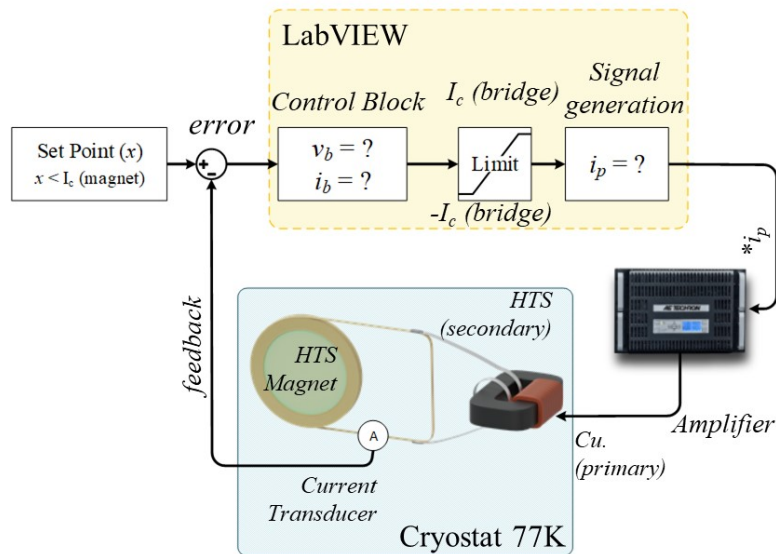


Figure 5.7: Block diagram of the closed-loop feedback control system for HTS magnets. The algorithm is implemented in LabVIEW. The control block reads the error, estimates the necessary bridge voltage, and determines the current required to generate the estimated bridge voltage. The signal is subsequently limited to protect the HTS from potential damage due to overcurrent. The signal generation block writes the signal for the amplifier. The amplifier produces the input signal for the primary side of the transformer.

HTS flux pump. The control algorithm, implemented using LabVIEW, estimates the required voltage for injecting flux into the HTS magnet and generates an input signal for the primary of the transformer to achieve flux pumping. In self-switching HTS flux pumps, the flux injection is achieved by driving the superconductor into the mixed state, but the non-linear $V-I$ characteristics at this state can present a difficulty in accurately estimating and controlling the flux injected into the HTS magnet. Our results show that this difficulty can be overcome through the use of the proposed control system.

5.4.1 Voltage prediction in HTS-CC

To predict the voltage across an HTS coated conductor in the mixed state, the structure of the conductor must be taken into account. Second generation (2G) HTS conductors are composed of multiple layers, including a high-temperature superconducting layer, a substrate

(Hastelloy) layer, a buffer stack layer, two silver overlays, and two electroplated copper layers [94]. The resistivity of the metal layers is well-known, but the resistivity of the HTS layer can be characterized using the E - J Power Law.

$$\rho_{hts}(I_c) = \frac{V_c}{I_c} \times \left(\frac{I}{I_c} \right)^{n-1} \quad (5.2)$$

Where, ρ_{hts} is resistivity of HTS layer, V_c is voltage criterion 10^{-4} V, I_c is critical current of HTS tape, I is the transport current, and n is the exponent of power law. As the transport current exceeds the critical current value of the superconducting layer (YBCO), it enters the mixed state (flux flow regime) and redistributes itself to other metal layers [164]. The net voltage due to flux flow resistivity can be calculated using the following formula

$$\begin{aligned} \frac{V}{l} &= I_T \cdot \frac{\rho_{hts} \cdot \rho_{layer}}{\rho_{layer} \cdot S_{hts} + \rho_{hts} \cdot S_{layer}} \\ \frac{R_{ff}}{l} &= \frac{\rho_{hts} \cdot \rho_{metal}}{\rho_{metal} \cdot S_{hts} + \rho_{hts} \cdot S_{metal}} \end{aligned} \quad (5.3)$$

Where R_{ff} is flux flow resistance, ρ_{hts} is resistivity of HTS layer, S_{hts} is cross-sectional area of HTS layer, ρ_{layer} is resistivity of metal layers, S_{layer} is cross-sectional area of metal layers and l is the length of the HTS tape. In Equation 5.3 the resistivity of the metal layers is known [165, 166] except the YBCO layer. Assuming the current density and electric field to be uniform across the length (l) of HTS tape, the electric potential and current density of an HTS tape can be derived as

$$|E(t)| = \frac{V(t)}{l}, \quad |J(t)| = \frac{E(t)}{\rho_{layer}} \quad (5.4)$$

Where $V(t)$ is measured voltage across the HTS tape, and ρ_{layer} is the resistivity of metal layers. The current in each layer can be obtained by integrating the current density over the cross section of each layer. If I_{total} is the total measured current, the current in HTS layer I_{hts} can be obtained as

$$I_{hts}(t) = I_{total}(t) - \sum_{i=1}^{n_{layer}} I_i^{layer}(t) \quad (5.5)$$

Knowing the cross section area of the HTS layer, the resistivity of HTS layer ρ_{hts} can be obtained as

$$\rho_{hts}(I) = \frac{V(t)}{I_{hts}(t)} \times \frac{S_{hts}}{l} \quad (5.6)$$

The flux flow resistance value can be accurately calculated by substituting equation 5.6 into equation 5.3.

5.4.2 Voltage estimation via FEA modeling and experimental verification

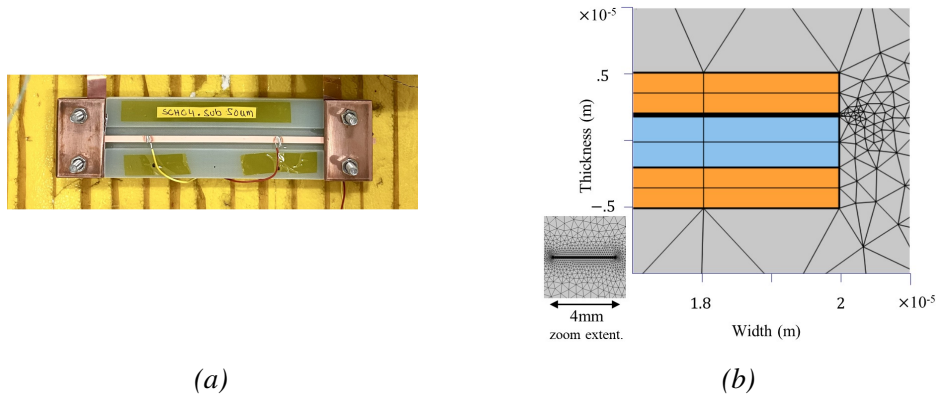


Figure 5.8: (a) Sample of HTS tape to test record the voltage when the HTS tape is subjected to over critical current, and (b) 2D FEM model of HTS tape in COMSOL, layer dimensions are given in Table 5.1 and physics parameters are in Table 5.2. A pulse of a current $1.2 \times$ critical current of HTS tape is applied and the response is recorded. On left a zoom extent view of a 4 mm wide HTS tape is illustrated.

The validity of the system of equations presented in Section 5.4.1 was verified through a series of experiments and simulations on a high-temperature superconducting (HTS) tape sample. The sample was prepared and the critical current values were measured at 77 K under self-field conditions using a $1 \mu\text{V}$ criterion. This criterion is used to determine the critical current of the sample, which is the maximum current that the sample can carry without losing its superconductivity. The sample's geometry and design parameters are illustrated in Figure 5.8 and presented in Tables 5.1 and 5.2. The measured critical current value was 145 A.

Table 5.1: Design parameters for layers of HTS tape subject to over critical current resistivity measurement.

Definition	Quantity	Unit
Width of HTS tape	4	mm
Length of HTS tape	8	cm
Thickness of HTS layer	1	μm
Thickness of Copper layer	40	μm
Thickness of silver layer	2	μm
Thickness of buffer layer	2	μm
Thickness of Ni-based substrate	50	μm

Table 5.2: Parameters employed in FEM simulation for layers of HTS tape subject to over critical current resistivity calculation.

Definition	Quantity	Unit
N-Value	21	
Critical Electric Field E_c	$1E^{-4}$	Vm^{-1}
Resistivity of air ρ_{air}	1	Ωm
Resistivity of copper Cu_{air}	$1E^{-8}$	Ωm
Permeability of free space μ_0	$4\pi E^{-7}$	NA^{-2}
Critical Current I_c	145	A

The sample was then analyzed using finite element simulation (FEM), which is a numerical technique used to analyze and solve complex problems in engineering and physics. A current pulse with an amplitude of 1.4 % of the critical current was applied to the sample, and the voltage across the layers of the tape was then measured and compared to laboratory experimental results, as shown in Figure 5.9. The results showed that when the transport current exceeds the critical current value, it is distributed among the other metal layers, and the induced voltages across the sample are proportional to the resistivity of these layers.

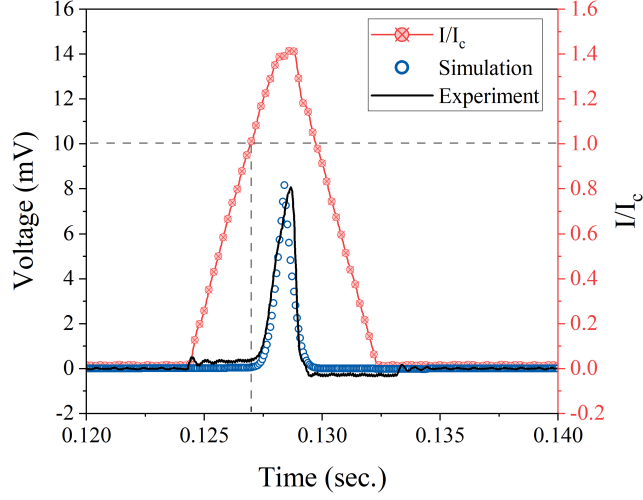


Figure 5.9: Voltage profile for 8 cm long HTS tape measured experimentally and calculated by FEM simulation against normalized applied current (I/I_c).

The equations described in this paragraph are the key to the proposed control system. They allow for the control system to estimate the required voltage for injecting flux into the HTS magnet, while also considering the potential quenching of the HTS tape caused by excessive currents.

5.4.3 Equivalent Circuit Model

To establish a relationship between the primary current (input) and the voltage across the bridge, a simplified magnetic circuit model can be considered as illustrated in Section 5.2.1. When the transport current is below its critical value, the secondary coil is short-circuited by the bridge and the flux flow resistance does not appear. Thus, the load side of the circuit can be neglected under this condition. By applying Kirchhoff's voltage law, the following expressions can be obtained

$$L_p \frac{di_p}{dt} + M \frac{di_s}{dt} + i_p R_1 = 0, \quad (5.7)$$

$$L_s \frac{di_s}{dt} + M \frac{di_p}{dt} + i_s R_s + i_s R_{ff} = 0 \quad (5.8)$$

Where L_p is the inductance of the primary coil, L_s is the inductance of the secondary coil, M is mutual inductance, R_1 is ohmic losses in the primary winding and R_s is the total resistance due to soldering joint in the secondary side. The mutual inductance of the transformer can be regarded as

$$M = \frac{\phi_c(i_p)}{i_p}, \quad (5.9)$$

The flux ϕ_c through the transformer core can be calculated by solving the magnetomotive force due to the applied current over the reluctance of the transformer core. Substituting Equation 5.9 into Equations 5.7 and 5.8 yields an expression for the induced current i_s with respect to the applied current i_p . The voltage across the bridge is caused by the flux flow resistivity. By understanding the relationship between the applied and induced currents, we can represent the flux pump in a simplified circuit diagram by replacing the excitation circuit with a current-controlled voltage source, as shown in Figure 5.10. The following equation represents the relationship between the current flowing through the load magnet and the

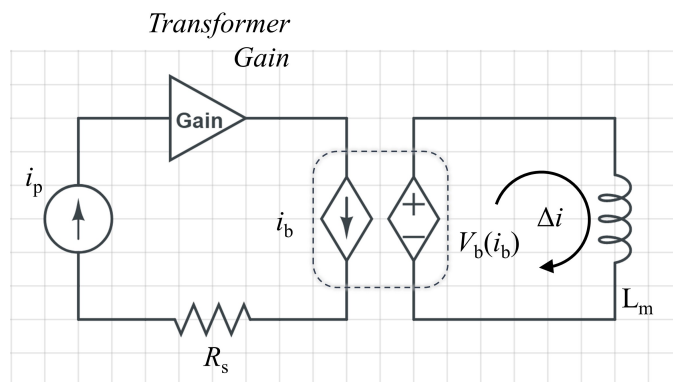


Figure 5.10: Simplified circuit model representing bridge as a current controlled voltage source, transformer is represented by Gain and the solder joint by R_s .

voltage across the bridge caused by flux flow resistivity

$$\Delta i = \frac{1}{L_m} \int_0^T v_b dt \quad (5.10)$$

5.5 Experiment

The experimental setup, shown in Figure 5.11, consists of a transformer and a jointless high-temperature superconducting magnet. The HTS magnet is made of 12 mm wide, 6 m long YBCO 2G HTS tape with an average critical current of 495 A. It was cut longitudinally at its center and wound into a double pancake structure, with each pancake having a width of 6 mm and a former diameter of 70 mm. One pancake was flipped to align the orientation of the field in the same direction. One side of the jointless HTS coil was extended to form the “bridge”. The secondary side of the 300:1 transformer was made of HTS tape with a critical current of 700 A, and the terminals were soldered to either side of the bridge, creating the return path for the induced current. The critical current of the bridge is ≤ 248 A. Two

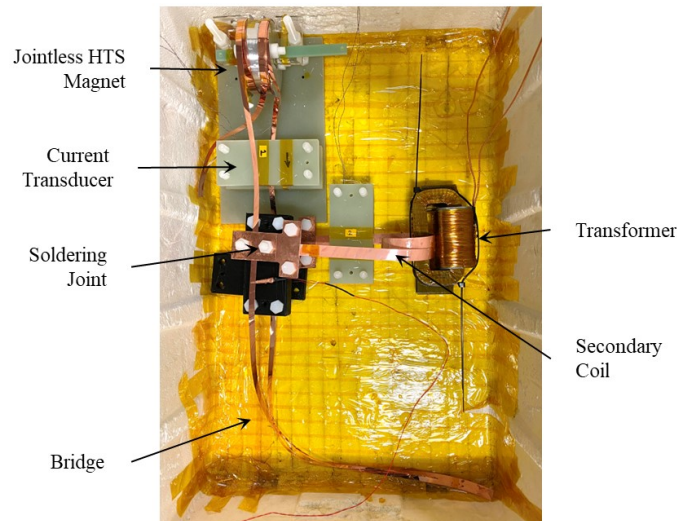


Figure 5.11: Photograph of proposed flux pump to charge HTS magnet in persistent current operation. Magnet is prepared in jointless fashion and the flux pump is operated in closed-loop feedback control, where a LabVIEW based control calculates the voltage required to inject the required current into the HTS magnet.

pre-calibrated current transducers were used to measure the induced voltage on the secondary side and the current in the magnet and provide a feedback signal. A twisted lead voltage tap across the bridge was used to record the voltage. The feedback control was implemented in LabVIEW, with voltage and current readings measured by an NI-9238 DAQ card and the current signal generated by an NI-9263 DAQ card. The power amplifier AE-Techron 7766 was used to generate the primary current for the transformer [167].

5.5.1 Control algorithm in LabVIEW

The control algorithm for implementing the closed-loop feedback control for HTS flux pumps was performed using LabVIEW. This programming platform was chosen for its ability to handle real-time data acquisition and control, as well as its user-friendly interface. To achieve this, two synchronous channels were implemented in LabVIEW, one for data reading and another for generating responses to the hardware. These channels were initialized together and the physical channel as well as the data rates were assigned outside the main loop.

The main loop of the program continuously monitors the HTS magnet current and feeds the result back to the signal generation block. This block then calculates the required voltages and the amplitude of the applied current for generating these voltages. Once the calculations are finished, the applied current signal is written to the signal generation channel, which excites the hardware and controlled pumping action takes place.

This closed-loop feedback control technique enables real-time monitoring and control of the HTS magnet current, ensuring stable and precise flux modulation. Furthermore, to record the generated voltages, applied current and induced current, another LabView file was created using the out-of-the-box DAQ Express tool. This enables further analysis of the data and provides a more comprehensive understanding of the performance of the flux pump.

This approach of using LabVIEW as a control algorithm platform for HTS flux pumps allows for greater flexibility and precision in controlling the magnet current and voltage, ultimately leading to more efficient and stable operation of HTS magnets in persistent current mode. It is an innovative and efficient method for achieving flux pumping in HTS magnets,

which can be easily adapted and implemented in various applications.

5.5.2 Critical Current of a Jointless HTS Magnet

The preparation of a jointless HTS magnet is a crucial step in the development of high-performance superconducting systems. The HTS tape, which is used in the construction of the magnet, is cut down the center using mechanical roller blades. However, this process can potentially cause degradation of the critical current due to the mechanical stress applied on the tape, as reported in [161]. Measuring the critical current of a jointless coil using the four-probe method can be challenging [162], but one approach that has been proposed in the literature is to saturate the coil to the point where the phenomenon of flux creep occurs [163].

In HTS coils, there should be no DC losses in theory, but when the coil approaches the critical state, flux flow and flux creep-related losses may occur. The current plot of the jointless magnet used in this study is shown in Figure 5.12, it demonstrates that the magnet saturates at 110 A and decays to 85 A due to flux creep after the charging is switched off. The flux creep is a phenomenon that occurs in HTS magnets, it is characterized by the gradual increase in resistance with time when the magnet is in the superconducting state. The flux

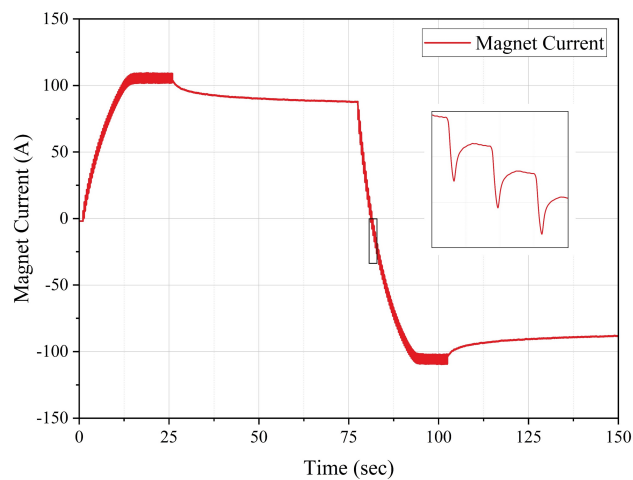


Figure 5.12: A jointless HTS magnet is charged to its critical current value using flux pump and flux pump is switched OFF at time $t = 26$ sec, the current decay can be observed due to self field flux creep at critical state and the current stabilizes at 85 A.

creep-related losses are related to the microstructure of the HTS tape and the current density. The critical current density is a measure of the ability of the HTS tape to carry current without losses.

To understand the behavior of the HTS magnets an equivalent circuit model is often used. This model consists of a series connection of a resistance and a inductance that represents the magnetic energy stored in the magnet. The resistance represents the losses in the magnet, while the inductance represents the energy stored in the magnetic field. The equivalent circuit model is a useful tool for understanding the behavior of the HTS magnets and can be used to predict the performance of the magnet under different operating conditions.

In conclusion, the preparation of a jointless HTS magnet is a critical step in the development of high-performance superconducting systems. Measuring the critical current of a jointless coil can be challenging, but one approach is to saturate the coil to the point where the phenomenon of flux creep occurs. The current plot of the jointless magnet used in this study is shown in Figure 5.12, it demonstrates the magnet saturates at 110 A and decays to 85 A due to flux creep after the charging is switched off. An equivalent circuit model is a useful tool for understanding the behavior of the HTS magnets and can be used to predict the performance of the magnet under different operating conditions.

5.5.3 Field modulation of HTS magnet using closed loop feedback control

The magnetic field of the jointless HTS magnet is modulated by injecting and removing current. The current plot of the HTS magnet is shown in Figure 5.13. The set point, which is the desired current level, is initially set to 80 A. At the start of the process, the current in the magnet is zero, so the error between the current and the set point is at its maximum. To rectify this, the control system calculates the required voltage for flux pumping based on the bridge voltage and generates a primary current signal that is sent to the amplifier. This process is repeated continuously until the set point is reached.

Once the set point is reached, the required voltage is reduced to zero and the primary

signal becomes zero, resulting in the HTS magnet operating in self-field persistent current mode (shown in Figure 5.13 from time $t = 10$ s to $t = 22$ s). In this mode, the magnet maintains a constant current without the need for any external voltage.

At time $t = 22$ s, a new set point ($x = 25$ A) is assigned and the control system recalculates the voltage required to remove the current from the jointless HTS magnet, generating the corresponding input current signal. At this iteration, the primary current direction is reversed to produce negative voltages across the bridge. The new set point is reached at $t = 25$ s, and the primary signal is switched off, allowing the HTS magnet to operate in persistent current mode again. The set point is similarly changed to $x = 40$ A, $x = 50$ A, $x = 60$ A, $x = 70$ A, $x = 75$ A, and $x = 80$ A, with the primary current switched off and the HTS magnet operating in persistent current mode after each set point is achieved. This process is repeated multiple times with different set points to validate the accurate operation of the closed-loop feedback control for modulating the HTS magnet's field. The set points are chosen and repeated in order to evaluate the system's ability to accurately and consistently regulate the HTS magnet's field.

The relation between the charging current (secondary) i_s , the bridge current i_b and the

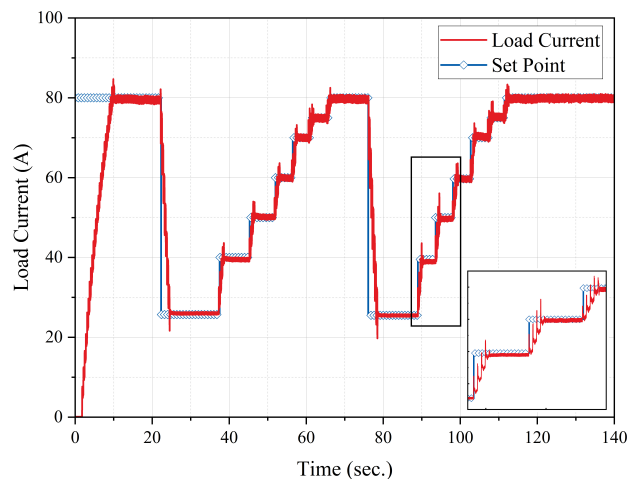


Figure 5.13: The current in the HTS magnet against the set-point value, the current plot illustrates the field modulation in the HTS magnet and accurate reference tracking in feedback control for a flux pump.

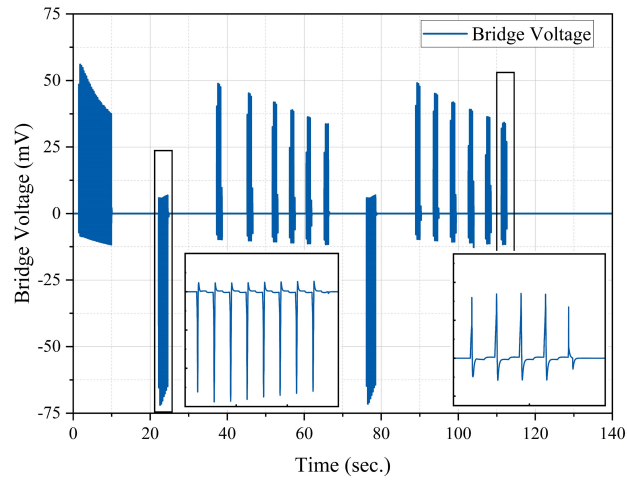


Figure 5.14: The voltage measured across the bridge during field modulation in HTS magnet.

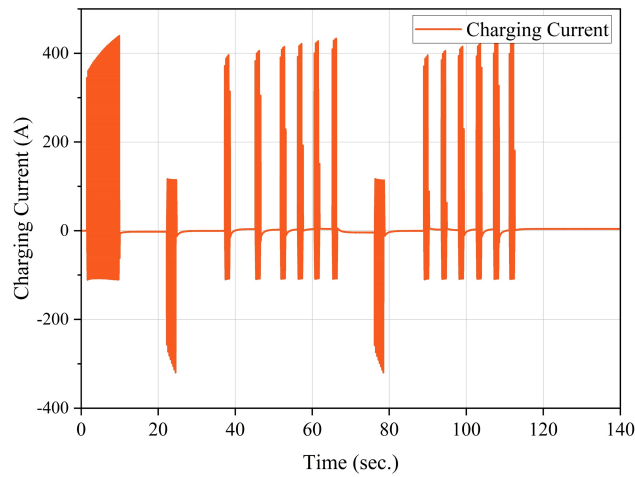


Figure 5.15: The charging current plot in the HTS secondary side of the transformer.

load current Δi can be given as;

$$i_s = i_b + \Delta i, \quad (5.11)$$

With the increase in the load current, the DC current starts to run through the bridge and the bridge current now has both AC and DC components, due to this a DC biasing in the bridge voltage plot can be seen in Figure 5.14. The charging current plot is shown in Figure 5.15. During the first cycle, the charging current is equal to the bridge current since the load current (Δi) is zero. As the load current accumulates, the bridge current becomes biased in

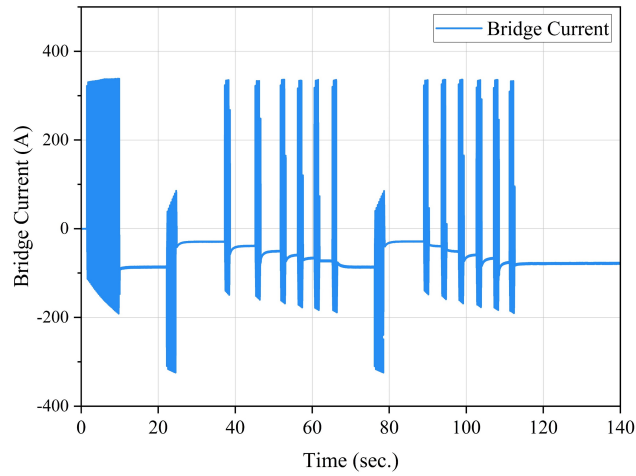


Figure 5.16: The bridge current plot i_b in HTS flux pump.

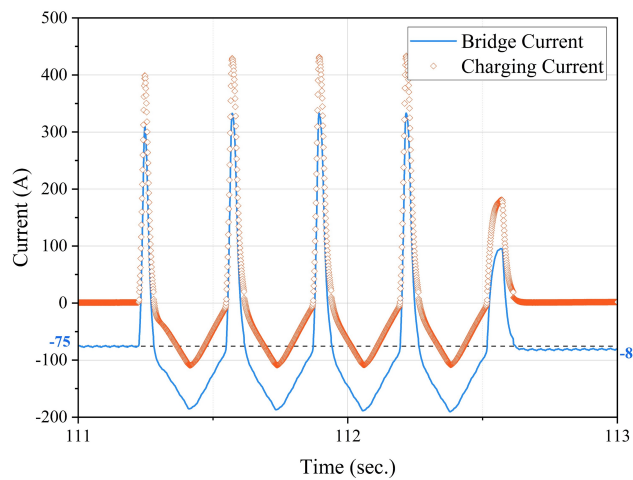


Figure 5.17: The bridge current vs charging current plot while charging an HTS magnet by closed loop feedback control operated flux pump.

the opposite direction. The magnitude of the charging current is automatically adjusted to keep the peak of the bridge current constant in each cycle, as illustrated in Figure 5.16. This is an important feature of the control system, as it ensures that the bridge current remains within safe operating limits, and that the system is able to maintain accurate control over the magnetic field of the HTS magnet.

When the load current reaches its set point limit, the input signal returns to zero and the corresponding charging current is also reduced to zero. However, due to the jointless

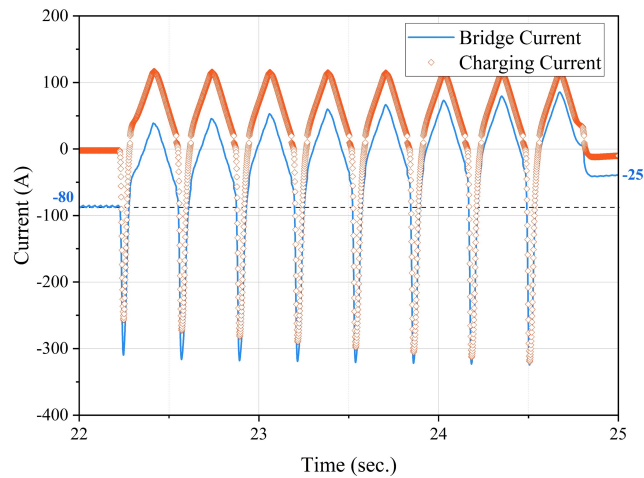


Figure 5.18: The bridge current vs charging current plot while charging an HTS magnet by closed loop feedback control operated flux pump.

geometry of the HTS magnet, we observe a persistent current flowing in the bridge. This is a characteristic of the HTS magnets that are operated in persistent current mode, and it is a result of the absence of joint resistance in the HTS loop. Figures 5.17 and 5.18 show the charging and discharging cycle of the HTS magnet and its corresponding bridge and charging current in detail. The magnitude of the peaks in the bridge current is nearly constant, indicating the accurate performance of the voltage calculation block in the feedback control. This means that the system is able to modulate the magnetic field of the HTS magnet with a high degree of precision, which is a crucial requirement for many applications that use HTS magnets.

5.5.4 Precision in closed loop feedback control of HTS magnet using flux pump

In a broad range of applications, closed-loop feedback control is extensively employed due to its ability to precisely modify the system in real-time. This type of control is especially important for applications where high precision is required, such as in the case of high-temperature superconducting (HTS) magnets. In this study, the implemented closed-loop feedback control system has been shown to precisely modulate the current of the HTS magnet

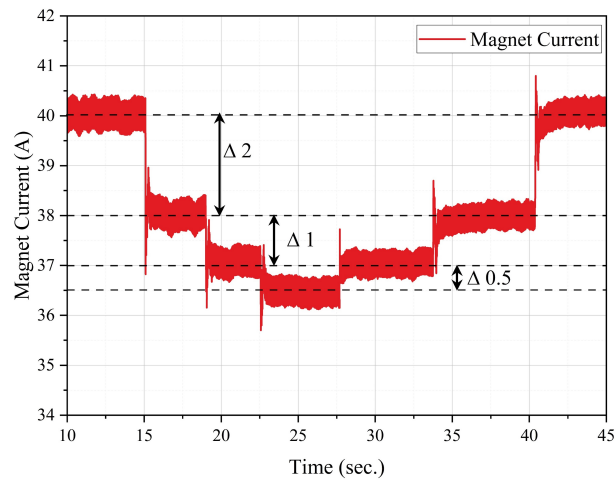


Figure 5.19: The current modulation in jointless HTS magnet indicating the precision control by removing the current from the magnet and injecting exactly the same amount.

by as little as 0.5 A, as illustrated in Figure 5.19.

It is worth noting that the precision of this control system is dependent on the inductance of the HTS magnet. In this study, the inductance of the HTS magnet is relatively low at $\sim 1.10 \mu\text{H}$, and small changes in load current may be difficult to quantify due to large ripple noise. However, for magnets with higher inductance values, the precision of the control system can be significantly improved.

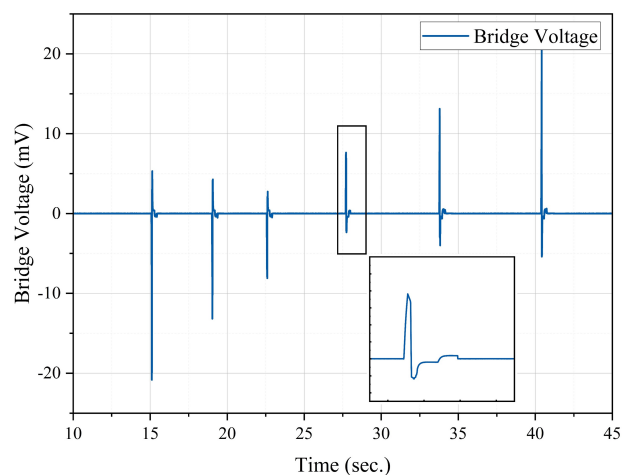


Figure 5.20: The induced voltages across the bridge to precisely remove and inject the current in an HTS magnet.

The corresponding voltage induced across the bridge to inject or remove current from the magnet is illustrated in Figure 5.20. This is a significant step towards achieving an ultra-stable DC source for HTS magnets. The results of this study demonstrate the potential of using closed-loop feedback control in HTS magnets, and the possibility of achieving high precision in the modulation of the magnetic field in these magnets.

5.5.5 Discussion

The proposed closed-loop control for flux pumping in HTS magnets presents an improvement over previously reported flux pump designs. As previously reported, these flux pumps are suitable for rapid pumping of currents in large magnets, but they may not be ideal for field stability. This is due to the sharp $V-I$ curve of the bridge superconductor, which makes it difficult to achieve effective control of the bridge voltage. A small noise in the bridge current can induce a large error in the bridge voltage.

Previous studies have addressed this problem by using an additional field source perpendicular to the bridge superconductor [29, 30], also explained in Section 3.3.2. However, this approach has several drawbacks. It increases the heat load on the cryogenic system, enlarges its footprint, and operates in an open-loop control. In contrast, the proposed closed-loop control can provide on-demand stable dc voltages to precisely energize the magnet. This enables flux pumping at stable dc voltages and achieving persistent current operation in HTS magnets.

In theory, a 55 mV can instantly establish a current of 80 A in the HTS magnet. However, realizing this high voltage in the HTS bridge is only possible in the flux flow regime. In the flux flow regime, the current is shared by other metal layers, which can produce heat among layers and quench the superconductor. Therefore, the superconductor is driven into the flux flow regime for a fraction of a second, and current is injected into the magnet. During each cycle, the feedback loop recalculates the required voltage and keeps on injecting the current until the set point is reached.

The closed-loop feedback control can limit the excessive current into the HTS bridge,

hence protecting the system from quenching or overcurrent damage. The proposed closed-loop control for flux pumping in HTS magnets presents a significant improvement over previously reported flux pump designs, it provides a more stable and precise flux pumping, and it protects the system from damage. This makes the proposed closed-loop control a more desirable solution for the flux pumping of HTS magnets.

5.6 Conclusion

In this chapter, the process of charging a jointless loop and jointless magnet using a self-rectifying flux pump was presented. The initial study was conducted to demonstrate the successful charging of the jointless loop, which opens up new possibilities for building jointless magnets that can operate in persistent current mode. Additionally, a closed-loop feedback control method for flux modulation of HTS magnets in persistent current mode was presented. The experimental results show that the proposed control technique can precisely induce a DC voltage across the HTS bridge, resulting in effective flux modulation. Unlike conventional flux pumps, where the DC voltages across the bridge are not controlled, the pumping speed in this method relies on the frequency and amplitude of the applied signal. Furthermore, the precision in flux modulation was demonstrated by removing an on-demand current of 0.5 A from the magnet. The control block calculated the required voltage of 7 mV to generate a corresponding current signal which drives the bridge into the flux flow regime and induces the exact voltage to inject 0.5 A. This feedback-controlled flux pump can be used in effective flux modulation of HTS magnets in persistent current operation. It removes the technical challenges associated with the use of high current power suppliers and current leads, thereby reducing the cooling requirement and footprint of HTS magnets. It also eliminates the need for additional field sources perpendicular to the bridge superconductor, reducing the heat load on the cryogenic system and minimizing the overall footprint of the system. This chapter has presented a new approach for flux pumping of HTS magnets, which is expected to be useful in a wide range of applications.

6

An HTS Flux Pump Operating at 30 K

6.1 Introduction

Superconducting magnets play a vital role in a range of advanced technologies, from NMR, MRI and superconducting motors to fusion reactor field coils. Superconducting electric machines have gained significant attention due to their potential to revolutionize the concept of fully electric aircraft, making them a prominent technology solution in recent times. Recent growing interest in all electric aircraft propulsion systems enables superconducting machines as a major contender towards zero carbon emission [168, 169, 170, 171, 172, 173]. Superconducting motors and generators offer higher power and torque densities compared to their traditional counterparts [174, 175, 176]. HTS tapes have a significantly higher current carrying capability compared to traditional conductors. For instance, the typical current density of copper winding in electric machines ranges from 4 to 6 A/mm², whereas this value can be several hundred times higher (depending on the tape material and manufacturer) for 2G HTS tapes at temperatures of 77 K or 20 K, using liquid nitrogen (LN₂) or liquid hydrogen (LH₂) as coolants. Notably, the concept of fully electric aircraft appears more achievable now, thanks to the utilization of a hydrogen-based system with fuel cells for energy storage and cooling purposes, eliminating the need for cryocoolers and batteries [177]. For instance, traditional machines typically achieve a magnetic loading of around 1 T, usually

utilizing rare-earth permanent magnets. However, with the use of 2G HTS tapes, this value can easily be increased to 3 to 4 T. This elevated magnetic loading enables the implementation of coreless/air-core topology in superconducting machines, resulting in higher power and torque densities, as well as lighter weight machines. Various topologies for these machines' field generation include traditional permanent magnets, bulk superconductors, and stacked tapes [178]. Increasing the magnetic loading in superconducting electric machines is crucial to achieve a power density target of 20 kW/kg. One promising solution for accomplishing this is the utilization of superconducting trapped-field magnets, which trap persistent currents and offer potential for enhanced magnetic loading in HTS electric machines. Several publications in the literature have focused on the development of HTS bulk magnets with high trap fields, reaching up to 17.7 T [8, 7, 179]. However, bulk magnets face significant challenges, such as mechanical vulnerability in larger sizes and the potential for cracks to appear in their construction at low temperatures. These limitations render them unsafe and unreliable as a viable option for field magnets in high-power superconducting machines intended for electric aircraft applications. To overcome these challenges, HTS magnets offer a viable solution. These are designed by implementing the concept of persistent currents operation of HTS magnet. This chapter covers the charging of HTS magnets via a self rectifying HTS flux pump. While some recent devices have achieved current capacities over 1 kA, they are designed for use in liquid cryogenics [149, 113]. The potential applications of HTS magnets in conduction-cooled infrastructure remain largely unexplored. In this chapter, we present a testing platform for a self-rectifying HTS flux pump and demonstrate its functionality at both 77 K and 30 K, including the impact of the copper heat load, laying the groundwork for potential use in conduction-cooled environments replicating the temperature of liquid H₂.

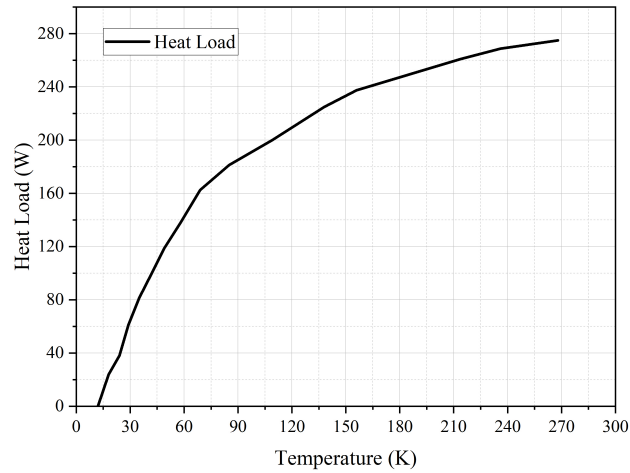


Figure 6.1: CH-110LT Cold Head Capacity Map Using F-70 Compressor at 50Hz [180].

6.2 Introduction to conduction cooling system

6.2.1 Cooling system

The cooling system utilized in this study is based on the principle of conduction cooling and is capable of reaching temperatures as low as 20 Kelvin. The system is comprised of five essential components that work together to maintain the desired temperature. The first component is the vacuum-sealed cryostat produced by ICE Oxford, which is fitted with a CH-110 cold head by Sumitomo, capacity waveform is illustrated in Figure 6.1. The second component, the helium compressor F-70 by Sumitomo, is designed to deliver high-pressure oil-free helium gas to the cryogenic refrigerators. The third component, a water chiller, helps regulate the temperature of the compressor. The fourth component is a two-stage vacuum pump by Pfeiffer, which is capable of reaching 10^{-6} HPa within the cryostat. Finally, the 336 temperature controller by Lakeshore with four channels and built-in PID control plays a crucial role in maintaining and controlling the temperature of the test subject.

It is important to note that the cooling system must maintain consistent and precise temperature control to ensure accurate results. The cryostat, as the primary component of the system, must maintain a vacuum-sealed environment to prevent contamination and

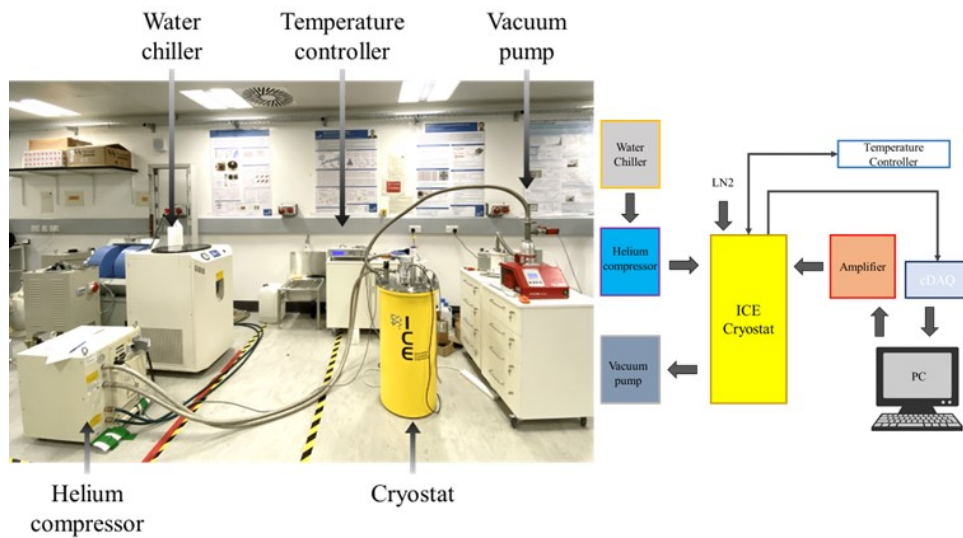


Figure 6.2: Illustration of the conduction cooling system, showcasing the cryostat, He compressor, temperature controller, vacuum pump, and water chiller. On the right, there is a block diagram of the cooling system.

preserve the low temperature. The helium compressor must provide a continuous supply of high-pressure oil-free helium gas to the cryogenic refrigerators, while the water chiller helps regulate its temperature. The two-stage vacuum pump helps maintain the low-pressure environment within the cryostat, and the temperature controller helps regulate the temperature of the test subject. The whole cooling system is illustrated in Figure 6.2.

6.2.2 Cryostat

The ICE Cryostat is a vital component of the cooling system used in this study. It is engineered to maintain extreme low temperatures, below 20 K, through conduction cooling. The cryostat is designed with a cavity capable of accommodating samples up to 290 mm in length and 300 mm in diameter, making it suitable for a wide range of experiments and tests. The cryostat features a two-stage cooling system, complete with temperature sensors and heaters to monitor and regulate the temperature of the sample under test. The first stage of the cooling system is located near the cold head and the second stage is placed near the copper plate, next to the sample holder.

Data transmission is an important aspect of any low temperature experiment, and the ICE Cryostat incorporates this seamlessly through the use of Fisher Connectors' feed-throughs. These feed-throughs allow for the safe and efficient transfer of data into the cryostat, without compromising the integrity of the low temperature environment inside.

In addition to the temperature sensors and heaters, the cryostat is equipped with a liquid

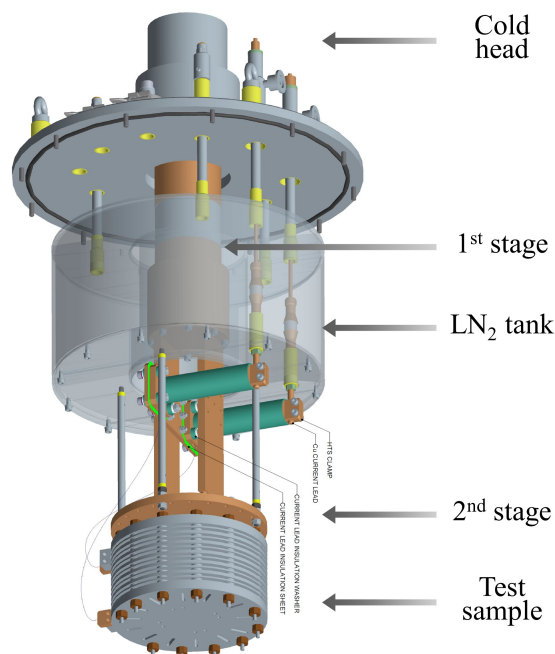


Figure 6.3: 3D Rendering of the Interior of the ICE Cryostat for Conduction Cooling [180].

nitrogen tank. This tank is used to subcool the copper leads, making it possible to inject high currents into the sample under test.

6.3 Assembly and design configuration of geometry in HTS flux pumps

6.3.1 HTS magnet

The High-Temperature Superconducting (HTS) Magnet is designed to be cooled using conduction cooling. The magnet's former is made from oxygen-free brass, measuring 10 mm in thickness and 70 mm in diameter. It has two copper terminals for easy connection to the power source. The former for the bridge, which is 12 mm thick and 120 mm in diameter, is housed on top of the magnet. The large diameter of the bridge minimizes the effect of the magnet's field on the critical current density (J_c) of the bridge. The magnet, bridge, and terminals are housed in a cup-shaped container, which is impregnated with a conductive material (to be described in a later section).

The bridge superconductor plays a crucial role in the functioning of self-switching HTS flux pumps. The current-carrying capability and configuration of the bridge significantly impact the charging process and the efficacy of flux injection, as demonstrated in Chapter 4. The design of this system integrates the bridge as part of the magnet, housed together in a cup-shaped container. The bridge superconductor is wound in a bifilar pancake configuration, with a slight modification. The magnet coil is wound into a double pancake, resulting in terminals on opposite sides. The HTS tape from the magnet coil is extended to form the bridge, with one side passed through an S-shaped slit in the bridge former to change its direction. The resulting bifilar bridge is wound over the former, as Figure 6.4a depicts.

The magnet was fabricated by winding 6 meters of HTS tape into a double pancake coil. The resulting magnet had an inductance of 32 μH and a critical current of 152 A at 77 K, measured using the criteria $E_0 = 10^{-4} \text{ V}\cdot\text{m}^{-1}$. The terminals of the double pancake coil were connected to the ends of the charging coil, while a 45 cm long HTS tape was wound into a

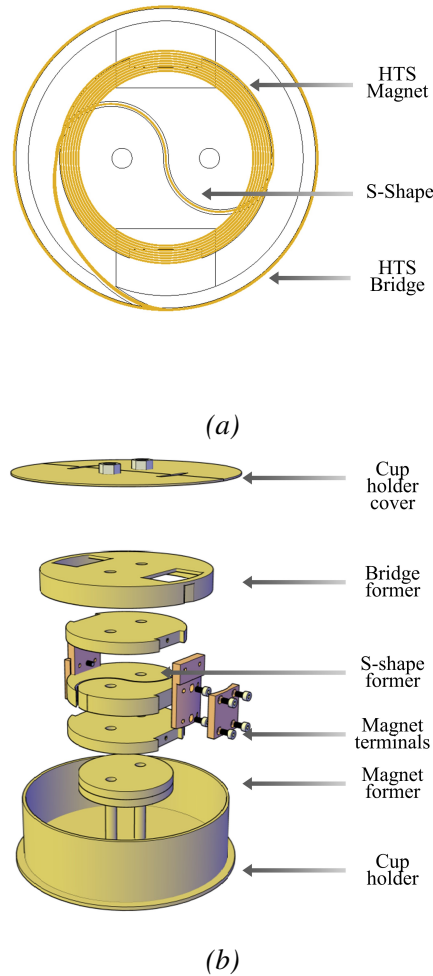


Figure 6.4: Schematic Representation of HTS Magnet and Bridge Superconductor,(a) The HTS Magnet and Bridge Superconductor configured in a bifilar pancake configuration with direction change via an S-shaped slit in the former,(b) 3D exploded diagram of the HTS Magnet former highlighting its components and design configuration.

bifilar pancake configuration to form the bridge and was connected in parallel to the magnet, resulting in a compact design as illustrated in Figure 6.5.

6.3.2 Excitation coil

The excitation circuit features a transformer with a 300:1 transformation ratio, with copper utilized on the primary side and high-temperature superconducting (HTS) tape on the secondary

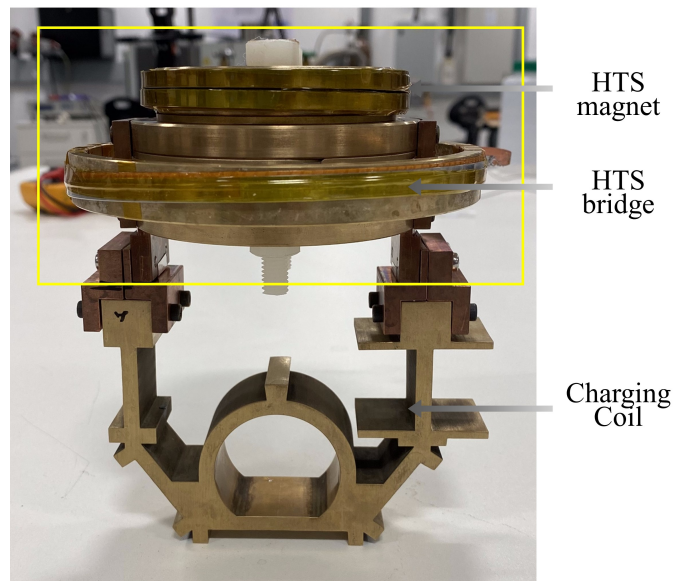
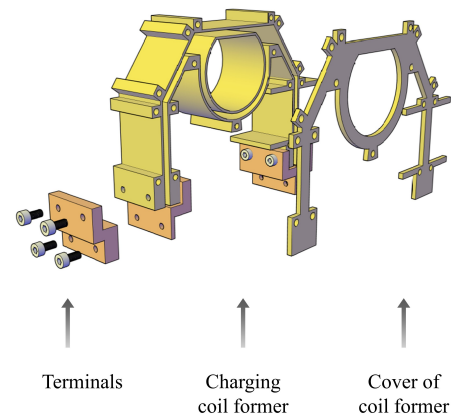


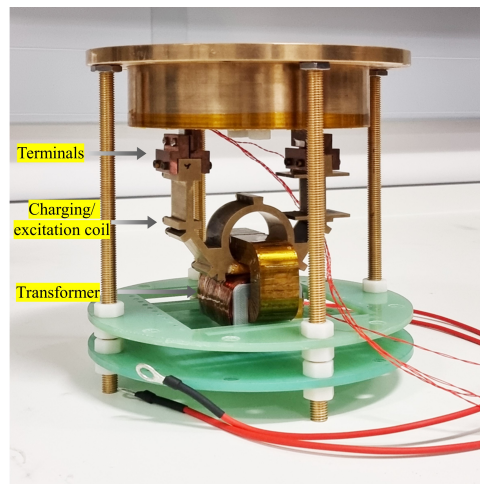
Figure 6.5: HTS Magnet and Excitation Circuit. The yellow box depicts the HTS magnet, while the bottom section shows the excitation circuit, including the charging coil housed in an oxygen-free brass former. The two components are joined together at the copper terminals using M3 bolts.

side. To serve as a charging coil, two HTS tapes were wound in parallel to create a 1-turn secondary coil with a critical current of 600 A per tape. The transformer was fabricated using amorphous cut cores from Hitachi Metals, which exhibit low core losses and high saturation flux density ($B_s=1.56$ T).

The charging coil is housed in an oxygen-free brass former, designed for conduction cooling, and is equipped with copper terminals for connection to the magnet. Oxygen-free brass is used due to its increased tensile strength and improved thermal conductivity. The former, which will be impregnated with thermal conduction material and sealed with a cover, is depicted in Figure 6.6 and is equipped with a hole to accommodate the U-shaped core of the transformer. One side of the former has been molded to hold a current transducer, allowing for measurement of the induced current in the charging coil. The terminals of the excitor and magnet are joined using M3 bolts with an indium film in-between to guarantee proper contact and minimize airgap resistance.



(a)



(b)

Figure 6.6: Image of HTS flux pump, (a) exploded diagram of charging coil former: showcasing components and terminals with adjoining bolts, (b) final assembly image showcasing transformer, HTS secondary/excitation coil and HTS magnet.

6.3.3 Impregnation of a sample under study

The HTS magnet and charging coil are housed in a brass former and it is crucial to distribute cooling/heating evenly across the superconductor, including portions not in direct contact with the former. In this study, conduction cooling is used, making impregnation a crucial aspect in achieving a cooling temperature of 30 K. Previous research by Kandasamy et al. showed that phase change materials provide an effective heat sink with improved thermal performance in

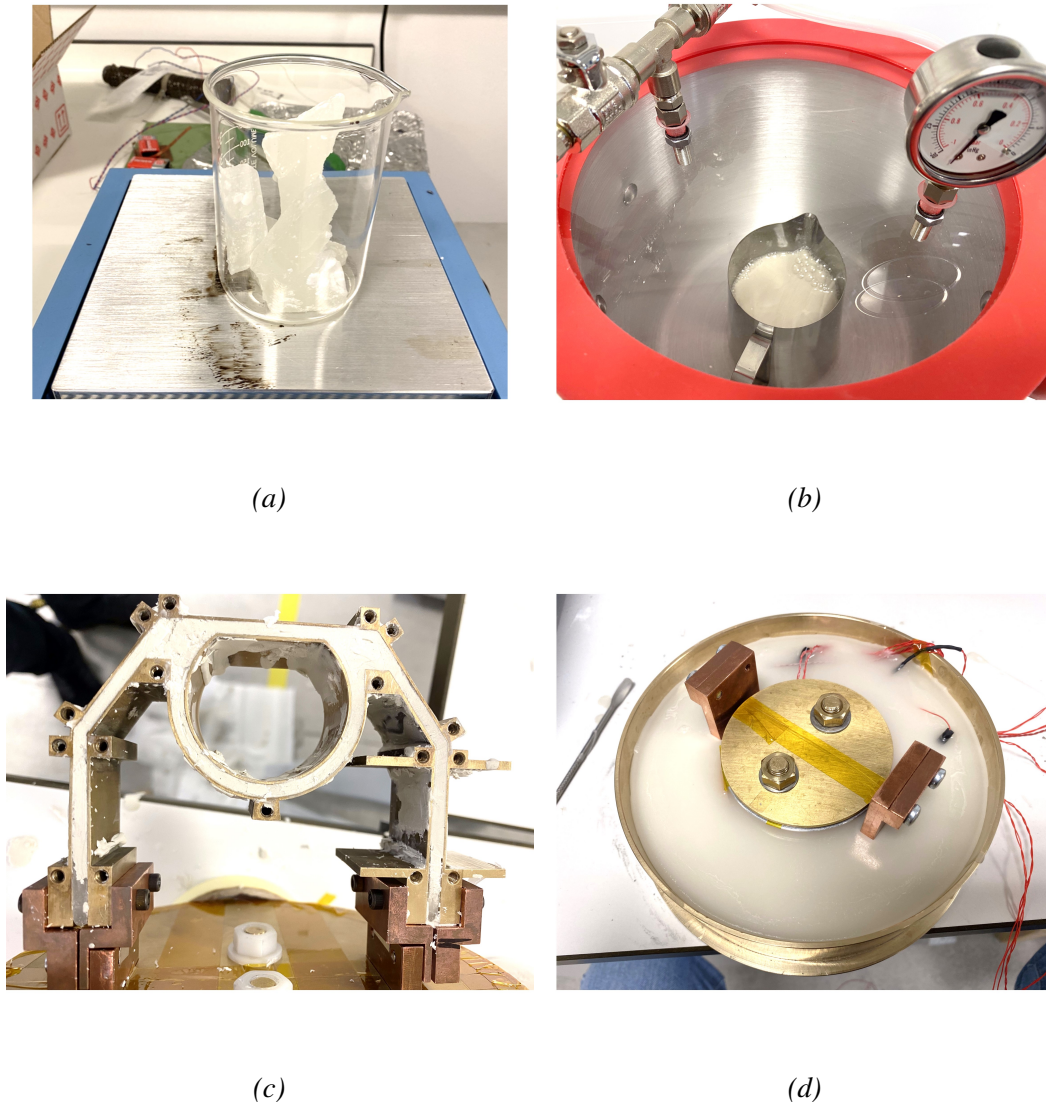


Figure 6.7: Impregnation of HTS magnet: (a) Melting of paraffin wax at 60 °C, (b) Degassing the mixture, (c) Charging coil after impregnation, and (d) HTS magnet after impregnation.

[181]. Ideal phase change materials possess high thermal conductivity, high specific heat and density, long-term durability, and reliable freezing behavior. Among various classes of phase change materials, paraffin waxes are most common and widely used. Matusuda et al. in [182] found that paraffin impregnation effectively prevents degradation of the HTS coil.

In this study, paraffin wax with a melting temperature of 55 °C was selected for impregnat-

ing the HTS magnet and charging coil due to its high latent heat values (145-240 kJ/kg) and chemical stability. The main challenge in using paraffin wax was its low thermal conductivity (below 0.1 W/m·K). To address this issue, ceramic fillers were added to enhance the thermal conductivity of the paraffin wax mixture. Aluminium Nitride (AlN) with particle size less than 10 microns was chosen as the ceramic filler due to its high thermal conductivity, excellent electrical insulation, low density, low thermal expansion, superior resistivity against thermal shock, and relative economy as reported by Badakhsh et al. in 2017 [183]. A concentration of fillers greater than 3% was found to improve the thermal conductivity by more than 18% and thermal responsivity by over 28% [184, 185]. This improved heat transfer from and to the paraffin wax allowed for the sample to be cooled down to 30 K. The mixture was prepared at 60 °C with continuous stirring, with a ratio of 10:1 between paraffin wax and aluminium nitride. After thorough mixing, the mixture was placed in a degassing chamber to eliminate any bubbles, as air pockets in the magnet could compromise its thermal conductivity. A sample after being impregnated with the paraffin wax mixture can be seen in Figure 6.7.

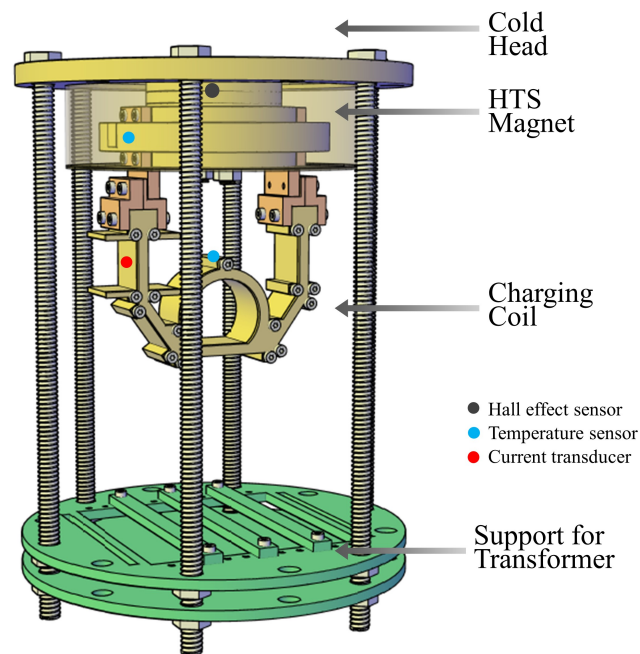


Figure 6.8: Schematic diagram of the final assembly of 30 K HTS flux pump.

6.3.4 Final assembly

The HTS magnet and charging coil are securely mounted into a specially designed frame fixture, which is customized to fit onto the cooling plate of the cryostat. The fixture is engineered with a sturdy support at the bottom to hold the transformer in place, allowing it to efficiently induce current into the secondary coil as illustrated in Figure 6.8. To facilitate precise measurement of the magnetic field of the transformer, the HTS magnet is preinstalled with a sensitive Hall effect sensor. The sample temperature is monitored using two temperature sensors from Lakeshore, one located on the magnet bridge and the other on the charging coil. Furthermore, to measure the induced current a current transducer has been incorporated into the design of the charging coil. Finally, the 30 K flux pump sample is securely installed on the cryostat, as demonstrated in Figure 6.9, completing the set-up process.

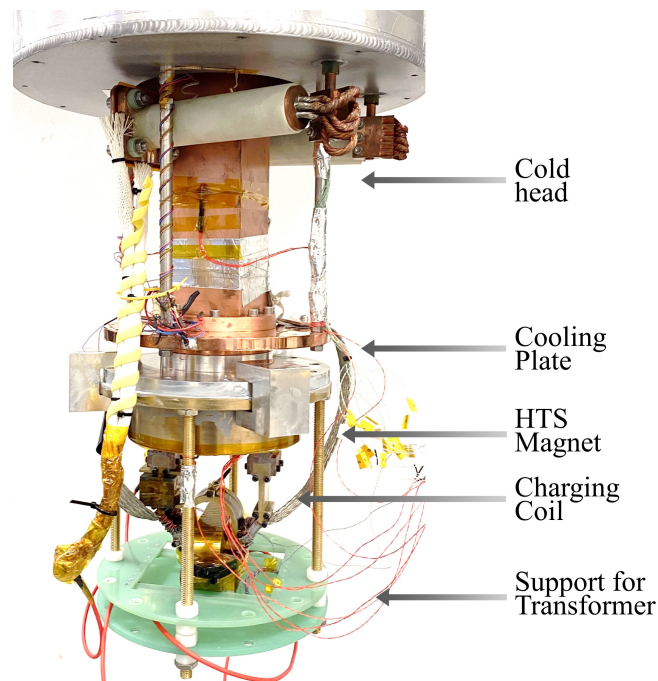


Figure 6.9: Image of HTS flux pump installed on cryostat cold head for operation at 30 K.

6.4 Experiment

The experiment's test bench was established using a methodology comparable to that presented in Section 4.4. The complete flux pump assembly, as illustrated in the previous section, was fully immersed in liquid nitrogen to facilitate testing at 77 K. Following that, the flux pump assembly underwent further testing at lower temperatures, reaching as low as 30 K. The recorded results for both temperature tests were analyzed and compared in later subsections to evaluate the performance of the flux pump.

6.4.1 Equivalent circuit model

The magnet and charging coil is designed with copper terminals to facilitate connection. The introduction of resistance through these terminals serves as a current-limiting resistor, which is denoted as R_{cu} in the system, which is $7E^{-5} \Omega$. The HTS-CC of the magnet is extended beyond the magnet terminals and soldered together to form a bifilar bridge. In this context, R_j

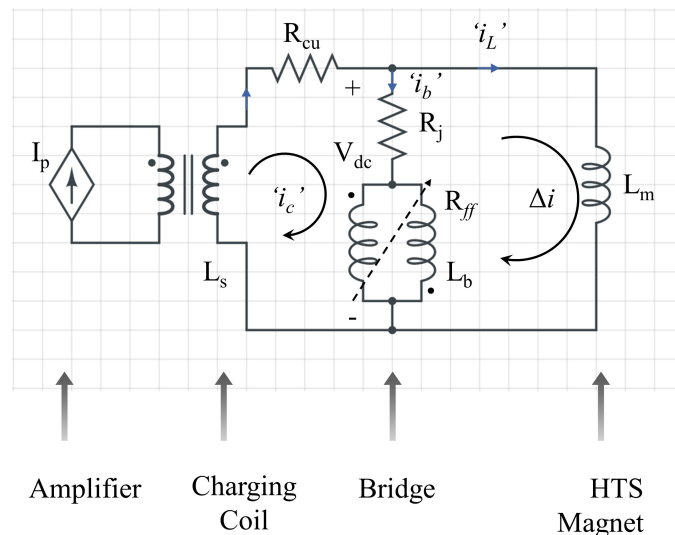
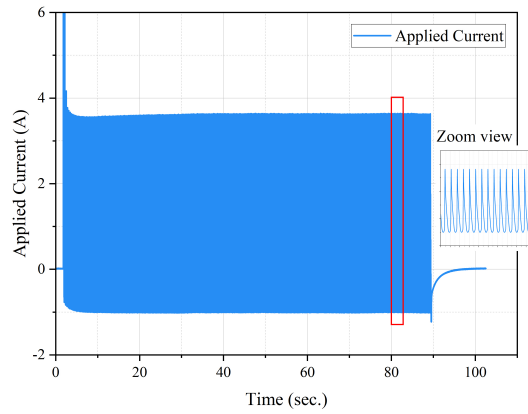


Figure 6.10: The equivalent circuit of the flux pump, which includes the charging coil, bifilar bridge, and magnet serving as the load coil.

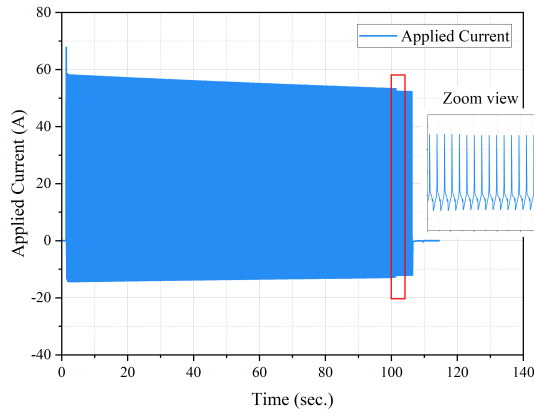
represents the soldering joint in the bridge which is $\sim 1E^{-5} \Omega$, R_{ff} represents the flux flow resistance of the bridge superconductor, and L_m represents the inductance of the HTS magnet. It is worth noting that since the bridge is constructed in a bifilar manner, it has negligible inductance.

6.4.2 Applied current

In this study, an asymmetric signal is utilized as the primary (input) current signal, as shown in Figure 4.14. The positive cycle of the signal involves a steady increase in current to reach the positive peak, followed by a decrease at the same rate to reach zero. Likewise, during the negative cycle, the current decreases to reach the negative peak, and then increases at the same rate to reach zero. The positive peak is maintained at a higher value to drive the superconductor into the flux flow region, enabling flux flow from the secondary side to the load side (magnet). On the other hand, the negative peak is kept much lower to retain the flux within the load. To eliminate the dc component, the length of the positive period is kept inversely proportional to the peak values of the negative period. The plot for the applied current is illustrated in Figure 6.11, and it is worth noting that the amplitude of the applied current at 77 K is significantly lower to induce only 400 A in the secondary side to ensure the bridge current goes over its critical current value. Whereas at 30 K, a significantly higher current is required to drive the superconductor into the flux flow region. The primary winding (copper) of the transformer has an input resistance of 1.1Ω and an inductance value of 110 mH. A power amplifier from AETECHRON 7796 5000 W [167], is employed to deliver a current of 60 A. The peak current of 60 A is applied for a brief duration in each cycle, as depicted in Chapter 4, Figure 4.14. Additionally, the copper leads connected to the primary winding of the transformer are immersed in LN_2 , significantly lowering their temperature and reducing resistivity compared to room temperature.



(a)



(b)

Figure 6.11: Applied current (i_p), (a) for flux pump operating at 77K, (b) for flux pump operating at 30 K.

6.4.3 Induced current in the secondary coil

The induce current in the charging coil can be calculated using the following equation presented below, which takes into account the circuit explanation presented in Section 6.4.1.

$$0 = \frac{d\phi}{dt} + L_s \frac{di_s}{dt} + i_s R_{cu} + i_b Z_b + i_b R_j, \quad (6.1)$$

The flux generated by the primary copper of the transformer is coupled with the high-temperature superconducting (HTS) charging coil. The charging current is denoted by i_s , and the inductance of the charging coil is represented by L_s . R_j is used to denote the joint

resistance, and Z_b represents the bridge impedance. Since the bridge inductance is negligible, the corresponding term can be approximated to zero. During the first cycle, the load current is zero, and thus, the current flowing through the bridge, represented by i_b , is equal to i_s . However, after the flux pumping action, the flux starts to accumulate in the magnet, and the DC current begins flowing through the bridge, resulting in a gradual increase in the charging current.

It is important to note that the critical current of HTS materials increases significantly as the temperature is lowered. For commercial HTS materials, the critical current increases by approximately 10% for each degree the temperature is lowered [186]. Furthermore, copper's resistivity changes with temperature [150, 151]. However, the change in copper's resistance is relatively small compared to the conductivity of the superconductor, as illustrated in Figure 6.12. The secondary/charging coil comprises two parallel HTS tapes of 12 mm width, with a total critical current of $I_c = 1000$ A at 77 K. To ensure that the bridge superconductor enters the flux flow region, the total critical current of the bridge is kept lower than that of the charging coil. The bridge is constructed using two HTS tapes of 4 mm width, with a total critical current of $I_c = 310$ A at 77 K. At 30 K, the critical current of the charging coil increases to 5700 A, while the total critical current of the bridge superconductor becomes

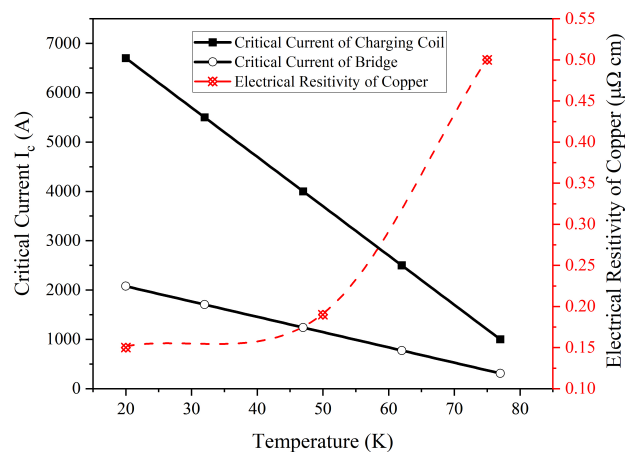
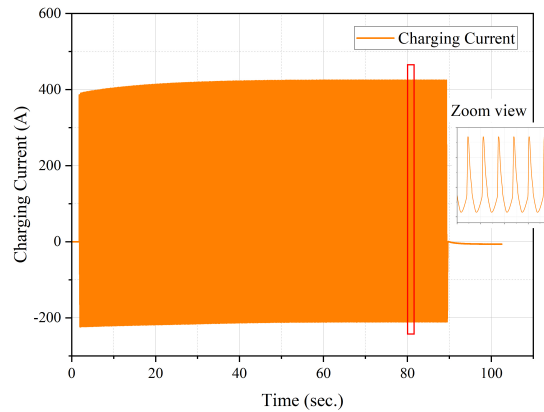
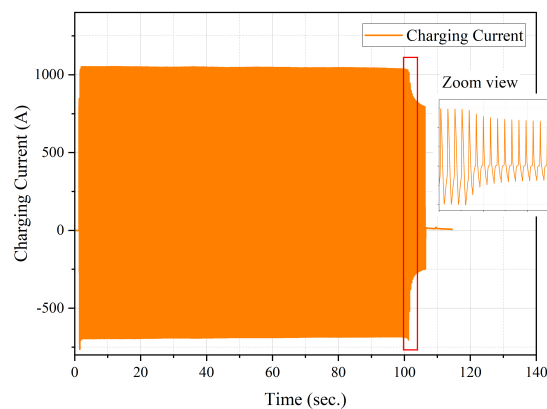


Figure 6.12: Temperature dependence of critical current for the charging coil and bridge, along with the variation of copper resistivity with temperature

1767 A, as determined using the criterion $E_0 = 10^{-4} \text{ V}\cdot\text{m}^{-1}$. Figure 6.13 illustrates the plot for the induced current in the charging coil. At 77 K, an applied current of 4 A can induce 400 A in the charging coil, whereas at 30 K, the charging current is limited to 1200 A. This limitation is due to the voltage induced in the secondary side, which limits the current in the charging coil. The high current flowing through the copper terminals generates heat, which results in an increase in temperature and a subsequent decrease in critical current. At 110 seconds, the charging coil quenches, further limiting the charging current. The temperature profile of the HTS magnet recorded at the bridge superconductor is presented in Figure 6.14. The temperature of the HTS magnet is maintained at 30 K, while the bridge superconductor



(a)



(b)

Figure 6.13: Induced current plot in the charging coil (i_s), (a) for flux pump operating at 77 K, (b) for flux pump operating at 30 K.

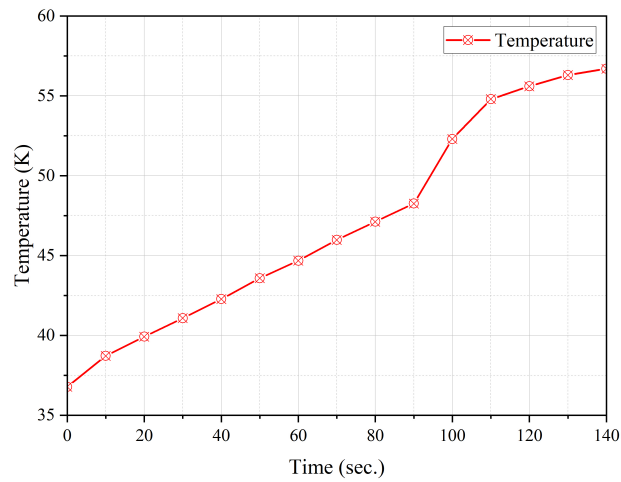


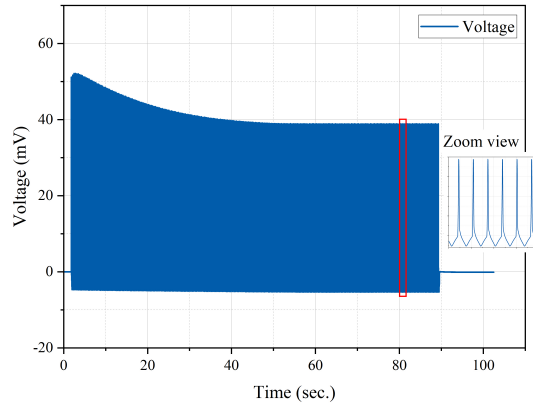
Figure 6.14: Temperature profile of the bridge superconductor for the flux pump operating at 30 K

operates at 36.5 K, and the charging coil at 40 K. The variation in temperature is attributed to the size and positioning of the components within the test setup. Specifically, the HTS magnet is closest and directly attached to the cold head cooling plate, followed by the bridge being sandwiched between the charging coil and the magnet. The charging coil, being the farthest component, creates this temperature gradient within the test setup. To achieve a temperature of 30 K, the cold head is kept on overnight for gradual cooling.

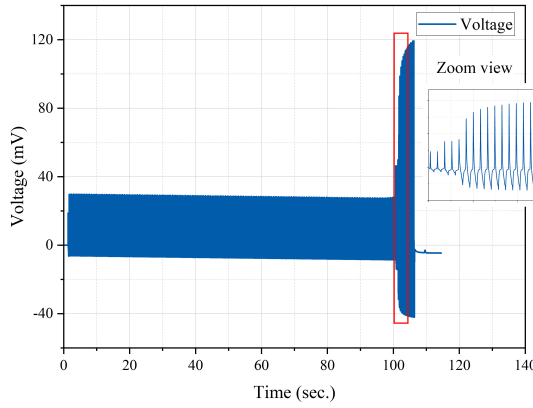
6.4.4 Voltage-current (V-I) of the bridge superconductor in the flux pump

In an ideal transformer, the secondary charging current (i_s) is always proportional to the primary current (i_p). However, in a real transformer, if the load impedance (Z_b) is high, the output voltage may reach its limit, causing the secondary current to limit the primary current. A transformer comprising of high-temperature superconductor (HTS) as its secondary, there is a voltage limit, which occurs when the current flowing through the HTS tape exceeds its critical value and causes it to quench. In this section, we will discuss the voltages induced across the bridge superconductor, the mathematical expression for dc voltages across the

Chapter 6. An HTS Flux Pump Operating at 30 K



(a)



(b)

Figure 6.15: The voltage measured (v_b) across the bridge, (a) for flux pump operating at 77 K, (b) for flux pump operating at 30 K.

bridge can be given as

$$V_{dc} = i_b R_j + i_b R_{ff} + L_b \frac{di_b}{dt} = L_m \frac{d\Delta i}{dt}, \quad (6.2)$$

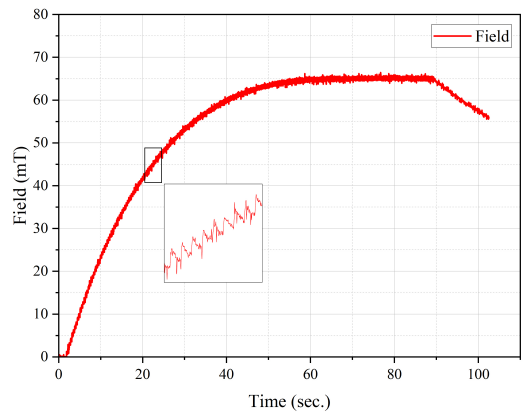
Where V_{dc} , is the dc voltages across the bridge, in (6.2) for a bifilar bridge the L_b is zero so the dc voltages V_{dc} across the bridge is purely due to flux flow resistivity R_{ff} .

During the initial charging cycle, the bridge current is equal to the charging current, and as the DC current accumulates in the magnet, the charging current becomes biased in one direction. As a result, the DC voltage drops as the load current increases. Figure 6.15a illustrates the

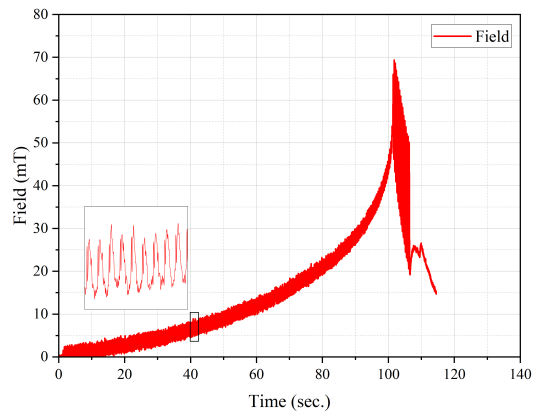
bridge voltage plot for a flux pump operating at 77 K. Conversely, if the primary current is too high, the bridge voltage reaches its maximum value and remains constant throughout the charging process. The load current increases nearly linearly at first, but eventually decreases as it approaches its critical current value. However, for a flux pump operating at 30 K, the temperature increases in every cycle, resulting in an exponential increase in load current before a quench occurs, as shown in Figure 6.15.

6.4.5 Flux injection into HTS magnet

Figure 6.16 shows the magnetic field plot of the coil magnets, which is important for understanding the flux pumping process. When the flux pump operates at 77 K, the bridge superconductor experiences a higher voltage, thanks to its lower critical current that enables it to enter the flux flow region. This induces higher voltages, leading to efficient charging of the magnet. Conversely, when the flux pump operates at 30 K, only a small dc voltage is available across the bridge superconductor due to the joint. However, this still causes flux pumping, as illustrated in Figure 6.16b. It is worth noting that the continuous injection of high charging current heats up the bridge, reducing its critical current, which is temperature-dependent. As a result, the rise in magnetic field follows an exponential plot before the bridge quenches. An important question arises concerning the need to avoid a massive heat load while charging the magnet without quenching the bridge. One potential solution is to use a lower frequency input signal, which can achieve the desired outcome. However, there are two key challenges with using a lower frequency signal. Firstly, the total resistance of the terminals and joints is large enough to dissipate the total flux injection in each cycle, which means that no flux accumulation took place at lower frequencies. Secondly, the power offered by the cold head is insufficient to cool down the flux pump, as shown in the capacity map illustrated in Figure 6.1.



(a)



(b)

Figure 6.16: The load's magnetic field measured at the center of the coil magnet for both cases, (a) for flux pump operating at 77 K, (b) for flux pump operating at 30 K.

6.5 Discussion

The self-switching high-temperature superconductor (HTS) flux pump has been identified as a promising method for charging magnets to high-current values (>1 kA), using a minimum geometry comprising of a single transformer as a source of flux. The bifilar bridge also enhances the field stability in the HTS magnet, which is critical for future all-electric propulsion systems that require higher magnetic fields compared to conventional permanent magnets.

However, one major challenge facing this technology is the ability to charge these persistent current HTS magnets. In our study, we demonstrated a promising solution to this

challenge by incorporating a flux pump. Specifically, our results showed that the flux pump can effectively inject flux into a closed-loop superconducting circuit at temperatures ranging from 77 K down to 30 K. However, we faced several challenges at lower temperatures, including the high input current required to drive the bridge in the flux flow region and the current limiting resistivity of the copper terminals. These challenges not only limit the charging current but also add heat to the bridge, which results in quenching after a few pumping cycles.

Despite these challenges, our study opens the door for further investigation and design considerations for future research on self-switching HTS flux pumps. While our self-rectifying flux pump at 30 K did not achieve the expected field value in the HTS magnet, our findings provide valuable insights into the limitations of this technology and suggest avenues for further exploration. Ultimately, our research contributes to the growing body of knowledge on HTS flux pumps and their potential applications in all-electric propulsion systems.

6.6 Conclusion

In this chapter, a compact high-temperature superconductor (HTS) magnet was designed to operate in a conduction-cooled environment at temperature below 77 K. The magnet incorporates a built-in bifilar bridge for charging using a flux pump and is capable of operating as a persistent current magnet. A detachable charging coil was provided as a wireless charger for the HTS magnet, and both the former for the HTS magnet and the charging coil were machined using oxygen-free brass to minimize thermal losses during cooling. Temperature measurements showed the HTS magnet to be at 30 K, while the charging coil and bridge were at 30 K. This temperature difference of 10 K was due to the large size of the flux pump relative to the cooling power of the cold head.

The flux pump was first operated at 77 K, and the results were recorded. The temperature was then lowered to 30 K to observe the performance of the flux pump. At both 77 K and 30 K, a magnetic field of 65 mT was successfully recorded at the center of the HTS magnet. The magnetic field anticipated at 30 K was much higher, but the rise in temperature of the bridge superconductor caused it to quench, and flux pumping actions ceased. To address this

issue, the copper terminals can be replaced with superconducting joints to avoid heating up the bridge superconductor and limiting the current induced in the charging coil. This is an important research topic that warrants further investigation. Another potential approach to sustaining injected current is to control the bridge temperature to generate voltage at lower temperatures and then rapidly cool it down to maintain the current. However, this would require a high power cold head or a helium-cooled chamber, which presents its own set of challenges. Despite the fact that the current in the HTS magnet presented in the chapter did not reach the anticipated level, the study effectively investigated key challenges associated with the method and demonstrated the viability of charging the HTS magnet using this method in a conduction-cooled environment.

7

Conclusion and Future Work

7.1 Introduction

This chapter presents the main findings and conclusions of the thesis, as well as the research contributions that were made. Additionally, recommendations for future research are provided at the end of the chapter.

7.2 Summary and conclusions

This thesis presents a thorough investigation into the design of a compact bifilar bridge coil, aiming to achieve stable voltages across the bridge superconductor for charging the HTS magnet using transformer rectifier flux pumps. Additionally, it introduces a closed-loop feedback technique for flux modulation in the HTS magnet. Furthermore, this research offers a unique perspective on magnet charging for applications operating at temperatures as low as 30 K using self rectifier HTS flux pump.

This thesis outlines a promising solution for achieving persistent current operation in HTS magnets for complex applications like fully superconducting motors, NMR, MRI, etc. It utilize a bifilar coil as a bridge to charge the HTS magnet using a transformer rectifier flux pump. Experimental results demonstrate the superiority of the bifilar bridge configuration,

which maintains stable peak voltages (103 mV) throughout the charging process, surpassing conventional HTS bridges. Moreover, the bifilar bridge enables the generation of a magnetic field of 35 mT, while the conventional bridge saturates at 25 mT with the same applied current. By eliminating the inductive component of the bridge, the bifilar configuration generates voltage solely through flux flow resistivity. This facilitates effective charging of the HTS load up to its critical current value.

Moreover, this thesis presents an effective control of the magnetic field in an HTS magnet via closed-loop feedback control technique. This not only modulates the field in the HTS magnet but also compensates for any decay in the field during operation, enabling a stable HTS magnet for high field application. The experimental results demonstrate the effectiveness of proposed control technique in inducing a precise voltage across the HTS bridge for effective flux modulation. Unlike traditional flux pumps that rely on the frequency and amplitude of the applied signal for pumping speed and do not control the voltage across the bridge, this technique allows for the injection/removal of a specific current of 0.5 A from the magnet on demand. By calculating the required voltage of 7 mV, the control block generates a corresponding current signal that drives the bridge into the flux flow regime and achieves the desired voltage needed to inject 0.5 A. This feedback-controlled flux pump is capable of precise flux modulation of HTS magnets in persistent current operation, overcoming technical challenges associated with high current power supplies and current leads while reducing the cooling requirements and footprint of HTS magnets.

Finally, it provides a practical demonstration of flux pumping at 30 K, which can be relevant to future all-electric propulsion systems that will be liquid hydrogen cooled. The magnet in this study incorporates a bifilar bridge for charging using a flux pump and can operate as a persistent current magnet. To minimize thermal losses during cooling, both the magnet former and the detachable charging coil were machined using oxygen-free brass. While the HTS magnet was found to be at 20 K, temperature measurements revealed that the charging coil and bridge were at 30 K due to the limited cooling power of the cold head relative to the size of the flux pump. The flux pump was successfully operated at 77 K and 30 K, recording a magnetic field of 65 mT at the center of the HTS magnet at both temperatures.

The anticipated magnetic field at 30 K was expected to be higher, the flux pumping actions were eventually ceased due to the superconductor in the bridge experiencing a temperature rise, resulting in quenching. To address this issue, the copper terminals can be replaced with least resistive $< \mu\Omega$ superconducting joints to avoid heating up the bridge superconductor and limiting the current induced in the charging coil and another potential approach to sustaining injected current is to control the bridge temperature to generate voltage at lower temperatures and then cool it down to maintain the current.

The results of this study provide new understanding and strategies for achieving stable magnetic fields in HTS magnets through the use of flux pumping. Additionally, the study highlights techniques for compensating for current decays in HTS magnets operating in persistent current mode. These findings might have significant implications for the development of high-field, low-cost HTS magnets, and represent a valuable contribution to the field of superconductivity research.

7.3 Future work

The results presented in this research provide a novel insight into achieving a stable magnetic field in HTS magnets via flux pumping and outline the methods to compensate for current decay in HTS magnets operating in the persistent current mode. Based on these findings, several recommendations can be proposed for those pursuing the development of HTS flux pumps.

A compact HTS permanent magnet design for fully superconducting motors

The permanent magnet in the rotor of fully superconducting machines currently acts as a bottleneck to magnetic loading. However, by utilizing HTS magnets, this limitation can be overcome. Traditional machines typically achieve a magnetic loading of approximately 1 T using rare-earth permanent magnets. In contrast, the use of 2G HTS tapes enables a significant increase in this value to 3 to 4 T. This elevated magnetic loading facilitates the implementation of coreless/air-core topology in superconducting machines, leading to higher

power and torque densities, as well as lighter weight machines.

The HTS magnet presented in this thesis comprises an integrated bifilar bridge, while the charging coil is detachable and separate from the magnet itself. Further study can focus on developing a complete package that integrates an HTS magnet, charging coil, and bridge in a compact geometry. This package can be installed in the rotor of fully superconducting machines without the need for any current leads entering the rotor.

Such advancements hold the potential to revolutionize the design and performance of superconducting machines.

Ultra precision flux modulation in HTS magnets

The HTS flux modulation presented in this thesis demonstrates the potential to achieve a resolution of less than $1E^{-5}$ A. It paves the way for further research and development of superconducting flux modulation techniques capable of precisely manipulating flux into and out of fully superconducting circuits with a resolution better than 10^{-4} A. It will offer a simple and effective solution for controlling magnetic flux motion in various superconducting electronic and sensor applications. Additionally, the ability to control flux with such precision in HTS magnets is essential for the development of superconducting controlled voltage sources, enabling output resolutions better than 10^{-14} V. Accomplishing this ambitious goal would have a profound impact on technology advancement and scientific research.

Scaling up the flux pump capability to charge 60 T HTS magnet

The bifilar bridge coil presented in this thesis can produce a predictable stable dc voltage, and it can be sized up to induce higher voltages to charge the large-scale HTS magnet. The primary objective of this research is to achieve a persistent current ranging from 2 kA to 20 kA within high-temperature superconducting (HTS) magnets that are enclosed. The results of this work could potentially have a profound impact on engineering practices. Currently, the National High Magnetic Field Lab (NHMFL) in Tallahassee, USA, is in the process of developing a 60 T HTS magnet that requires a large transport current [187]. It is worth noting that the larger the transport current, the smaller the magnet needs to be. However, the NHMFL has

encountered significant challenges due to the substantial transport current, which necessitates large current leads that consume a massive amount of energy and result in substantial losses. The proposed solution of using flux pumps has garnered interest, but numerous technological challenges must be addressed to achieve the desired outcome. These challenges include dealing with the substantial forces that arise between the superconductor and field magnet when a high current is generated, ensuring mechanical stability. Additionally, the significant losses on joints caused by the high transport current necessitate the development of low-loss joints [22, 188, 189]. Finally, achieving full penetration of the superconductor that has a high current capacity requires a demanding field strength. It is crucial to pay attention to these challenges as they are significant and require significant attention.

Superconducting rectifier

Flux pumps are often described as superconducting rectifiers that can only energize HTS magnets. However, extending this technology to achieve AC-DC conversion could have exciting implications for a range of applications, such as enabling the transfer of energy from offshore wind turbines to high-voltage DC cables (HVDC), or facilitating the delivery of energy out of cryogenic environments, such as Superconducting Magnetic Energy Storage (SMES) and magnets quench protections. This would represent a significant advancement, as it would allow for more efficient and reliable energy transfer across a wide range of systems. While further research and development is needed to explore the full potential of this technology, the possibilities it presents are certainly worthy of attention and investigation.

References

- [1] HG Khodzhibagiyan, NN Agapov, PG Akishin, NA Blinov, VV Borisov, AV Bychkov, AR Galimov, AM Donyagin, VN Karpinskiy, VS Korolev, et al. Superconducting magnets for the nica accelerator collider complex. *IEEE transactions on applied superconductivity*, 24(3):1–4, 2013.
- [2] Lucio Rossi. Superconducting magnets for the lhc main lattice. *IEEE transactions on applied superconductivity*, 14(2):153–158, 2004.
- [3] K Yokoyama, T Oka, H Okada, Y Fujine, A Chiba, and K Noto. Solid-liquid magnetic separation using bulk superconducting magnets. *IEEE Transactions on applied superconductivity*, 13(2):1592–1595, 2003.
- [4] Yuri Lvovsky, Ernst Wolfgang Stautner, and Tao Zhang. Novel technologies and configurations of superconducting magnets for mri. *Superconductor Science and Technology*, 26(9):093001, 2013.
- [5] V Corato, Tommaso Bagni, ME Biancolini, R Bonifetto, P Bruzzone, N Bykovsky, D Ciazynski, M Coleman, A Della Corte, A Dembkowska, et al. Progress in the design of the superconducting magnets for the eu demo. *Fusion engineering and design*, 136:1597–1604, 2018.
- [6] Masaru Tomita and Masato Murakami. High-temperature superconductor bulk magnets that can trap magnetic fields of over 17 tesla at 29 k. *Nature*, 421(6922):517–520, 2003.
- [7] John H Durrell, Anthony R Dennis, Jan Jaroszynski, Mark D Ainslie, Kysen GB Palmer, YH Shi, Archie M Campbell, John Hull, Mike Strasik, EE Hellstrom, et al. A trapped field of 17.6 T in melt-processed, bulk Gd-Ba-Cu-O reinforced with shrink-fit steel. *Superconductor Science and Technology*, 27(8):082001, 2014.

- [8] Anup Patel, Algirdas Baskys, Tom Mitchell-Williams, Aoife McCaul, William Coniglio, Jens Hänisch, Mayraluna Lao, and Bartek A Glowacki. A trapped field of 17.7 T in a stack of high temperature superconducting tape. *Superconductor Science and Technology*, 31(9):09LT01, 2018.
- [9] J Toth and ST Bole. Design, construction, and first testing of a 41.5 t all-resistive magnet at the nhmfl in tallahassee. *IEEE Transactions on Applied Superconductivity*, 28(3):1–4, 2017.
- [10] Y Iijima, N Kaneko, S Hanyu, Y Sutoh, K Kakimoto, S Ajimura, and T Saitoh. Development of ibad/pld process for long length y-123 conductors in fujikura. *Physica C: Superconductivity and its applications*, 445:509–514, 2006.
- [11] Herbert C Freyhardt. YBaCuO and REBaCuO HTS for applications. *International journal of applied ceramic technology*, 4(3):203–216, 2007.
- [12] Y Shiohara, M Yoshizumi, T Izumi, and Y Yamada. Present status and future prospect of coated conductor development and its application in japan. *Superconductor Science and Technology*, 21(3):034002, 2008.
- [13] M Sugano, K Osamura, W Prusseit, R Semerad, T Kuroda, K Itoh, and T Kiyoshi. Reversible strain dependence of critical current in 100 a class coated conductors. *IEEE transactions on applied superconductivity*, 15(2):3581–3584, 2005.
- [14] Jae-Hun Lee, Hunju Lee, Jung-Woo Lee, Soon-Mi Choi, Sang-Im Yoo, and Seung-Hyun Moon. Rce-dr, a novel process for coated conductor fabrication with high performance. *Superconductor Science and Technology*, 27(4):044018, 2014.
- [15] HW Weijers, UP Trociewitz, WD Markiewicz, J Jiang, D Myers, EE Hellstrom, A Xu, J Jaroszynski, P Noyes, Y Viouchkov, et al. High field magnets with HTS conductors. *IEEE transactions on applied superconductivity*, 20(3):576–582, 2010.
- [16] Yukikazu Iwasa. HTS magnets: stability; protection; cryogenics; economics; current stability/protection activities at FBML. *Cryogenics*, 43(3-5):303–316, 2003.

- [17] Benjamin J Parkinson, Robert Slade, Michael JD Mallett, and Vadim Chamritski. Development of a cryogen free 1.5 T YBCO HTS magnet for MRI. *IEEE transactions on applied superconductivity*, 23(3):4400405–4400405, 2012.
- [18] Rowan M Walsh, Robert Slade, Donald Pooke, and Christian Hoffmann. Characterization of current stability in an HTS NMR system energized by an HTS flux pump. *IEEE transactions on applied superconductivity*, 24(3):1–5, 2013.
- [19] Chang Young Lee, Jin Ho Lee, Jung Min Jo, Chan Bae Park, Won Hee Ryu, Yoon Do Chung, Young Jin Hwang, Tae Kuk Ko, Se-Young Oh, and Ju Lee. Conceptual design of superconducting linear synchronous motor for 600-km/h wheel-type railway. *IEEE transactions on applied superconductivity*, 24(3):1–4, 2013.
- [20] Y Jiang, R Pei, W Xian, Z Hong, and TA Coombs. The design, magnetization and control of a superconducting permanent magnet synchronous motor. *Superconductor Science and Technology*, 21(6):065011, 2008.
- [21] Hyung-Seop Shin, Ki-Hyun Kim, John Ryan C Dizon, Tae-Young Kim, Rock-Kil Ko, and Sang-Soo Oh. The strain effect on critical current in ybco coated conductors with different stabilizing layers. *Superconductor Science and Technology*, 18(12):S364, 2005.
- [22] Youngjae Kim, Juan Bascuñán, Thibault Lecrevisse, Seungyong Hahn, John Voccio, Dong Keun Park, and Yukikazu Iwasa. YBCO and Bi2223 coils for high field LTS/HTS NMR magnets: HTS-HTS joint resistivity. *IEEE Transactions on Applied Superconductivity*, 23(3):6800704–6800704, 2013.
- [23] Yeonjoo Park, Myungwhon Lee, Heesung Ann, Yoon Hyuck Choi, and Haigun Lee. A superconducting joint for $\text{GdBa}_2\text{Cu}_3\text{O}_{7-\delta}$ -coated conductors. *NPG Asia Materials*, 6(5):e98–e98, 2014.
- [24] Amalia Ballarino. Current leads, links and buses. *arXiv preprint arXiv:1501.07166*, 2015.

- [25] LJM Van de Klundert and Herman HJ ten Kate. Fully superconducting rectifiers and fluxpumps part 1: Realized methods for pumping flux. *Cryogenics*, 21(4):195–206, 1981.
- [26] LJM Van De Klundert and HHJ Ten Kate. On fully superconducting rectifiers and flux-pumps. a review. part 2: Commutation modes, characteristics and switches. *Cryogenics*, 21(5):267–277, 1981.
- [27] Marijn P Oomen, Martino Leghissa, Guenter Ries, Norbert Proelss, H-W Neumueller, Florian Steinmeyer, Markus Vester, and Frank Davies. HTS flux pump for cryogen-free HTS magnets. *IEEE transactions on applied superconductivity*, 15(2):1465–1468, 2005.
- [28] Sasha Ishmael, Carl Goodzeit, Philippe Masson, Rainer Meinke, and Robert Sullivan. Flux pump excited double-helix rotor for use in synchronous machines. *IEEE transactions on applied superconductivity*, 18(2):693–696, 2008.
- [29] Jianzhao Geng and TA Coombs. Mechanism of a high-Tc superconducting flux pump: Using alternating magnetic field to trigger flux flow. *Applied Physics Letters*, 107(14):142601, 2015.
- [30] Jianzhao Geng, K Matsuda, Lin Fu, Boyang Shen, Xiuchang Zhang, and TA Coombs. Operational research on a high-Tc rectifier-type superconducting flux pump. *Superconductor Science and Technology*, 29(3):035015, 2016.
- [31] YD Chung, Itsuya Muta, Tsutomu Hoshino, Taketsune Nakamura, and MH Shon. Design and performance of compensator for decremental persistent current in HTS magnets using linear type magnetic flux pump. *Cryogenics*, 44(11):839–844, 2004.
- [32] Zhiming Bai, Guo Yan, Chunli Wu, Shufang Ding, and Chuan Chen. A novel high temperature superconducting magnetic flux pump for MRI magnets. *Cryogenics*, 50(10):688–692, 2010.

- [33] Lin Fu, Koichi Matsuda, and Tim Coombs. Linear flux pump device applied to HTS magnets: further characteristics on wave profile, number of poles, and control of saturated current. *IEEE Transactions on Applied Superconductivity*, 26(3):1–4, 2016.
- [34] Christian Hoffmann, Donald Pooke, and A David Caplin. Flux pump for HTS magnets. *IEEE Transactions on Applied Superconductivity*, 21(3):1628–1631, 2010.
- [35] TA Coombs, Jean-François Fagnard, and Koichi Matsuda. Magnetization of 2-g coils and artificial bulks. *IEEE Transactions on Applied Superconductivity*, 24(5):1–5, 2014.
- [36] Zhenan Jiang, K Hamilton, Naoyuki Amemiya, RA Badcock, and CW Bumby. Dynamic resistance of a high-Tc superconducting flux pump. *Applied Physics Letters*, 105(11):112601, 2014.
- [37] CW Bumby, Zhenan Jiang, JG Storey, AE Pantoja, and RA Badcock. Anomalous open-circuit voltage from a high-Tc superconducting dynamo. *Applied Physics Letters*, 108(12):122601, 2016.
- [38] Walther Meissner and Robert Ochsenfeld. Ein neuer effekt bei eintritt der supraleitfähigkeit. *Naturwissenschaften*, 21(44):787–788, 1933.
- [39] Pia Jensen Ray. *Structural investigation of $La_{2-x}Sr_xCuO_{4+y}$* . PhD thesis, Master’s thesis (University of Copenhagen, 2015), 2015.
- [40] J George Bednorz and K Alex Müller. Possible high Tc superconductivity in the Ba-La-Cu-O system. *Zeitschrift für Physik B Condensed Matter*, 64(2):189–193, 1986.
- [41] Werner Buckel and Reinhold Kleiner. *Superconductivity: fundamentals and applications*. John Wiley & Sons, 2008.
- [42] NE Alekseevskii and IP GAIDUKOV. The effect of pressure on the superconductivity of cadmium. *SOVIET PHYSICS JETP-USSR*, 2(4):762–764, 1956.
- [43] David Larbalestier, Alex Gurevich, D Matthew Feldmann, and Anatoly Polyanskii. High-tc superconducting materials for electric power applications. In *Materials For*

- Sustainable Energy: A Collection of Peer-Reviewed Research and Review Articles from Nature Publishing Group*, pages 311–320. World Scientific, 2011.
- [44] Lev Davidovich Landau. *Collected papers of LD Landau*. Pergamon, 1965.
- [45] Charles P Poole, Horacio A Farach, and Prozorov Ruslan Creswick, Richard J. *Superconductivity Second Edition*. Academic press, 2007.
- [46] John Bardeen, Leon N Cooper, and John Robert Schrieffer. Theory of superconductivity. *Physical review*, 108(5):1175, 1957.
- [47] Alexei Alexeyevich Abrikosov. The magnetic properties of superconducting alloys. *Journal of Physics and Chemistry of Solids*, 2(3):199–208, 1957.
- [48] Günter Fuchs, Wolf-Rüdiger Canders, Hardo May, Ryszard Palka, and Gernot Krabbes. *High Temperature Superconductor Bulk Materials: Fundamentals, Processing, Properties Control, Application Aspects*. John Wiley & Sons, 2006.
- [49] Charles P Poole, Horacio A Farach, and Richard J Creswick. *Superconductivity Third Edition*. Elsevier, 2014.
- [50] CP Poole Jr and HA Farach. R, j. creswick, superconductivity, 1996.
- [51] BM Vlcek, MC Frischherz, S Fleshler, U Welp, JZ Liu, J Downey, KG Vandervoort, GW Crabtree, MA Kirk, John Giapintzakis, et al. Flux pinning in $\text{YBa}_2\text{Cu}_3\text{O}_{7-\delta}$ single crystals: Neutron irradiation and annealing. *Physical Review B*, 46(10):6441, 1992.
- [52] EM Chudnovsky. Pinning by oxygen vacancies in high-Tc superconductors. *Physical review letters*, 65(24):3060, 1990.
- [53] David R Nelson and VM Vinokur. Boson localization and pinning by correlated disorder in high-temperature superconductors. *Physical review letters*, 68(15):2398, 1992.

- [54] K Harada, T Matsuda, J Bonevich, M Igarashi, S Kondo, G Pozzi, U Kawabe, and A Tonomura. Real-time observation of vortex lattices in a superconductor by electron microscopy. *Nature*, 360(6399):51–53, 1992.
- [55] K Kakimoto, M Igarashi, S Hanyu, Y Sutoh, T Takemoto, T Hayashida, Y Hanada, N Nakamura, R Kikutake, H Kutami, et al. Long RE123 coated conductors with high critical current over 500 A/cm by IBAD/PLD technique. *Physica C: Superconductivity and its Applications*, 471(21-22):929–931, 2011.
- [56] M Dürschnabel, Z Aabdin, M Bauer, R Semerad, W Prusseit, and O Eibl. DyBa₂Cu₃O_{7-x} superconducting coated conductors with critical currents exceeding 1000 A cm⁻¹. *Superconductor Science and Technology*, 25(10):105007, 2012.
- [57] Cristina Buzea and Tsutomu Yamashita. Review of the superconducting properties of MgB₂. *Superconductor Science and Technology*, 14(11):R115, 2001.
- [58] Kenji Kawano, JS Abell, M Kambara, N Hari Babu, and DA Cardwell. Evidence for high intergranular current flow in a single-phase polycrystalline MgB₂ superconductor. *Applied Physics Letters*, 79(14):2216–2218, 2001.
- [59] Giovanni Giunchi. High density MgB₂ obtained by reactive liquid Mg infiltration. *International Journal of Modern Physics B*, 17(04n06):453–460, 2003.
- [60] Simone Sprio, Anna Tampieri, Gian Carlo Celotti, and D Rinaldi. Densification behaviour of MgB₂ superconductor by hot-pressing. In *Key Engineering Materials*, volume 264, pages 1201–1204. Trans Tech Publ, 2004.
- [61] G Giunchi, E Perini, T Cavallin, E Bassani, R Quarantiello, V Cavaliere, and A Matrone. Superconducting permanent magnet made by a bulk MgB₂ ring. *IEEE transactions on applied superconductivity*, 18(2):1216–1219, 2008.
- [62] Hiroyuki Fujishiro, Takuya Tamura, Takahiro Arayashiki, Mitsuru Oyama, Tomohisa Sasaki, Tomoyuki Naito, Giovanni Giunchi, and Alessandro Figini Albisetti. Pulsed

- field magnetization of large MgB₂ bulk fabricated by reactive liquid Mg infiltration. *Japanese Journal of Applied Physics*, 51(10R):103005, 2012.
- [63] Giovanni Giunchi, Giovanni Ripamonti, Tommaso Cavallin, and Enrico Bassani. The reactive liquid mg infiltration process to produce large superconducting bulk MgB₂ manufacts. *Cryogenics*, 46(2-3):237–242, 2006.
- [64] JH Durrell, CEJ Dancer, A Dennis, Y Shi, Z Xu, AM Campbell, N Hari Babu, RI Todd, CRM Grovenor, and DA Cardwell. A trapped field of > 3 T in bulk MgB₂ fabricated by uniaxial hot pressing. *Superconductor Science and Technology*, 25(11):112002, 2012.
- [65] Philip W Anderson and YB Kim. Hard superconductivity: theory of the motion of abrikosov flux lines. *Reviews of modern physics*, 36(1):39, 1964.
- [66] Charles P Bean. Magnetization of high-field superconductors. *Reviews of modern physics*, 36(1):31, 1964.
- [67] YoB Kim, CF Hempstead, and AR Strnad. Magnetization and critical supercurrents. *Physical Review*, 129(2):528, 1963.
- [68] YB Kim, CF Hempstead, and AR Strnad. Critical persistent currents in hard superconductors. *Physical Review Letters*, 9(7):306, 1962.
- [69] AP Malozemoff. Flux creep in high temperature superconductors. *Physica C: Superconductivity*, 185:264–269, 1991.
- [70] William Geraint Vaughan Rosser. An introduction to the theory of relativity. 1964.
- [71] John Bardeen and MJ Stephen. Theory of the motion of vortices in superconductors. *Physical Review*, 140(4A):A1197, 1965.
- [72] Alan T Dorsey. Vortex motion and the hall effect in type-II superconductors: A time-dependent Ginzburg-Landau theory approach. *Physical Review B*, 46(13):8376, 1992.

- [73] NB Kopnin and AV Lopatin. Flux-flow hall effect in clean type-II superconductors. *Physical Review B*, 51(21):15291, 1995.
- [74] Nikolai B Kopnin. Vortex dynamics and mutual friction in superconductors and fermi superfluids. *Reports on Progress in Physics*, 65(11):1633, 2002.
- [75] MR Beasley, R Labusch, and WW Webb. Flux creep in type-II superconductors. *Physical Review*, 181(2):682, 1969.
- [76] Philip W Anderson. Theory of flux creep in hard superconductors. *Physical Review Letters*, 9(7):309, 1962.
- [77] Yun Luo, Toshiyuki Takagi, and Kenzo Miya. Reduction of levitation decay in high Tc superconducting magnetic bearings. *Cryogenics*, 39(4):331–338, 1999.
- [78] Yoshikatsu Yoshida, Mitsuru Uesaka, and Kenzo Miya. Magnetic field and force analysis of high Tc superconductor with flux flow and creep. *IEEE transactions on magnetics*, 30(5):3503–3506, 1994.
- [79] P Kovac, V Cambel, and P Bukva. Measuring the homogeneity of Bi(2223)/Ag tapes by four-probe method and a hall probe array. *Superconductor Science and Technology*, 12(7):465, 1999.
- [80] A Gladun, G Fuchs, K Fischer, D Busch, R Eujen, and J Huedepohl. Critical current densities and activation energy of BiPbSrCaCuO tapes. *IEEE transactions on applied superconductivity*, 3(1):1390–1393, 1993.
- [81] L Civale, B Maiorov, A Serquis, JO Willis, JY Coulter, H Wang, QX Jia, PN Arendt, JL ab MacManus-Driscoll, MPa Maley, et al. Angular-dependent vortex pinning mechanisms in $\text{YBa}_2\text{Cu}_3\text{O}_7$ coated conductors and thin films. *Applied physics letters*, 84(12):2121–2123, 2004.
- [82] WJ Carr Jr. *AC loss and macroscopic theory of superconductors*. CRC press, 2001.

- [83] Shigehisa Kusada, Motohiro Igarashi, Kaoru Nemoto, Takeshi Okutomi, Satoshi Hirano, Katsuyuki Kuwano, Takaya Tominaga, Motoaki Terai, Toru Kuriyama, Kenji Tasaki, et al. The project overview of the HTS magnet for superconducting Maglev. *IEEE Transactions on Applied Superconductivity*, 17(2):2111–2116, 2007.
- [84] Felipe Sass, Guilherme Gonçalves Sotelo, Alexander Polasek, and Rubens de Andrade. Application of 2G-tape for passive and controlled superconducting levitation. *IEEE transactions on applied superconductivity*, 21(3):1511–1514, 2011.
- [85] Kenji Tasaki, Kotaro Marukawa, Satoshi Hanai, Taizo Tosaka, Toru Kuriyama, Tomohisa Yamashita, Yasuto Yanase, Mutsuhiko Yamaji, Hiroyuki Nakao, Motohiro Igarashi, et al. HTS magnet for Maglev applications (1)—Coil characteristics. *IEEE transactions on applied superconductivity*, 16(2):1100–1103, 2006.
- [86] Seungyong Hahn, Dong Keun Park, John Voccio, Juan Bascuñán, and Yukikazu Iwasa. No-insulation (NI) HTS inserts for >1 GHz LTS/HTS NMR magnets. *Ieee transactions on applied superconductivity*, 22(3):4302405–4302405, 2011.
- [87] W Denis Markiewicz, John R Miller, Justin Schwartz, Ulf P Trociewitz, and Huub W Weijers. Perspective on a superconducting 30 T/1.3 GHz NMR spectrometer magnet. *IEEE Transactions on applied superconductivity*, 16(2):1523–1526, 2006.
- [88] Seungyong Hahn, Kwanglok Kim, Kwangmin Kim, Xinbo Hu, Thomas Painter, Iain Dixon, Seokho Kim, Kabindra R Bhattarai, So Noguchi, Jan Jaroszynski, et al. 45.5-tesla direct-current magnetic field generated with a high-temperature superconducting magnet. *Nature*, 570(7762):496–499, 2019.
- [89] Siyuan Liu, Xiaohua Jiang, Guolin Chai, and Jiangbo Chen. Superconducting joint and persistent current switch for a 7-T animal MRI magnet. *IEEE transactions on applied superconductivity*, 23(3):4400504–4400504, 2012.
- [90] K Nemoto, S Saito, Y Sanada, K Sasaki, S Miyake, and H Hashiguchi. Niobium-tin

- persistent-current switch for the superconducting magnet of Maglev. *IEEE transactions on applied superconductivity*, 9(2):181–184, 1999.
- [91] TK Ko, YS Oh, and SJ Lee. Optimal design of the superconducting persistent current switch with respect to the heater currents and the operating currents. *IEEE Transactions on Applied Superconductivity*, 5(2):262–265, 1995.
- [92] Jianhua Liu, Junsheng Cheng, Feng Zhou, Qiuliang Wang, Kun Chang, and Xian Li. Electrical properties of cold-pressing welded NbTi persistent joints. *Cryogenics*, 58:62–67, 2013.
- [93] GD Brittles, T Mousavi, CRM Grovenor, C Aksoy, and SC Speller. Persistent current joints between technological superconductors. *Superconductor Science and Technology*, 28(9):093001, 2015.
- [94] SuperPower Inc. super power 2012, “www.superpower-inc.com/Technology.aspx”: date accessed 2023/04/26.
- [95] Young Gun Park, Chang Young Lee, Jiho Lee, Seokho Nam, Yoon Do Chung, Yong Soo Yoon, and Tae Kuk Ko. Experimental analysis on initial current decay characteristics of persistent-mode HTS coil by external alternating magnetic field. *IEEE Transactions on Applied Superconductivity*, 25(3):1–4, 2014.
- [96] Young Gun Park, Woo Seung Lee, Jeyull Lee, Seunghyun Song, Young Jin Hwang, Yoon Do Chung, and Tae Kuk Ko. Operational characteristics of HTS coils with flux diverters in semipersistent mode under alternating magnetic field. *IEEE Transactions on Applied Superconductivity*, 26(4):1–5, 2016.
- [97] J Geng, H Zhang, C Li, X Zhang, B Shen, and TA Coombs. Angular dependence of direct current decay in a closed ybco double-pancake coil under external ac magnetic field and reduction by magnetic shielding. *Superconductor Science and Technology*, 30(3):035022, 2017.

- [98] Andres E Pantoja, Zhenan Jiang, Rodney A Badcock, and Chris W Bumby. Impact of stator wire width on output of a dynamo-type HTS flux pump. *IEEE Transactions on Applied Superconductivity*, 26(8):1–8, 2016.
- [99] Kent Hamilton, Andres E Pantoja, James G Storey, Zhenan Jiang, Rodney A Badcock, and Chris W Bumby. Design and performance of a “squirrel-cage” dynamo-type HTS flux pump. *IEEE Transactions on Applied Superconductivity*, 28(4):1–5, 2018.
- [100] Kent Hamilton, Andres E Pantoja, James G Storey, Zhenan Jiang, Rodney A Badcock, and Chris W Bumby. Asynchronous magnet–stator topologies in a squirrel-cage superconducting dynamo. *IEEE Transactions on Applied Superconductivity*, 29(5):1–5, 2019.
- [101] Wei Wang, Yong Lei, Shuqian Huang, Peng Wang, Zhen Huang, and Qun Zhou. Charging 2G HTS double pancake coils with a wireless superconducting dc power supply for persistent current operation. *IEEE Transactions on Applied Superconductivity*, 28(3):1–4, 2018.
- [102] Yuntian Zhang, Wei Wang, Hanxin Ye, Xueqing Wang, Yunfei Gao, Qun Zhou, Xueshan Liu, and Yong Lei. Compact linear-motor type flux pumps with different wavelengths for high-temperature superconducting magnets. *IEEE Transactions on Applied Superconductivity*, 30(4):1–5, 2020.
- [103] Wei Wang, Chao Yang, Hang Xu, Hanxin Ye, Zhenxuan Yang, Hong Li, Jiafu Wei, Yingwei Zhu, Chenghuai Wu, Run Long, et al. A kilo-amp linear-motor type flux pump. *IEEE Transactions on Applied Superconductivity*, 32(6):1–5, 2022.
- [104] Yunfei Gao, Wei Wang, Xueqing Wang, Shuqian Huang, Yong Lei, Xueshan Liu, and Qun Zhou. Design and study of a 2G HTS synchronous motor with brushless HTS flux pump exciters. *IEEE Transactions on Applied Superconductivity*, 29(5):1–5, 2019.
- [105] Hong Li, Wei Wang, Xiaojun Niu, Jun Zheng, Yunfei Gao, Hanxin Ye, Yuntian Zhang, Jiafu Wei, Hang Xu, Boyang Shen, et al. Charging optimization of a YBCO

- racetrack coil with a linear-motor type flux pump for an HTS synchronous motor. *IEEE Transactions on Applied Superconductivity*, 31(8):1–5, 2021.
- [106] Jianzhao Geng, K Matsuda, L Fu, Jean-François Fagnard, Hong Zhang, X Zhang, Boyang Shen, Q Dong, M Baghdadi, and TA Coombs. Origin of dc voltage in type-II superconducting flux pumps: field, field rate of change, and current density dependence of resistivity. *Journal of Physics D: Applied Physics*, 49(11):11LT01, 2016.
- [107] Timothy Coombs, Zhiyong Hong, and Xiaomin Zhu. A thermally actuated superconducting flux pump. *Physica C: Superconductivity*, 468(3):153–159, 2008.
- [108] Yu Yan, Quan Li, and TA Coombs. Thermally actuated magnetization flux pump in single-grain YBCO bulk. *Superconductor Science and Technology*, 22(10):105011, 2009.
- [109] TA Coombs, Z Hong, Y Yan, and CD Rawlings. The next generation of superconducting permanent magnets: The flux pumping method. *IEEE transactions on applied superconductivity*, 19(3):2169–2173, 2009.
- [110] MP Oomen, J Rieger, M Leghissa, Bernard ten Haken, and Herman HJ ten Kate. Dynamic resistance in a slab-like superconductor with $J_c(B)$ dependence. *Superconductor science and technology*, 12(6):382, 1999.
- [111] Zhenan Jiang, Wei Zhou, Quan Li, Min Yao, Jin Fang, Naoyuki Amemiya, and Chris W Bumby. The dynamic resistance of YBCO coated conductor wire: Effect of DC current magnitude and applied field orientation. *Superconductor Science and Technology*, 31(3):035002, 2018.
- [112] Zhenan Jiang, Ryuki Toyomoto, Naoyuki Amemiya, Xingyou Zhang, and Chris W Bumby. Dynamic resistance of a high- T_c coated conductor wire in a perpendicular magnetic field at 77 K. *Superconductor Science and Technology*, 30(3):03LT01, 2017.

- [113] Jianzhao Geng, Tom Painter, Peter Long, Jamie Gawith, Jiabin Yang, Jun Ma, Qihuan Dong, Boyang Shen, Chao Li, and TA Coombs. A kilo-ampere level HTS flux pump. *Superconductor Science and Technology*, 32(7):074004, 2019.
- [114] Bradley Leuw, Jianzhao Geng, James HP Rice, Dominic A Moseley, and Rodney A Badcock. A half-wave superconducting transformer-rectifier flux pump using $J_c(B)$ switches. *Superconductor Science and Technology*, 35(3):035009, 2022.
- [115] Sriharsha Venuturumilli, Jianzhao Geng, Bradley Leuw, Chris Bumby, and Rod Badcock. Modelling of various rectifier flux pump topologies enabled by $J_c(B)$ switches. In *7th International Workshop on Numerical Modelling of High Temperature Superconductors*, 2021.
- [116] Jianzhao Geng and TA Coombs. An HTS flux pump operated by directly driving a superconductor into flux flow region in the E–J curve. *Superconductor Science and Technology*, 29(9):095004, 2016.
- [117] Jianzhao Geng, Chris W Bumby, and Rodney A Badcock. Maximising the current output from a self-switching kA-class rectifier flux pump. *Superconductor Science and Technology*, 33(4):045005, 2020.
- [118] Pengbo Zhou, Guangtong Ma, Yuke Deng, Xingchao Nie, Yao Zhai, Kang Liu, Han Zhang, and Yongjian Li. A contactless self-regulating HTS flux pump. *IEEE Transactions on Applied Superconductivity*, 30(4):1–6, 2020.
- [119] Wei Wang, Jiafu Wei, Chao Yang, Chenghuai Wu, and Hong Li. Review of high temperature superconducting flux pumps. *Superconductivity*, page 100022, 2022.
- [120] C Hoffmann, R Walsh, E Karrer-Mueller, and D Pooke. Design parameters for an HTS flux pump. *Physics Procedia*, 36:1324–1329, 2012.
- [121] Zhenan Jiang, Chris W Bumby, Rodney A Badcock, Hae-Jin Sung, Nicholas J Long, and Naoyuki Amemiya. Impact of flux gap upon dynamic resistance of a rotating HTS flux pump. *Superconductor Science and Technology*, 28(11):115008, 2015.

- [122] Chris W Bumby, Sinhoi Phang, Andres E Pantoja, Zhenan Jiang, James G Storey, Hae-Jin Sung, Minwon Park, and Rodney A Badcock. Frequency dependent behavior of a dynamo-type HTS flux pump. *IEEE Transactions on Applied Superconductivity*, 27(4):1–5, 2016.
- [123] Rodney A Badcock, Sinhoi Phang, Andres E Pantoja, Zhenan Jiang, James G Storey, Hae-Jin Sung, Minwon Park, and Chris W Bumby. Impact of magnet geometry on output of a dynamo-type HTS flux pump. *IEEE Transactions on Applied Superconductivity*, 27(4):1–5, 2016.
- [124] Chris W Bumby, Andres E Pantoja, Hae-Jin Sung, Zhenan Jiang, Ravi Kulkarni, and Rodney A Badcock. Through-wall excitation of a magnet coil by an external-rotor HTS flux pump. *IEEE Transactions on Applied Superconductivity*, 26(4):1–5, 2016.
- [125] Zhiming Bai, Shufang Ding, Chao Li, Chengshan Li, and Guo Yan. A newly developed pulse-type microampere magnetic flux pump. *IEEE Transactions on Applied Superconductivity*, 20(3):1667–1670, 2010.
- [126] Zhiming Bai, Chuan Chen, Yanqing Wu, and Zhen Zhen. Effect of various pulse wave forms for pulse-type magnetic flux pump. *Cryogenics*, 51(9):530–533, 2011.
- [127] Lin Fu, Koichi Matsuda, Mehdi Baghdadi, and Tim Coombs. Linear flux pump device applied to high temperature superconducting (HTS) magnets. *IEEE Transactions on Applied Superconductivity*, 25(3):1–4, 2015.
- [128] T Ogasawara, K Yasuköchi, S Nose, and H Sekizawa. Effective resistance of current-carrying superconducting wire in oscillating magnetic fields 1: Single core composite conductor. *Cryogenics*, 16(1):33–38, 1976.
- [129] A Uksusman, Y Wolfus, A Friedman, A Shaulov, and Y Yeshurun. Voltage response of current carrying Y–Ba–Cu–O tapes to alternating magnetic fields. *Journal of Applied Physics*, 105(9):093921, 2009.

- [130] Grigori P Mikitik and Ernst Helmut Brandt. Generation of a dc voltage by an ac magnetic field in type-II superconductors. *Physical Review B*, 64(9):092502, 2001.
- [131] H.L. Laquer, K.J. Carroll, and E.F. Hammel. An automatic superconducting flux pump* *work performed under the auspices of the U.S. atomic energy commission. In *Liquid Helium Technology*, volume 6 of *Pure and Applied Cryogenics*, pages 539–544. Elsevier, 1966.
- [132] Yukikazu Iwasa. Microampere flux pumps for superconducting NMR magnets part 1: basic concept and microtesla flux measurement. *Cryogenics*, 41(5-6):385–391, 2001.
- [133] Sangkwon Jeong, H Lee, and Y Iwasa. Superconducting flux pump for high-temperature superconductor insert coils of nmr magnets. In *AIP Conference Proceedings*, volume 613, pages 441–448. American Institute of Physics, 2002.
- [134] TA Coombs. Superconducting flux pumps. *Journal of Applied Physics*, 125(23):230902, 2019.
- [135] I Giaever. A dc transformer. *IEEE spectrum*, 3(9):117–122, 1966.
- [136] Mark D Ainslie, Weijia Yuan, Zhiyong Hong, Ruilin Pei, Tim J Flack, and Tim A Coombs. Modeling and electrical measurement of transport AC loss in HTS-based superconducting coils for electric machines. *IEEE transactions on applied superconductivity*, 21(3):3265–3268, 2010.
- [137] Z Hong, AM Campbell, and TA Coombs. Numerical solution of critical state in superconductivity by finite element software. *Superconductor Science and Technology*, 19(12):1246, 2006.
- [138] G Barnes, M McCulloch, and D Dew-Hughes. Computer modelling of type II superconductors in applications. *Superconductor Science and Technology*, 12(8):518, 1999.

- [139] TA Coombs, AM Campbell, A Murphy, and M Emmens. A fast algorithm for calculating the critical state in superconductors. *COMPEL-The international journal for computation and mathematics in electrical and electronic engineering*, 20(1):240–252, 2001.
- [140] Naoyuki Amemiya, Shun-ichi Murasawa, Nobuya Banno, and Kengo Miyamoto. Numerical modelings of superconducting wires for AC loss calculations. *Physica C: Superconductivity*, 310(1-4):16–29, 1998.
- [141] G Meunier, YLe FLOCH, and C Guerin. A nonlinear circuit coupled computation of coupled problem 3D eddy current and electrical circuit by using ϕ -T T₀ formulation for solid conductors. *IEEE Transactions on Magnetics*, 39(3 part 1):1729–1732, 2003.
- [142] Roberto Brambilla, Francesco Grilli, and Luciano Martini. Development of an edge-element model for ac loss computation of high-temperature superconductors. *Superconductor Science and Technology*, 20(1):16, 2006.
- [143] Ph Vanderbemden, Z Hong, TA Coombs, Samuel Denis, Marcel Ausloos, J Schwartz, IB Rutel, N Hari Babu, DA Cardwell, and AM Campbell. Behavior of bulk high-temperature superconductors of finite thickness subjected to crossed magnetic fields: Experiment and model. *Physical Review B*, 75(17):174515, 2007.
- [144] Mark D Ainslie, Victor M Rodriguez-Zermeno, Zhiyong Hong, Weijia Yuan, Timothy J Flack, and Timothy A Coombs. An improved FEM model for computing transport AC loss in coils made of RABiTS YBCO coated conductors for electric machines. *Superconductor Science and Technology*, 24(4):045005, 2011.
- [145] Min Zhang, Jae-Ho Kim, Sastry Pamidi, Michal Chudy, Weijia Yuan, and TA Coombs. Study of second generation, high-temperature superconducting coils: Determination of critical current. *Journal of Applied Physics*, 111(8):083902, 2012.
- [146] Jianzhao Geng and Timothy Arthur Coombs. Modeling methodology for a HTS

- flux pump using a 2D H-formulation. *Superconductor Science and Technology*, 31(12):125015, 2018.
- [147] Ronald Kreutz, Joachim Bock, Frank Breuer, K-P Juengst, Martin Kleimaier, H-U Klein, Detlef Krischel, Mathias Noe, Ralph Steingass, and K-H Weck. System technology and test of CURL 10, a 10 kV, 10 MVA resistive high-T_c superconducting fault current limiter. *IEEE transactions on applied superconductivity*, 15(2):1961–1964, 2005.
- [148] Chanjoo Lee, Kwanwoo Nam, Hyoungku Kang, Min Cheol Ahn, Tae Kuk Ko, and Bok-Yeol Seok. Design of a high temperature superconducting coil for a 8.3 MVA fault current limiter. *IEEE transactions on applied superconductivity*, 17(2):1907–1910, 2007.
- [149] James HP Rice, Jianzhao Geng, Chris W Bumby, Hubertus W Weijers, Steven Wray, Heng Zhang, Frank Schoofs, and Rodney A Badcock. Design of a 60 kA flux pump for fusion toroidal field coils. *IEEE Transactions on Applied Superconductivity*, 32(4):1–5, 2021.
- [150] Florent Blondelle, Ahmad Sultan, Eddy Collin, and Henri Godfrin. Electrical conductance of bolted copper joints for cryogenic applications. *Journal of Low Temperature Physics*, 175:877–887, 2014.
- [151] TD Le, JH Kim, SI Park, and HM Kim. Conceptual design of current lead for large scale high temperature superconducting rotating machine. *Progress in Superconductivity and Cryogenics*, 16(2):54–58, 2014.
- [152] Chao Li, Shengjie Wang, Hanru Jia, Jiawei He, Bin Li, and Tim A Coombs. Impacts of the saturated transformer on the HTS flux pump. *IEEE Transactions on Applied Superconductivity*, 31(8):1–4, 2021.
- [153] Jianhua Liu, Junsheng Cheng, and Qiuliang Wang. Evaluation of NbTi superconducting

- joints for 400 MHz NMR magnet. *IEEE transactions on applied superconductivity*, 23(6):34–39, 2013.
- [154] K Ohki, T Nagaishi, T Kato, D Yokoe, T Hirayama, Y Ikuhara, T Ueno, K Yamagishi, T Takao, R Piao, et al. Fabrication, microstructure and persistent current measurement of an intermediate grown superconducting (iGS) joint between REBCO-coated conductors. *Superconductor Science and Technology*, 30(11):115017, 2017.
- [155] Y Yanagisawa, R Piao, Y Suetomi, T Yamazaki, K Yamagishi, T Ueno, T Takao, K Ohki, T Yamaguchi, T Nagaishi, et al. Development of a persistent-mode NMR magnet with superconducting joints between high-temperature superconductors. *Superconductor Science and Technology*, 34(11):115006, 2021.
- [156] Seyeon Lee, Woo-Seok Kim, Yungil Kim, Sang Ho Park, Ji-Kwang Lee, Jin-Ho Hahn, Gye-Won Hong, Il Han Park, Chan Park, and Kyeongdal Choi. Characteristics of an HTS pancake coil in persistent current mode using wind-and-flip winding method. *IEEE transactions on applied superconductivity*, 23(3):4601305–4601305, 2013.
- [157] Muhammad Zulfiqar Ali, Jinxing Zheng, Felix Huber, Zhiwei Zhang, Weijia Yuan, and Min Zhang. 4.6 T generated by a high-temperature superconducting ring magnet. *Superconductor Science and Technology*, 33(4):04LT01, 2020.
- [158] Bimal K Bose. Technology trends in microcomputer control of electrical machines. *IEEE Transactions on industrial Electronics*, 35(1):160–177, 1988.
- [159] Daniel A Steck, Kurt Jacobs, Hideo Mabuchi, Tanmoy Bhattacharya, and Salman Habib. Quantum feedback control of atomic motion in an optical cavity. *Physical review letters*, 92(22):223004, 2004.
- [160] R Vijay, Chris Macklin, DH Slichter, SJ Weber, KW Murch, Ravi Naik, Alexander N Korotkov, and Irfan Siddiqi. Stabilizing Rabi oscillations in a superconducting qubit using quantum feedback. *Nature*, 490(7418):77–80, 2012.

- [161] Liyuan Liu, Yunpeng Zhu, Xinsheng Yang, Tian Qiu, and Yong Zhao. Delamination properties of YBCO tapes under shear stress along the width direction. *IEEE Transactions on Applied Superconductivity*, 26(6):1–6, 2016.
- [162] P Chaudhari, RH Koch, RB Laibowitz, TR McGuire, and RJ Gambino. Critical-current measurements in epitaxial films of $\text{YBa}_2\text{Cu}_3\text{O}_{7-x}$ compound. *Physical review letters*, 58(25):2684, 1987.
- [163] Ravi Kumar, SK Malik, SP Pai, PR Apte, R Pinto, R Vijayaraghavan, and Dhanajay Kumar. Self-field-induced flux creep in $\text{YBa}_2\text{Cu}_3\text{O}_{7-y}$ thin films. *Physical Review B*, 46(9):5766, 1992.
- [164] Nicolo' Riva, S Richard, F Sirois, C Lacroix, B Dutoit, and F Grilli. Overcritical current resistivity of YBCO-coated conductors through combination of PCM and finite-element analysis. *IEEE Transactions on Applied Superconductivity*, 29(5):1–5, 2019.
- [165] HTS Modeling Work Group. Modeling of high temperature superconductors (HTS), “www.htsmodelling.com”: date accessed 2022/05/29.
- [166] Shengnan Zou, Víctor MR Zermeño, A Baskys, A Patel, Francesco Grilli, and BA Glowacki. Simulation and experiments of stacks of high temperature superconducting coated conductors magnetized by pulsed field magnetization with multi-pulse technique. *Superconductor Science and Technology*, 30(1):014010, 2016.
- [167] AETECHRON Inc. Aetechron, “www.aetechron.com/IND-RESEARCH-7796.shtml”: date accessed 2023/05/29.
- [168] DS Dezhin and IN Dezhina. Development of the future aircraft propulsion system based on HTS electrical equipment with liquid hydrogen cooling. *IEEE Transactions on Applied Superconductivity*, 32(4):1–5, 2022.
- [169] UNEP. Report on atmosphere and air pollution, 2006.

- [170] Yuan Gao, Charles Jausseme, Zhen Huang, and Tao Yang. Hydrogen-powered aircraft: Hydrogen–electric hybrid propulsion for aviation. *IEEE Electrification Magazine*, 10(2):17–26, 2022.
- [171] Philippe J Masson and Cesar A Luongo. HTS machines for applications in all-electric aircraft. In *2007 IEEE power engineering society general meeting*, pages 1–6. IEEE, 2007.
- [172] Kiruba S Haran, Swarn Kalsi, Tabea Arndt, Haran Karmaker, Rod Badcock, Bob Buckley, Timothy Haugan, Mitsuru Izumi, David Loder, James W Bray, et al. High power density superconducting rotating machines—development status and technology roadmap. *Superconductor Science and Technology*, 30(12):123002, 2017.
- [173] T Balachandran, D Lee, N Salk, and KS Haran. A fully superconducting air-core machine for aircraft propulsion. In *IOP Conference Series: Materials Science and Engineering*, volume 756, page 012030. IOP Publishing, 2020.
- [174] Fangjing Weng, Min Zhang, Tian Lan, Yawei Wang, and Weijia Yuan. Fully superconducting machine for electric aircraft propulsion: Study of AC loss for HTS stator. *Superconductor Science and Technology*, 33(10):104002, 2020.
- [175] M Feddersen, KS Haran, and F Berg. Ac loss analysis of MgB₂-based fully superconducting machines. In *IOP Conference Series: Materials science and engineering*, volume 279, page 012026. IOP Publishing, 2017.
- [176] AM Campbell. Superconducting and conventional machines. *Superconductor Science and Technology*, 27(12):124012, 2014.
- [177] Mohammad Yazdani-Asrami, Min Zhang, and Weijia Yuan. Challenges for developing high temperature superconducting ring magnets for rotating electric machine applications in future electric aircrafts. *Journal of Magnetism and Magnetic Materials*, 522:167543, 2021.

- [178] Yutaka Terao, Yusuke Ishida, Hiroyuki Ohsaki, and Hitoshi Oyori. Electromagnetic characteristic comparison of superconducting synchronous motor characteristics for electric aircraft propulsion systems. *SAE International Journal of Advances and Current Practices in Mobility*, 2(2019-01-1912):828–837, 2019.
- [179] Difan Zhou, Mitsuru Izumi, Motohiro Miki, Brice Felder, Tetsuya Ida, and Masahiro Kitano. An overview of rotating machine systems with high-temperature bulk superconductors. *Superconductor Science and Technology*, 25(10):103001, 2012.
- [180] ICE Oxford Inc. Ice oxford, “www.iceoxford.com”: date accessed 2023/04/02.
- [181] Ravi Kandasamy, Xiang-Qi Wang, and Arun S Mujumdar. Transient cooling of electronics using phase change material (PCM)-based heat sinks. *Applied thermal engineering*, 28(8-9):1047–1057, 2008.
- [182] T Matsuda, T Okamura, M Hamada, S Matsumoto, T Ueno, R Piao, Y Yanagisawa, and H Maeda. Degradation of the performance of an epoxy-impregnated REBCO solenoid due to electromagnetic forces. *Cryogenics*, 90:47–51, 2018.
- [183] Arash Badakhsh, Chan Woo Park, and Byung-Joo Kim. Preparation and analysis of paraffin-based phase change material using aluminum nitride as the reinforcing agent. In *4th International Conference on Nanotechnology, Nanomaterials & Thin Films for Energy Applications*, pages 70–72. One Central Press, University of Aalto, Finland, 2017.
- [184] SM Shalaby, HF Abosheish, ST Assar, and AE Kabeel. Improvement of thermal properties of paraffin wax as latent heat storage material with direct solar desalination systems by using aluminum oxide nanoparticles. *no. June*, pages 28–30, 2018.
- [185] Prabhu Bose and Valan Arasu Amirtham. A review on thermal conductivity enhancement of paraffinwax as latent heat energy storage material. *Renewable and Sustainable Energy Reviews*, 65:81–100, 2016.

- [186] Sastry Pamidi, Chul Han Kim, Jae-Ho Kim, Danny Crook, and Steinar Dale. Cryogenic helium gas circulation system for advanced characterization of superconducting cables and other devices. *Cryogenics*, 52(4-6):315–320, 2012.
- [187] Mark D Bird, IR Dixon, and Jack Toth. Large, high-field magnet projects at the NHMFL. *IEEE Transactions on Applied Superconductivity*, 25(3):1–6, 2014.
- [188] Hyung-Seop Shin, Chan-Hun Jung, and Arman Ray Nisay. Joint characteristics of ultrasonic welded cc bridge joints for hts coil applications. *Superconductor Science and Technology*, 33(11):115007, 2020.
- [189] Phillip V Shoaff, Yusuf S Hascicek, Justin Schwartz, and Steven W Van Sciver. An investigation of the characterizations and development of hts joints in bscco 2212/ag composites. *IEEE transactions on applied superconductivity*, 7(2):1695–1698, 1997.